

Photochemical Studies of Atmospherically Relevant Species in Multiple Phases

Hanna Lignell

University of Helsinki
Faculty of Science
Department of Chemistry
Laboratory of Physical Chemistry
P.O. Box 55 (*A.I. Virtasen aukio 1*)
FIN-00014 University of Helsinki
Finland

University of California Irvine
School of Physical Sciences
AirUCI-institute
Department of Chemistry
1102 Natural Sciences II
Irvine, CA 92697
USA

ACADEMIC DISSERTATION

To be presented, with the permission of the Faculty of Science of the University of Helsinki, for public criticism in the Main lecture hall A110 of the Department of Chemistry (*A. I. Virtasen aukio 1*) on January 24th 2014, at 12 noon.

Helsinki 2014

Supervisors

Professor Markku Räsänen, Laboratory of Physical Chemistry,
University of Helsinki, Finland

Professor Sergey Nizkorodov, Department of Chemistry, University of
California, Irvine, USA

Professor Benny Gerber, Department of Chemistry, University of
California, Irvine, USA

Dr. Leonid Khriachtchev, Laboratory of Physical Chemistry, University
of Helsinki, Finland

Reviewers

Professor Mika Pettersson, Nanoscience Center, University of Jyväskylä,
Finland

Professor Helge Lemmetyinen, Department of Chemistry and
Bioengineering, Tampere University of Technology, Finland

Opponent

Professor Anne Monod, *Laboratoire de Chimie de l'Environnement, Aix-
Marseille Université*, Marseille, France

ISBN 978-952-10-9295-4 (paperback)

ISBN 978-952-10-9296-1 (PDF)

<http://ethesis.helsinki.fi>

Yliopistopaino

Helsinki 2014

Abstract

In this thesis, fundamentally and atmospherically relevant species, their heterogeneous chemistry, and photolytic processing in multiple phases are explored both experimentally and computationally, providing important new insights and mechanistic understanding of these complicated systems.

HArF is a covalently bonded neutral ground-state molecule of argon that is found to form at very low temperatures. This thesis explores the HArF low temperature formation mechanism and kinetics, and discusses the effect of the environment to the formation. In the second part, a computational study of an atmospherically relevant molecule N_2O_4 and its isomerization and ionization on model ice and silica surfaces is presented. N_2O_4 is known to produce HONO, which is a major source of atmospheric OH, an important atmospheric oxidant. The isomerization mechanism is found to be connected to the dangling surface hydrogen atoms at both surfaces, and we suggest that this mechanism could be expanded to other atmospherically relevant surfaces as well.

Atmospheric aerosols play a critical role in controlling climate, driving chemical reactions in the atmosphere, acting as surfaces catalyzing heterogeneous reactions, and contributing to air pollution problems and indoor air quality issues. Low-volatility organic compounds that are produced in the oxidation of biogenic and anthropogenic Volatile Organic Compounds (VOC's) are known collectively as Secondary Organic Aerosol (SOA). In this thesis, a comprehensive investigation of aqueous photochemistry of *cis*-pinonic acid, a common product of ozonolysis of α -pinene (an SOA precursor) is presented. Various experimental techniques are used to study the kinetics, photolysis rates, quantum yields, and photolysis products, and computational methods are used to explore the photolysis mechanisms. Atmospheric implications and importance of aqueous photolysis vs. OH-mediated aging is discussed. The viscosity effects on SOA chemistry are then explored by a novel approach where an environmentally relevant probe molecule 2,4-dinitrophenol is embedded directly inside the SOA matrix, and its photochemistry is studied at different temperatures and compared to reaction efficiency in other reaction media (octanol and water). It is observed that decreasing temperature significantly slows down the photochemical process in the SOA matrix, and this behavior is ascribed to increasing viscosity of the SOA material.

Acknowledgements

First I would like to thank my supervisor in Helsinki, Professor Markku Räsänen. He has been incredibly supportive and believed in me through all these years, and I am proud to have been a part of his research group. Next, I want to express my overflowing gratitude to my current PI and advisor at UC Irvine, Professor Sergey Nizkorodov. His wonderful sense of humor, encouragement, critique, friendship, solid support, and tireless devotion to my research training are greatly appreciated. I warmly thank my third supervisor, Professor Benny Gerber, the man of ultimate wisdom, incredible stories, and genius mind intermingled. His guidance and patience taught me a great deal about science and life, and gave me many lessons in the field of computational chemistry. I also want to acknowledge Dr. Leonid Khriachtchev, who introduced me into the world of noble gas chemistry and demonstrated me what a brilliant researcher and a vivid imagination can create.

I warmly thank Professor Lauri Halonen, the head of the Laboratory of Physical Chemistry in Helsinki, and Professor Barbara Finlayson-Pitts, the director of the AirUCI-institute at UC Irvine. I also want to thank all the past and present group members in Helsinki and Irvine for creating a wonderful atmosphere for making great science. Especially I want to thank the co-authors of my papers; Mychel, Scott, Maggie, Dorit, and Mallory. To Mallory I am forever grateful for her devotion to our project and adapting to a somewhat crazy schedule for my sake.

I want to acknowledge Dr. John Greaves for guiding me through the thick jungle of mass spectra interpretation. Chad Cantwell is thanked for his help with all kinds of computer related problems. Dr. Patricia Terrell is kindly acknowledged for checking the language of this thesis. I also want to express my gratitude to my thesis reviewers, Professors Helge Lemmetyinen and Mika Pettersson.

The Academy of Finland (CoE project Computational Molecular Science), Finnish Ministry of Education (Laskemo Graduate School), Finnish Cultural Foundation, Magnus Ehrnrooth Foundation, and National Science Foundation (NSF) are acknowledged for funding my research.

Next, I want to thank my friends Santtu, Aki, Maija, Litti, Essi, Mikko, Saara, Joonas, Tim, Joy, Diane, Pepe, Ian, Orietta, Tusse, Maria, Juha, Katri, Anttu, Petra, Reijo, and many others for their support in good and bad times. I am grateful to my dear Yogini Lila Russo for helping me grow stronger both

physically and mentally through yoga practice. I would also like to thank my parents-in-law, Lilli and Simo, for always being kind to me.

I thank my big brother Ville, who has been my idol since I was a little girl. He has always helped me, argued with me, tirelessly taught me algebra, and loved me, unconditionally. He supported me until I was ready to stand on my own. I would not have achieved what I have without him. I dearly thank my gentle and loving parents, Raili and Mario. They have loved me, understood me, and accepted and supported me in all the choices I have made in my path. With them in my life I know there is always someone there, no matter what happens.

I proudly thank the brightest light and joy of my life, my children Ilka, Meri-Xenia, Dominic, and Tristan-Star. They have loved me and supported me and with their cute smiles carried me through the long days in the lab. Finally, I want to thank my husband (and colleague) Antti for his love, support, and companionship. Needless to say, this would not have happened without him by my side.

A handwritten signature in cursive script, reading "Hanna Lignell". The signature is written in a light, elegant style with a small flourish at the end of the name.

Hanna Lignell
Santa Monica, California
September 2013

Contents

List of Original Publications	8
Abbreviations	10
1. Introduction	11
1.1 HARF Molecule	12
1.2 Oxides of Nitrogen	14
1.3 Secondary Organic Aerosol	16
1.4 Temperature Dependence of Photochemistry of SOA Matrices	19
2. Experimental Methods	22
2.1 HARF Preparation and Photolysis	22
2.2 Aqueous Photolysis of <i>cis</i> -Pinonic Acid	23
2.3 Gas Phase Photolysis of <i>cis</i> -Pinonic Acid	27
2.4 Comparison of <i>cis</i> -Pinonic Acid Loss Mechanisms	28
2.5 Photochemistry of SOA Matrices and Aqueous Solutions	30
3. Computational Methods	34
3.1 Isomerization and Ionization of N ₂ O ₄ on Model Ice and Silica Surfaces	34
3.2 The Photoexcitation Dynamics of PA and Hydrated PAMe	36
4. Results and Discussion	37
4.1 Low Temperature Formation of HARF	37
4.1.1 Precursors and Preparation	37
4.1.2 Low Temperature Formation	39
4.1.3 Decay of (ArHAr) ⁺ and (ArDAr) ⁺ and Implications of Tunneling Reaction	40
4.1.4 Locality of the Photolysis	43
4.1.5 HARF@Ar _n Supermolecule	45
4.2 Heterogeneous Chemistry of N ₂ O ₄ on Model Ice and Silica Surfaces	47
4.2.1 Isomerization	48
4.2.2 Ionization	51
4.2.3 Atmospheric Implications	52
4.3 Aqueous Photochemistry of <i>cis</i> -Pinonic Acid and α-pinene SOA	53
4.3.1 Products and Mechanism of the Aqueous PA Photolysis	56
4.3.2 Absorption Cross Sections and Quantum Yield of the Photolysis	64
4.3.3 The Gas Phase Photolysis of PAMe	69
4.3.4 Computational Results for the PA Photochemistry	71
4.3.5 Atmospheric Implications	74
4.3.6 Temperature Dependence of the Aqueous Photochemistry of α-pinene SOA	77
4.4 Temperature Dependence of the Photolysis of SOA Matrices	79
4.4.1 Photolysis of the SOA Materials	79
4.4.2 Photolysis of the α-pinene SOA Matrix with 24-DNP as a Probe	82
4.4.3 Temperature Dependence of the Photochemistry of 24-DNP in Octanol	87
4.4.4 Conclusions and Atmospheric Implications	92
5. Concluding Remarks	96
References	97

List of Original Publications

This thesis is based on the following publications:

- I Hanna Lignell, Leonid Khriachtchev, Antti Lignell, and Markku Räsänen, *Local formation of HARF in solid argon: Low temperature limit and thermal activation*, *Low Temp. Phys.* 36, 400 (2010)
- II Hanna Lignell, Mychel E. Varner, Barbara J. Finlayson-Pitts, and R. Benny Gerber, *Isomerization and ionization of N₂O₄ on model ice and silica surfaces*, *Chem. Phys.* 405, 52 (2012)
- III Hanna Lignell, Scott Epstein, Margaret Marvin, Dorit Shemesh, R. Benny Gerber, and Sergey A. Nizkorodov, *Experimental and theoretical study of aqueous cis-pinonic acid photolysis*, *J. Phys. Chem. A*, 117, 12930 (2013)
- IV Hanna Lignell, Mallory L. Hinks, and Sergey A. Nizkorodov, *Viscosity suppresses photochemistry in organic aerosols*, *Proc. Natl. Acad. Sci.*, Submitted (2013)

All previously published material is reprinted with permission from the original publishers.

Contributions:

Article I: The author performed major part of the experiments and data analysis and was responsible for writing the first draft of the paper.

Article II: The author performed all the calculations and data analysis and wrote the paper.

Article III: The author performed major part of all the experiments and was responsible of most of the data analysis of the experimental data. The author wrote the paper.

Article IV: The author performed major part of the experiments and data analysis, and wrote the paper.

Other publications related to this thesis:

1. Antti Lignell, Leonid Khriachtchev, Hanna Mustalampi, Toni Nurminen, and Markku Räsänen, *Interaction of bihalogen anions with nitrogen: Matrix-isolation study and first principle calculations of the (ClHCl)⁻ ···N₂ and (BrHBr) ···N₂ complexes*, Chem. Phys. Lett. 405, 448 (2005)
2. Antti Lignell, Leonid Khriachtchev, Hanna Lignell, and Markku Räsänen, *Protons solvated in noble-gas matrices: Interaction with nitrogen*, Phys. Chem. Chem. Phys. 8, 2457 (2006)
3. Anastasia Bochenkova, Leonid Khriachtchev, Antti Lignell, Markku Räsänen, Hanna Lignell, Alexander Granovsky, and Alexander Nemukhin, *Hindered rotation of HARF in solid argon*, Phys. Rev. B 77, 094301 (2008)
4. Emily E. Hardegree-Ullman, Murthy S. Gudipati, Adwin C. A. Boogert, Hanna Lignell, Louis J. Allamandola, Karl R. Stapelfeldt, Michael Werner, *Laboratory determination of the infrared band strengths of pyrene frozen in water ice: Implications for the composition of interstellar ices*, Astrophys J., Submitted (2014)

Abbreviations

24-DNP	2,4-Dinitrophenol
ADC(2)	Algebraic Diagrammatic Construction method 2
BVOC	Biogenic Volatile Organic Compound(s)
CIMS	Chemical Ionization Mass Spectrometry
CMK	Cyclobutyl Methyl Ketone
Da	Dalton
DFT	Density Functional Theory
ESI-MS	ElectroSpray Ionization Mass Spectrometry
FTIR	Fourier Transform InfraRed
FWHM	Full Width at Half-Maximum
GC	Gas Chromatography
H-transfer	Hydrogen transfer
HPLC	High Performance Liquid Chromatography
IR	Infrared
IRC	Intrinsic Reaction Coordinate
ISC	InterSystem Crossing
IVOC	Intermediate Volatile Organic Compound(s)
LC	Liquid Chromatography
LWC	Liquid Water Content
MAC	Mass Absorption Coefficient
MI	Matrix Isolation
MNDO	Modified Neglect of Diatomic Overlap
MP2	Møller-Plesset 2 nd order perturbation theory
MRCI	MultiReference Configuration Interaction
NPA	Natural Population Analysis
NMR	Nuclear Magnetic Resonance
NOx	Nitrogen Oxides
OM2	Orthogonalization corrected semiempirical Method2
PA	<i>cis</i> -Pinonic Acid
PAMe	<i>cis</i> -Pinonic Acid Methyl ester
PM	Particulate Matter
PM3	Parametric Method 3
PTR-MS	Proton Transfer Reaction Mass Spectrometer
RI	Resolution-of-the-Identity
S/N	Signal-to-Noise
SIMPOL	Simplified P ^o _L prediction method
SLM	Standard Liters per Minute
SOA	Secondary Organic Aerosol
SOM	Secondary Organic Material
SZA	Solar Zenith Angle
TMS	TetraMethylSilane
ToF	Time-of-Flight
TS	Transition State
UV	UltraViolet
UV-Vis	UltraViolet-Visible
VOC	Volatile Organic Compound(s)
VUV	Vacuum UltraViolet
WSOC	Water Soluble Organic Compound(s)
ZPE	Zero-Point Energy

1. Introduction

The air quality of the lower atmosphere has dramatically improved in developed countries as a result of different air pollution control strategies and environmental laws since the 1960's, but especially in densely populated urban areas and in the developing countries, the air quality issues continue to have great impact on public health and visibility degradation. In the Los Angeles area, the concentrations of particulate matter (PM) have decreased from ~ 60 to $20 \mu\text{g}/\text{m}^3$ (PM₁₀) and from ~ 90 to $60 \mu\text{g}/\text{m}^3$ (PM_{2.5}) during the past 30 years,¹ whereas the situation is much worse in some other large cities, for example Beijing and Teheran, where air pollution is currently at extreme levels. The air quality index values of these cities are constantly reported as very unhealthy. Research in the field of atmospheric sciences is crucial, clearly evidenced by a recent study which revealed that 2.1 million deaths occur each year as a result of human-caused air pollution.²

Fundamental and applied research in the field of atmospheric sciences has greatly enhanced our understanding of different processes in the gas phase. Detailed gas phase kinetics databases are available with information about absorption cross sections, photolysis quantum yields, reaction rate constants, etc. (for example the JPL's Chemical Kinetics and Photochemical Data for Use in Atmospheric Studies).³ Such data concerning condensed phase processes, however, are largely lacking. Under Earth's tropospheric conditions, the knowledge concerning heterogeneous reactions remains limited because of complexity and great number of relevant reactive species and a wide range of surfaces available for these reactions. Water films, ice, organic surfaces, urban silica surfaces (such as buildings, soil) all catalyze different heterogeneous reactions. In addition, variations in different environmental parameters (such as water vapor concentration, solar intensity, and meteorological conditions) make the understanding of heterogeneous chemistry a challenging task.^{4,5} Current models severely underpredict the amounts of particulate air pollutants, while gas-phase predictions of O₃ and NO_x compounds are modelled reasonably well. State-of-the-art experiments and theoretical methods are urgently needed to advance our understanding of particulate air pollutants to the same level as for gas-phase pollutants.

The outcome of chemical and photochemical reactions taking place at surfaces or at condensed phase can in some cases be dramatically different from corresponding gas phase reactions. Molecules trapped inside condensed phase matrix are affected not only by physical restrictions from

their neighboring molecules, but they can also react with the host molecules, sometimes producing unexpected and exotic results. The effects of the host matrix on photochemical reactions have been demonstrated in various fields of chemistry, from fundamental condensed phase research in noble gas matrices⁶ to atmospherically relevant aerosol photochemistry.⁴ For example, most organic reactions, including atmospherically relevant ones, occur by completely different reaction pathways in water and in organic solvents, and are strongly affected by the presence of trace levels of oxygen in the solution.⁷ In this thesis, fundamentally and atmospherically relevant species, their heterogeneous chemistry, and photolytic processing in condensed phases are explored both experimentally and computationally, providing important new insights and mechanistic understanding of these complicated systems. In the following sections, the specific systems targeted by this thesis will be introduced in greater detail.

1.1 HArF Molecule

Noble-gas hydride molecules with general formula HNgY [H = Hydrogen atom, Ng = Noble-gas atom (Ar, Kr or Xe), and Y = electronegative fragment] were discovered in 1995 and they have been since studied both experimentally and computationally.⁸⁻¹² These molecules are prepared using photolysis of HY precursor in a noble-gas matrix, followed by thermally induced hydrogen diffusion reaction in noble-gas matrices.^{13,14} They can also be formed directly after irradiation as an intermediate reaction, indicating locality of solid-state photolysis.¹⁵⁻¹⁷ The formation of HNgY molecules takes place via $H + Ng + Y$ reaction of neutral fragments and they have a charge-transfer nature showing a strong $(HNg)^+Y^-$ character. HArF molecule is a covalently bonded neutral ground-state molecule of argon.^{16,18} It is synthesized experimentally using the VUV photolysis of HF in solid argon at 7-8 K. It was observed that HArF can occupy two different matrix site configurations referred to as unstable HArF and stable HArF.^{18,19} The unstable HArF configuration is formed in large quantities upon annealing at higher temperatures (up to 28 K). Upon annealing above 28 K, unstable HArF decomposes leaving only the stable form visible. This thermal modification of the HArF absorption bands is a remarkable solid-state phenomenon. The conversion is strongly related to the surrounding matrix environment and this behavior suggests that in condensed phase the concept of a single molecule needs to be refined. The appearance of HArF molecule in two distinctively separate matrix sites suggests that it could be more appropriate to consider HArF as a so called “supermolecule”, denoted as HArF@Ar_n.

Many computational and theoretical studies concerning the properties of HArF molecule have been carried out. For example, the structure, potential energy surface, and vibrational properties (both harmonic and anharmonic) have been examined.²⁰⁻²⁴ The trapping configurations of HArF in the argon matrix have been simulated in numerous studies,²⁵⁻²⁷ and Bochenkova *et al.* reported theoretical and experimental results on libration motion of HArF in solid argon²⁸ and on thermal reorganization of the unstable to stable HArF configuration.²⁹ Both the supermolecule concept and libration motion are important solid-state processes, making the only known argon containing molecule an extremely interesting species.

In Article I, it was demonstrated that HArF was slowly formed after photolysis of the HF/Ar matrices down to 8 K. It is probable that this low temperature formation of HArF molecule is a short-range process and involves quantum tunnelling of hydrogen. The local, short-range processes have been discussed while dealing with noble-gas compounds. Pettersson *et al.* have shown that the formation of HXeI molecule is a combination of local and global H atom mobilities³⁰ and the recovery of HXeCC and HXeI after IR decomposition are local processes.^{13,14} The local formation mechanism of the HArF seems to be different from the other HNgY molecules in Kr and Xe matrices, in which they form mainly upon global mobility of hydrogen atoms that are activated by thermal annealing.³¹ In this thesis, the formation kinetics of HArF in low temperatures (down to 8 K) is considered in detail. Concentration dependence, effect of broadband IR-radiation, H/D isotope effect, activation energy, and mechanism for the formation are discussed underlining the importance of understanding the fundamental condensed phase photochemical processes.

A related reaction taking place at low temperature noble-gas matrices is the decay of (NgHNg)⁺ cations that are formed upon photolysis. This phenomenon has been discussed extensively in the literature, and different mechanisms have been proposed.³¹⁻³⁴ Previously it has been suggested that the formation of HArF and decay of (ArHAr)⁺ are fundamentally unconnected.³² In this thesis, the connection between these species is briefly revisited; the results presented here are found to support the previous conclusions.

Although the noble gases and their chemistry might seem esoteric at first glance, detailed knowledge concerning their photophysics is very informative for understanding the behavior of highly reactive molecules constrained in a rigid environment. Also, the experimentally realized HXeOXeH molecule can

be considered as a combination of water and two Xe-atoms, both of which occur in the atmosphere.³⁵ This molecule may represent a first step towards the possible preparation of (Xe-O)_n chains, and it can be potentially relevant to the geochemical “missing xenon” problem.^{36,37}

1.2 Oxides of Nitrogen

Reactive nitrogen oxides (NO_x = NO + NO₂) act as catalysts of oxidation of hydrocarbons in the atmosphere and are closely tied to lower atmosphere ozone chemistry. NO_x have both natural and anthropogenic sources, including fossil fuel combustion, biomass burning, and oxidation of atmospheric ammonia.³⁸ The heterogeneous reaction of NO₂ with water in thin, liquid water films produces HONO and HNO₃,⁴ and these molecules have important role in the chemistry of troposphere. HONO molecule is a major source of atmospheric OH, which is a very important atmospheric oxidant.³⁹ Since OH initiates the chemistry that leads to the formation of ozone and other air pollutants, it is important to determine which OH precursors are significant in order to accurately model urban airsheds and to develop regional control strategies. Previously it has been suggested that the formation of a complex between NO₂ and water at the air–water interface is the key step in the mechanism.⁴ In the atmosphere, the primary formation reaction of HONO is assumed to be the following:



Possible other formation processes and reactions of HONO in the Earth’s atmosphere have been reviewed,⁴⁰ but the mechanism of the formation reaction is not completely understood. Particularly at higher concentrations and lower temperatures, presence of the N₂O₄ dimer is in equilibrium with NO₂ and the dimer can contribute the equilibrium reaction significantly:



It has been proposed that during the heterogeneous hydrolysis process, the more stable, symmetric isomer of N₂O₄ is converted at the water surface to its asymmetric isomer ONONO₂, which then cleaves into ions.⁴¹⁻⁵⁰ HONO is created when the ion pair reacts with water and surface-adsorbed HNO₃ is produced simultaneously. The asymmetric isomer ONONO₂ is the more reactive form of the dimer, and the isomerization reaction has been studied previously using both experimental and computational methods.

Experimental study by Koel and Wang explored the isomerization on amorphous ice surface. They brought up the possible participation of the dangling surface $-OH$ bonds in the isomerization mechanism.⁴⁸ In a computational study by Jung and Marcus the dangling $-OH$ bonds were also found to have a role in catalyzing reactions via hydrogen bonding at organic-water interfaces.⁵¹ This study was motivated by experimental work by Narayan *et al.* where the role of water in reactivity of organic compounds was investigated.⁵² The dimerization and isomerization of NO_2 in both in absence and in presence of water have been studied by Pimentel and coworkers. Their investigations include calculations of the isomerization barriers with a polarizable continuum model,⁵⁰ direct asymmetric isomerization,⁴⁹ and isomerization in presence of water clusters.⁴² The water cluster model revealed that at least 3 water molecules were required to produce a stable asymmetric dimer product, and if the water molecule number was increased to 7, a direct route for formation of HONO and HNO_3 was also observed. A computational study by Miller *et al.* provided insights into the dynamics of the asymmetric $ONONO_2$ in presence of water clusters.⁵³ They utilized molecular dynamics simulations to investigate the timescales of the $ONONO_2 \rightarrow NO^+NO_3^-$ ionization reaction, and reported that contact with just a single water molecule at room temperature leads to the separation on a timescale of several picoseconds. Increasing the number of water molecules accelerated the ionization.

As the formation of HONO is of critical importance due to its role in the tropospheric OH production, it is of considerable interest to broaden the understanding of the formation from liquid water films to ice and other atmospherically relevant surfaces. In Article II of this thesis, model ice and silica surfaces were chosen for this purpose, as they both represent this group of surfaces. The importance of ice in the atmosphere cannot be underestimated, and silicates on the other hand are major components of building materials, roads, and soils.⁵⁴ While the previous studies utilizing small clusters as water model systems have been useful in understanding the formation of HONO,^{42,50,53} and related reactions,^{55,56} the more realistic approach is certainly more relevant when atmospheric reactions and phenomena are concerned. The model surfaces used in Article II to investigate the isomerization of N_2O_4 were $(H_2O)_{20}$ ice cluster and $Si_8O_{16}H_{12}$ particle, which is a $(SiO_2)_8$ cluster with surface hydrogens resembling the crystal structure of quartz. In this thesis the isomerization mechanism is presented and the further ionization will be briefly considered. Atmospheric implications will be discussed.

1.3 Secondary Organic Aerosol

Atmospheric aerosols play a critical role in controlling climate, driving chemical reactions in the atmosphere, acting as surfaces catalyzing heterogeneous reactions, and contributing to air pollution problems and indoor air quality issues.^{4,5,57,58} Presence of the solar radiation gives rise to complex photochemical reactions that drive the chemistry of the aerosols in both the gas- and the particle-phase. The chemical composition and properties of the tropospheric aerosols is largely controlled by organic compounds. A significant fraction of organic compounds are emitted in the atmosphere directly by various sources (vegetation, fires, traffic, industrial emissions, ocean wave breaking) in the form of Primary Organic Aerosol (POA). Low-volatility organic compounds that are produced in the oxidation of biogenic and anthropogenic Volatile Organic Compounds (VOC's) are known collectively as Secondary Organic Aerosol (SOA). SOA is now believed to make a larger contribution to the mass concentration of tropospheric particulate matter than POA does.⁵⁸⁻⁶¹ SOA is produced in the troposphere as a result of chains of complex reactions that start with the oxidation of the VOC's by ozone (O_3), hydroxyl radical (OH), and nitrate radical (NO_3). These reactions culminate with the condensation of low-volatility oxidation products into pre-existing particles or with the formation of new particles by a select group of oxidation products that have an especially low volatility.

One important group of VOC's that efficiently forms SOA is terpenes, a class of hydrocarbons emitted to the troposphere primarily by vegetation. Terpenes include monoterpenes ($C_{10}H_{16}$), sesquiterpenes ($C_{15}H_{24}$), and oxygenated terpenes.⁶¹⁻⁶³ Atmospheric lifetimes of terpenes vary from minutes to hours due to gas-phase reactions with O_3 , OH, and NO_3 and these reactions produce a variety of organic compounds. Further atmospheric processing of the primary oxidation products can occur in different phases. More volatile compounds will continue to react primarily in the gas-phase. However, water soluble compounds may react faster in the aqueous phase associated with cloud droplets, fog droplets, and aerosol water (some liquid water is always present in aerosol particles). Compounds with a large affinity for organic solvents may preferentially react in the "particle phase", which is dominated by the low-volatility SOA organics. Figure 1 schematically describes some of the key processes including the partitioning of organics between different phases and photooxidation in different phases leading to highly "aged" aerosol, which is eventually removed by wet and dry deposition.

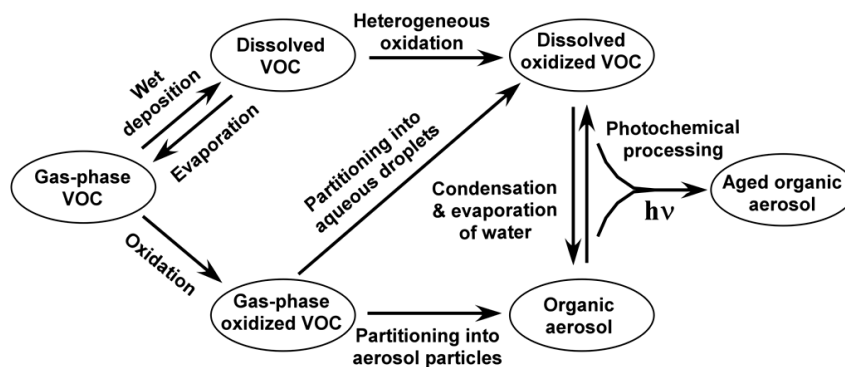


Figure 1. Simplified diagram of atmospheric processing of terpenes and their oxidation

The chemical composition of SOA is highly complex. The determination of composition and oxidation of laboratory generated SOA from various SOA precursors requires highly-sophisticated analytical techniques capable of handling complex mixtures,^{64,65} and many of the components still remain unidentified. An additional challenge in molecular characterization of SOA is its highly dynamic nature. Once SOA is formed, it can go through various photochemical and non-radical driven processes in a dry state, a wetted state, and a dissolved state inside cloud and fog droplets. SOA is removed from the atmosphere after several days through wet and/or dry deposition, and this offers more than sufficient time for these “aging” processes to significantly change the chemical make-up of the particles.

Of the biogenic VOC's, monoterpenes α -pinene and d-limonene are commonly emitted in to the atmosphere therefore playing key roles in the SOA formation.⁶⁶⁻⁸⁵ The global α -pinene emissions estimated at 66 Tg/yr are larger than emissions of any other BVOC with the exception of methanol and isoprene.⁸⁶ The chemical mechanism of the α -pinene oxidation has been widely studied over the years, a representative list of these studies is provided in Ref. 87. Laboratory ozonolysis of α -pinene and d-limonene produces a complex mixture of organics as condensed phase products, for example pinonaldehyde, pinonic acid, nor-pinonic acid, pinic acid, limonic acid, limononic acid, and 7-hydroxylimononic acid.^{71,88} Photooxidation of α -pinene under low relative humidity has recently been studied in both gas and particle phase.^{84,85}

cis-Pinonic acid (hereafter abbreviated as PA) is one of the major products of ozonolysis reaction of α -pinene. It is moderately soluble in water and is an example of a compound classified as IVOC (intermediate volatility organic

compound), thus it can exist in gas-phase, aqueous phase, and in particle phase. Several studies that investigated SOA production from oxidation of terpenes have reported observations of PA,^{67,68,89,90} making PA an important tracer of α -pinene chemistry. The OH-initiated oxidation of PA has also been investigated.⁹¹ In field studies, PA has been reported in fine aerosols found in forested, urban, and rural areas^{92,93} and PA methyl ester (methyl pinonate) has been detected in fog droplets.⁹⁴ It has been suggested that aerosol formation that takes place over forests is dominated by condensable organic vapors (including PA).⁹⁵ PA also efficiently lowers the surface tension of water clusters and thus plays an important role in availability of atmospheric aerosol particles for cloud formation, demonstrated by both experimental and computational results.^{96,97}

The role of water (cloud/fog water, aerosol water, and ice) in the atmosphere cannot be understated. Even though liquid water content even in the densest fogs and clouds is low (typically <0.5 g liquid per cubic meter of air), water droplets and ice crystals provide unique conditions for aqueous phase photochemistry of water soluble organic compounds (WSOC).⁹⁸⁻¹⁰¹ Heterogeneous processes involving trace gases uptaken by various solid interfaces in Earth's surface significantly impact important atmospheric processes and phenomena.¹⁰² It has been estimated that aerosol water mass exceeds dry aerosol mass by a factor of 2-3 under typical troposphere conditions.^{103,104} Terpenes and other SOA precursors can access aqueous aerosol particles via wet deposition and go through oxidation process in the aqueous phase.¹⁰⁵⁻¹⁰⁹ Soluble atmospheric organic compounds end up staying in the cloud and fog droplets for significant periods of time, and this aqueous phase chemistry taking place in these conditions can differ from reactions in dry SOA particles or in the gas phase. Reactions in aqueous environments can lead to unique product formation of species for which no efficient gas phase sources exist.¹¹⁰ Aqueous phase can also offer new uptake mechanisms and change the oxidation state of organics compared to particles in dry conditions.¹¹¹ It is believed that the aqueous SOA chemistry could partly explain the discrepancies between the measurements from gas-phase oxidation mechanisms in the laboratory and SOA measured on the field.¹¹²⁻¹¹⁷ SOA composition can be significantly modified in aqueous phase by direct photolysis.¹¹⁸⁻¹²¹ and relative humidity also affects the behavior and viscosity of the SOA particles.¹²²

As previously mentioned, ozonolysis of α -pinene produces *cis*-pinonic acid (PA) as one of the primary products; further oxidation of PA in both the gas and the aqueous phase then leads to highly-oxidized products that condense to SOA. One of the main objectives of this thesis is to better understand the

mechanisms of the aqueous photolytic processing of the α -pinene SOA (and of monoterpenes in general) in the atmosphere utilizing both experimental and computational methods. In Article III, PA was chosen as a representative α -pinene SOA constituent, and the rate, quantum yield, reaction products, and mechanism of its aqueous photolysis were investigated. PA is not only an atmospherically relevant compound; its intermediate volatility also offers the opportunity to directly compare its photochemistry between gas-phase and condensed-phase environments. PA also includes two different functional groups separated by a rigid butyl ring, thus giving it characteristics that other multifunctional molecules found in the atmosphere possess. The results provide useful insights into the role of carbonyls in photochemical aging of aqueous SOA and raise new questions about the challenge of identifying specific tracer molecules that can be uniquely attributed to a specific VOC or to a specific photochemical process.

1.4 Temperature Dependence of Photochemistry of SOA Matrices

In the troposphere, chemical reactions can take place not only in the gas-phase but also in/on condensed media, and these reactions are much less understood than those taking place in the gas-phase. Aerosol particles can provide unique reaction environments for complex chemistry and such reactions have been discussed in the literature.¹²³ For example, the uptake of N_2O_5 on aerosol particles has been widely studied,¹²⁴ and it has been shown that the heterogeneous chemistry of N_2O_5 on chloride-containing aerosol efficiently releases photolabile chlorine-containing compounds to the atmosphere.^{55,125} By way of another example related to section 1.2, the heterogeneous hydrolysis of N_2O_4 on an air-water interface is known to produce HONO.⁴¹ The complex material associated with the secondary organic aerosol particles (sometimes referred to as “secondary organic material” or “SOA material” or simply “SOM”), which is believed to be the dominant component of atmospheric particles by mass, may provide an especially rich environment for atmospheric photochemistry. The types of compounds found in SOA material have a great variety of functional groups available for both direct photolysis as well as secondary photochemistry. Quantitative determination of the composition, physical properties and chemical properties of SOA material is a challenging task. The compounds forming SOA typically have chemical structures corresponding to highly oxidized C₅-C₁₅ compounds with oxygen-to-carbon ratios approaching 1, the value characteristic of carbohydrates. This would suggest an amorphous

solid structure (also referred to as glassy) for SOA material. The glassy state of SOA particles was observed for the first time in a study where the particles containing products from oxidized biogenic VOC were shown to bounce from substrates upon impaction in a way expected from solids.¹²⁶ Whereas the “phase state” of aerosol particles cannot be defined in a classical sense, or at all, studies concerning the properties of the SOA material (such as viscosity) certainly are relevant. Past studies on atmospherically relevant particle viscosities are very limited, but it has been shown that viscosity can be an important factor when new particle formation and growth rates, gas-particle exchange rates, water diffusion rates,¹²⁷ and reactive uptake are concerned. A recent study by Abramson *et al.* used evaporation rates of molecules trapped inside SOA particles to determine a reasonably accurate value for SOA material viscosity.¹²⁸ Increasing viscosity can limit molecular diffusion inside SOA material, changing the formation rates and mechanisms,¹²⁹⁻¹³¹ and it can also change oxidation rates of species residing inside the organic environment.^{131,132} The viscosity and diffusivity are usually connected to each other through Stokes-Einstein relationship,¹²² but the validity of this relationship has recently been called into question for SOA particles.¹²⁷ Measurements of molecular diffusivity in particles and measurement of viscosity of representative SOA materials just start to emerge, and more studies are needed in order to understand the impact of these parameters on the climate and air quality issues. Humidity appears to have the greatest effect of SOA material viscosity because of the plasticizer properties of water.¹³¹ Viscosity changes associated with the relative humidity dependent hygroscopicity of NaCl and sucrose aerosols, as well as reaction dependent changes in viscosity during ozonolysis of oleic acid aerosols have recently been reported.¹³³

Understanding particle viscosity is especially important for modeling the formation of SOA in air-pollution models. The importance of the phase-state determination is related to the gas-particle partitioning equilibrium. In case of liquids the timescale of diffusive mixing is not rate limiting, but recent studies show that the equilibration timescale for gas-particle partitioning in semisolid SOA particles can be increased to hours or even days.¹³⁴ These conditions are more likely to affect the partitioning in remote forest areas, where the biogenic aerosol particles more likely possess the amorphous solid features,¹²⁶ as well as low mass loadings and large particle sizes.¹³⁴ Also SOA particles in mid- and upper troposphere are affected by the slower equilibration conditions due to reduced temperatures.¹³¹

So far, the viscosity effects have been considered only from the perspective of physical properties of particles, diffusion of molecules through particles, and

gas-particle equilibria as discussed above. The effect of viscosity on photochemistry of compounds trapped in particles has not been explored. In this thesis, the viscosity effects on SOA chemistry were approached by investigating how the temperature affected the reaction rate of the photolysis reaction in a model SOA matrix. The premise of the experiments was that lowering the temperature of an SOA material should increase its viscosity and potentially reduce the yields and branching ratios of photolytic processes occurring in the SOA matrix, via more efficient caging of the primary photolysis products. Such temperature effects were first explored in d-limonene and α -pinene SOA matrix photolysis, both of which acted as viscous liquids or amorphous solids, depending on the temperature. In more systematic study, photolysis of an atmospherically relevant probe molecule, 2,4-dinitrophenol (hereafter referred to as 24-DNP), was investigated in an α -pinene SOA matrix at different temperatures, and for comparison in octanol films (organic liquid) and in an aqueous solution. Studies comparing photochemistry of atmospherically relevant molecules in aqueous, liquid organic, and solid-like organic phases have not previously been published.

In Article IV, 24-DNP was chosen as a probe molecule to investigate the difference of photochemical behavior in aqueous, organic liquid, and organic solid phase. 24-DNP is an atmospherically relevant molecule, which absorbs UV and blue radiation strongly. 24-DNP can be found from both surface waters and atmospheric waters (clouds, fogs, aqueous aerosols), its main sources being air pollution from industrial plants and pesticide runoff waters.¹³⁵ 24-DNP is the strongest phytotoxic nitrophenol which can be detected in the environment in significant amounts.¹³⁶ Previous laboratory studies on the photodegradation and phototransformation of 24-DNP have been published, but they were limited to aqueous phase experiments.¹³⁷ The importance of this molecule in seawaters has also been demonstrated.¹³⁸ The photoproducts of this species are not known, but the similarities to molecules which photochemistry is better understood¹³⁹⁻¹⁴¹ provided insights to the photodissociation process. It has been suggested previously, that the 24-DNP could form from nitration reactions of mononitrophenols in solution. In clouds, anti-correlation has been found between the atmospheric levels of 24-DNP and 2-nitrophenol, while no traces of 24-DNP have been detected under clear weather conditions.¹⁴² 24-DNP has also been found to form in aqueous solutions via reactions with excited mononitrophenols and NO_2 .¹⁴³

As 24-DNP has a low vapor pressure (1.42×10^{-7} mmHg)¹⁴⁴ and high octanol-water partitioning coefficient ($K_{ow} = 8738$),¹⁴⁵ it is plausible to assume that it resides as likely in organic phase as in aqueous phase. In Article IV, the fate

of this molecule was investigated, and as only a small number of previous studies related to organic phase photochemistry of organic particulate matter exist,¹⁴⁶ the results provide new information about the photochemistry of this environmentally relevant species, and general insights into photochemistry occurring in SOA material.

2. Experimental Methods

2.1 HARF Preparation and Photolysis

In the standard Matrix Isolation (MI) technique the sample gas and matrix gas are mixed in a glass bulb with typical mixing ratios of 1:(200-2000) and then deposited onto a cold CsI substrate (7-60 K), respectively. The advantage of the MI technique is that it allows the study of highly reactive species or molecules that are unstable under normal conditions. In this work, the HF/Ar solid matrices were studied in a closed cycle helium cryostat (APD, DE 202A) that provided temperatures down to 8 K. The matrices were deposited onto a cold CsI substrate by passing Ar gas (AGA, 99.9999%) through HF-containing pyridine polymer (Fluka). The deposition temperature varied between 8 and 16 K, but most of the matrices were deposited at 12 K for consistency, since the deposition temperature can affect the HARF formation rate at low temperatures. Impurity water was removed from the sample-gas flow by adding a sulphuric acid H₂SO₄ drop (J. T. Baker, 95-97%) to the deposition line. Deuteration of HF was achieved by using deuterated sulphuric acid D₂SO₄ (Merck, 96-98%, D > 99 %). The deuteration degree of HF was up to 90 %. The ratio of Ar gas and HF was varied by changing the amount of the pyridine polymer and varying the argon gas flow rate. After the sample gas was deposited, the matrices were photolyzed using a krypton lamp (126-160 nm). Although the absolute concentrations of HF and DF were difficult to determine when using the pyridine polymer preparation method, the Ar/HF ratio could be estimated using the integrated molar absorptivity of gas phase HF. Using this approximation, the mixing ratios were typically found to be ~1:2000. Nicolet SX60 spectrometer was used in transmission mode to record the IR absorption spectra in 4000-400 cm⁻¹ range with 1 cm⁻¹ resolution using a liquid-nitrogen-cooled MCT-A detector and Ge-KBr beam splitter. In some of the experiments, the matrices were annealed up to 20 K after photolysis. Schematic view of the experimental setup is presented in Fig. 2.

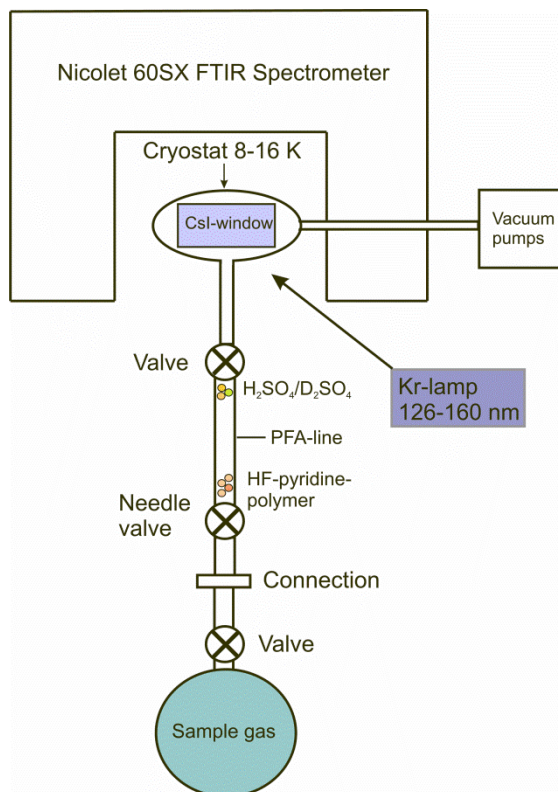


Figure 2. Experimental setup for HArF preparation and photolysis

2.2 Aqueous Photolysis of *cis*-Pinonic Acid

For the aqueous photolysis experiments, PA (Sigma-Aldrich, 98%) was dissolved in HPLC grade water (Fisher Scientific, Omnisolv, HPLC grade) with concentrations varying between 1.0-18 mM. The samples were photolyzed in 30 minute time intervals up to 2 hours in a standard 1 cm⁻¹ quartz cuvette. The cuvette was exposed to open air during photolysis. Radiation from a 150 W Xenon UV-lamp in an air-cooled housing (Newport model 66902) was reflected by a 90-degree dichroic mirror (Edmund optics #NT64-451) and filtered with a U-330 band-pass filter (Edmund optics #46-438, center wavelength 330 nm, FWHM 140 nm). The spectrum of the photolyzing radiation was recorded using a portable UV/VIS spectrometer (Ocean Optics USB4000); most of the radiation was confined at 280-400 nm spectral range. The photolysis reaction was monitored with a Shimadzu UV-2450 dual-beam UV/VIS spectrometer using nanopure water as a reference

(the cuvette was periodically removed from the photolysis setup for this measurement). The experimental setup and the lamp's spectrum are shown in Fig 3.

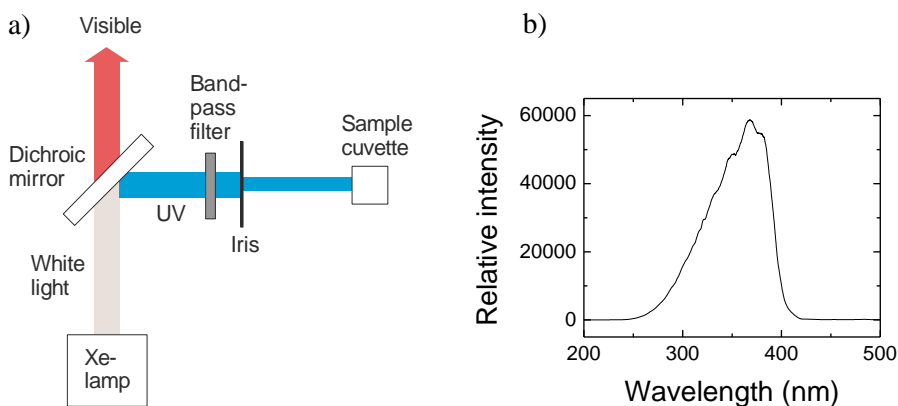


Figure 3. a) Schematic layout of the experimental setup for aqueous phase photolysis (top view). The dichroic mirror serves to isolate the 280-400 nm band, and the bandpass filter further limits the transmission of the visible and near-IR radiation. b) The spectrum of the radiation used in the aqueous photolysis experiments recorded with an Ocean Optics USB4000 spectrometer.

UV-Vis spectra of PA with varying concentrations were recorded to confirm that Beer's law was obeyed ($\epsilon = 76.87 \text{ L mol}^{-1} \text{ cm}^{-1}$ at the peak of the $\pi^* \leftarrow n$ transition at 280 nm), see Fig. 4. The quantum yield of the photolysis of PA was determined relative to that of an azoxybenzene (Fisher Scientific, 98 %) actinometer.¹⁴⁷ The actinometry experiment was performed by photolyzing an ethanol solution consisting of 0.2 mM azoxybenzene/6.0 mM KOH. The absorption of the photoisomerization product of azoxybenzene was followed at wavelength of 458 nm (extinction coefficient $\epsilon = 7600 \text{ L mol}^{-1} \text{ cm}^{-1}$).

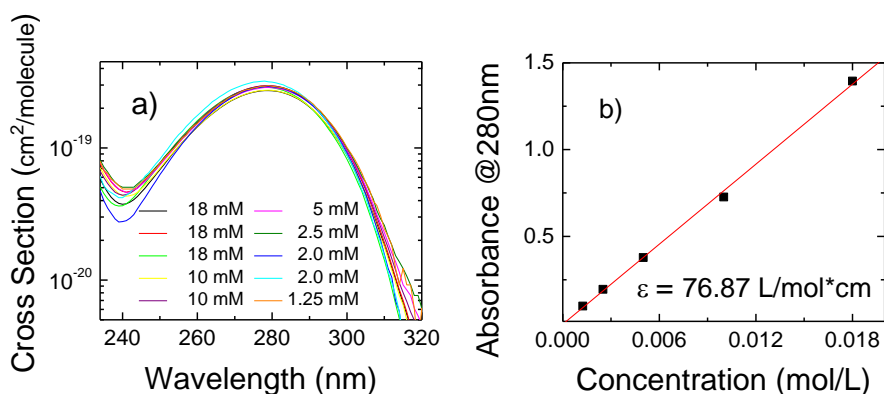


Figure 4. a) Absorption cross sections of PA in water obtained at concentrations varying from 1.25 mM to 18 mM. b) A representative Beer-Lambert plot for PA in water at the peak of the $\pi^* \leftarrow n$ band.

The photolyzed samples were analyzed using different analytical techniques. First, five identical 5.00 mM PA solutions were prepared and photolyzed for 0, 30, 60, 90, and 120 minutes. The photolyzed samples were subsequently derivatized by Fischer-esterification to produce an ester, by refluxing for 1 hour with either methanol (Fisher Scientific, Optima, HPLC grade) or ethanol (Rossville Gold Shield) and using HCl (J. T. Baker) as a catalyst. This method esterified only products that possessed a carboxyl group. Cyclohexane (Fisher Scientific, Spectranalyzed) was used to extract the ester and other non-polar products to the organic phase, and the samples were injected to GC-CIMS (Waters GCT-premiere, flow rate 1.5 mL/min, DB-5 30 m column, 1 μ L injection amount) using the positive-ion chemical ionization mass spectrometry (CIMS) mode with NH_4^+ as the ion reagent. Accurate mass measurements were used to determine the molecular formulas of the detected species. The observed ionization mechanisms were NH_4^+ addition and protonation. The m/z values were accurate to 3 Da (resolving power = 7000) enabling determination of ion formulas. The molecular formulas of the product compounds were obtained by removing NH_4^+ or H^+ from the formulas of the corresponding ionized species.

Next, the photolyzed samples were injected to High-Performance Liquid Chromatography (HPLC) instrument to separate the different photolysis product fractions to further analyze with Nuclear Magnetic Resonance (NMR) spectroscopy. For the HPLC product separation, a 10 mM PA solution was photolyzed for 60 min. A gradient method was used in the

separation. Solvent A was HPLC grade water (Fisher Scientific, Omnisolv, HPLC grade) with 2 % acetonitrile (EMD chemicals, HPLC grade) and 0.2 % acetic acid (Aldrich, 99.7%). Solvent B was acetonitrile with 0.2 % acetic acid. The column was a Phenomenex Luna C18 semi-prep column with a 500 μ L injection loop. The absorption spectra of the eluding species were followed in real-time with a photodiode array detector (PDA, Shimadzu SPD-10Avp, 200-650 nm). Fractions of different photolysis products that eluded at different retention times were collected in scintillation vials (collection time per fraction \sim 20 s, of the order of the FWHM of the peaks). The collection was repeated multiple times in order to collect sufficient amounts of the separated products for further analysis. The collected fraction was evaporated in a rotary evaporator at 45 $^{\circ}$ C and the residue re-dissolved in CD_3CN (Aldrich, D 99.8%, 0.03% TMS) or CDCl_3 (CIL, D 99.8%, 0.05% TMS) for NMR analysis. Also a time-dependent experiment was carried out, where the PA sample was photolyzed in 10 minute intervals and injected into the HPLC instrument. This experiment was designed to provide information on the order of the photolysis products, but the outcome was not conclusive. The main product started forming within the first 10 minutes, but no clear difference was observed as the other product peaks started to appear.

NMR-spectroscopy was used to identify the photolysis products. Three different sets of NMR experiments were performed, with and without prior separation of the photolysis products with HPLC. In the first set of experiments, four 18 mM PA/ D_2O solutions were prepared and photolyzed for 0, 15, 60, and 120 minutes. H1 and C13 NMR-spectra were recorded using Bruker Avance 500 MHz NMR-spectrometer equipped with a highly sensitive, Three Channel Inverse (TCI) cryoprobe. In the second set of experiments, PA was photolyzed in CDCl_3 to compare the NMR spectra with aqueous photolysis, as well as improve the quality of the NMR spectra. Four 18 mM samples were photolyzed for 0, 30, and 45 minutes and H1 and C13 NMR spectra recorded. Blank experiments with photolyzed CDCl_3 were carried out also to rule out any possible solvent photochemistry. In the third set of experiments the photolysis products were separated using HPLC as previously described before performing the NMR analysis. Pure PA NMR spectra were recorded also in CD_3CN .

The photolyzed samples were analyzed also using Liquid Chromatography ElectroSpray Ionization Mass Spectrometry (LC-ESI-MS), where the photolysis products were separated by liquid chromatography and the fractions analyzed by mass spectrometric methods. For the LC-ESI-MS, an 8 mL solution of 10 mM PA/HPLC grade water was photolyzed and the photolyzed sample concentrated by evaporation with rotary evaporator (from

8 mL to 4 mL). The sample was injected to LC-ESI-MS instrument (Waters LCT Classic, LC:Agilent 1100, autosampler:Gilson 231XL) and both positive (+) and negative (-) ion mode mass spectra were recorded covering mass range of 100-1000. A 25 cm x 2 mm Luna C18(2), 3 μ m particles column was used for the separation, injection amount and flow rate being 10 μ L and 0.2 mL/min, respectively. The solvents were the same as described in the HPLC-PDA section, and a gradient program similar to that of the HPLC setup was used. The observed ionization mechanisms were Na⁺ addition and/or protonation in the (+) mode and deprotonation in the (-) mode. In addition to the photolyzed samples, chromatograms of pure PA and the HPLC separated main photolysis product (PA isomer) were recorded for comparison.

2.3 Gas Phase Photolysis of *cis*-Pinonic Acid

To provide comparative results between the direct aqueous and gas phase photolysis, gas phase photolysis experiments were performed using Proton Transfer Reaction Time of Flight Mass Spectrometer (PTR-ToF-MS, Ionicon Analytik). Due to the low vapor pressure of PA, experiments were done with PA methyl ester (hereafter abbreviated as PAMe). PA was derivatized using the already described Fischer esterification to produce the ester (Section 2.2). Evaporation of the cyclohexane extract resulted in a clear liquid (PAMe) and some residual PA. The gas phase photolysis set-up consisted of a 230 L Teflon FEP bag with several feed through inlets for the sample injection lines, air and vacuum lines, and sampling lines. PAMe was injected into a separate 9L Teflon bag and evaporated into the main bag with 8-10 SLM flow of dry air to avoid issues of introducing the liquid ester into the photolysis bag. The concentration of the ester was monitored in real-time with the PTR-ToF-MS instrument. After the ester concentration had stabilized, the content of the bag was photolyzed for 4 hours with UV-lights (10 Philips UV-B lamps, TL 40W/12 RS). A diagram of the setup and the spectrum of the UV-lamps are shown in Fig. 5. Acetone was used as an actinometer in order to determine the gas-phase photolysis quantum yield of PAMe. As the cross sections of PAMe were not measured quantitatively in the experiments, acetone cross sections were used instead. Gas phase acetone absorption cross sections and photolysis quantum yields required for the calculations were taken from Ref. 3.

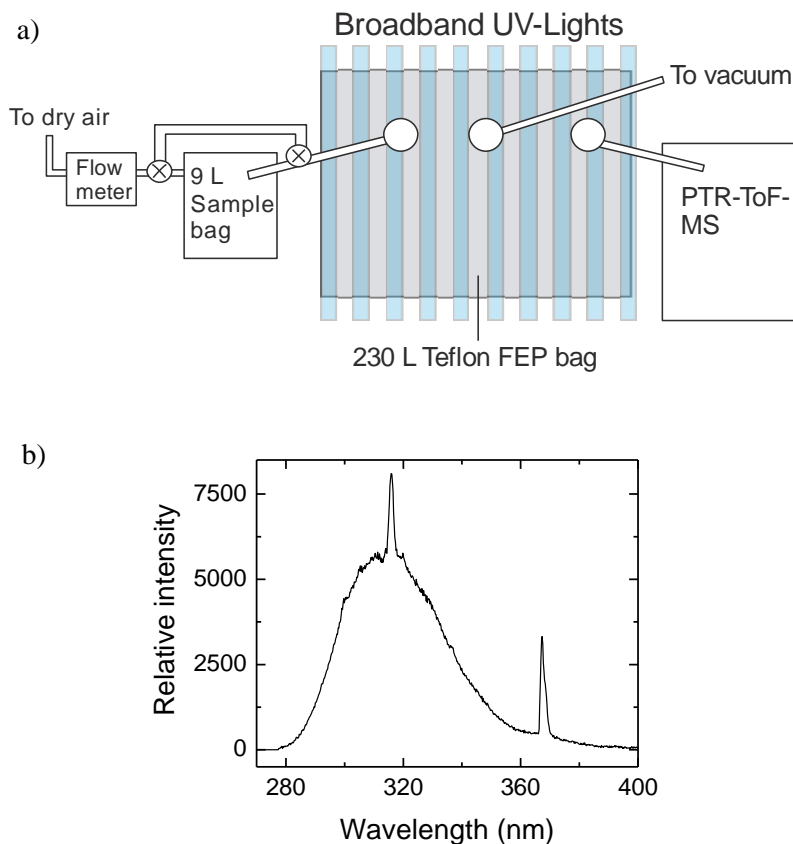


Figure 5. a) A schematic diagram of the gas phase photolysis setup. The vertical bars behind the Teflon bag represent a bank of UV-B lamps (Philips, TL 40W/12 RS). The intermediate 9 L bag is used to prevent injecting any liquid into the main bag. b) The spectrum of the UV-lamps used in the gas-phase measurements.

2.4 Comparison of *cis*-Pinonic Acid Loss Mechanisms

In addition to investigating the photolysis mechanism and products of aqueous PA, two sets of simulations were performed to shed light to the atmospheric relevance of the photolysis reaction compared to other sinks for PA. The first set of calculations compared the disappearance of PA due to direct aqueous photolysis, direct gas phase photolysis, aqueous OH-oxidation, and gas phase OH-oxidation. The method used in these

calculations was adapted from Refs. 119 and 121. PA was assumed to partition to the aqueous phase (clouds and fogs) by obeying Henry's law equilibrium, the Henry's law constant was predicted using HENRYWIN v3.20¹⁴⁸ developed by the Environmental Protection Agency (EPA). The rate of dissolution to clouds depends on their liquid water content (LWC), which varies quite dramatically. The largest value routinely found in the atmosphere (0.5 g m^{-3})^{5,149} was used in these calculations. The rate constant for the direct photolysis of PA in aqueous phase was determined from the measured absorption cross sections. As no gas-phase absorption cross sections were measured for the gas phase PA, data of gas phase acetone from Ref. 3 were used instead. Structure activity relationships developed by Monod and Doussin^{150,151} and Kwok and Atkinson¹⁵² were used to determine the rate constants of the aqueous and gas phase OH- oxidation. The actinic flux as a function of solar zenith angle (SZA) was also required, and NCAR Tropospheric Ultraviolet & Visible Radiation Model (Edition 4.4)¹⁵³ was used to predict it at an global average albedo value of 0.154. The gas phase OH concentrations were correlated to the O¹D photolysis rates.¹⁵⁴ The values of 10^{-13} and 10^{-14} M were used for aqueous daytime and nighttime OH concentrations, respectively.⁹⁸ As no information about the aqueous OH concentration variations as a function of SZA was available, similar correlation to that of the gas phase was used.

The second set of calculations looked at the fate of PA in a wet aerosol, where no clouds or fog were present. In this case the assumptions were the following. Typical organic aerosol mass concentration of $20 \text{ } \mu\text{g m}^{-3}$ and particle water content of $50 \text{ } \mu\text{g m}^{-3}$ were assumed and the gas- to organic phase partitioning for PA was calculated from standard absorptive partitioning model.^{155,156} The choice of the vapor pressure of PA ($C^* = 5.2 \text{ } \mu\text{g/m}^3$)¹⁵⁷ was justified by comparison to previous field studies.¹⁵⁸ Gas- to aqueous aerosol phase partitioning was approximated using Henry's law, and it was assumed that the organic and aqueous aerosol phase were not connected. A negligible OH concentration inside the particles was also assumed. In the aqueous-aerosol phase calculation the experimental PA parameters were used. In the case of organic-aerosol phase calculation, parameters of gas phase acetone were used to model the properties of gas phase PA.

2.5 Photochemistry of SOA Matrices and Aqueous Solutions

The setups used for the SOA experiments are shown in Fig. 6. The SOA material was prepared by dark ozonolysis of α -pinene (Alfa Aesar, 98%) and d-limonene (Acros Organics, 98%) in a 20 L flow tube as described in Ref. 159. The SOA particles were collected through a 1-m charcoal denuder using a Sioutas impactor¹⁶⁰ (single stage D) on a 25 mm CaF₂ window. A typical operation time of the flow tube was 3 hours, producing 8-10 mg of SOA material. The mass of the SOA was determined by weighing the window before and after the collection. The pure SOA samples were prepared by sandwiching the SOA material between two CaF₂ windows and pressing them together while gently heating. In the experiments where 24-DNP was embedded in the SOA film, a 100 μ L droplet of 0.01 M 24-DNP (Sigma-Aldrich, 99.9%, Pestanal analytical standard, with \sim 0.3 mL H₂O/g) in methanol (Fisher Scientific, Optima, HPLC grade) was added directly on the window where the SOA material was collected to dissolve the organic material, and the methanol was allowed to completely evaporate by waiting for 30 min. This evaporation time was chosen by testing different wait times and following the 290 nm signal. At wait times 30 min and higher the signal was stable immediately, suggesting that no further solvent evaporation was taking place. The amount of 24-DNP was chosen such a way, that it was unlikely for it to affect the physical properties of the matrix (such as its viscosity), but absorbed the photolyzing radiation more strongly than the molecules in the SOA matrix. The 24-DNP:SOA mass ratio in these experiments was typically \sim 1:50. Figure 7 shows photographs of the samples at different stages of the experiments.

The 24-DNP/octanol samples were prepared by placing a 15 μ L droplet of 27 mM 24-DNP/octanol (Sigma-Aldrich, 99%) solution between the CaF₂ windows. The actinometer film was prepared similarly by placing a 15 μ L droplet of octanol solution consisting of 63 mM azoxybenzene/29 mM KOH between the CaF₂ windows.

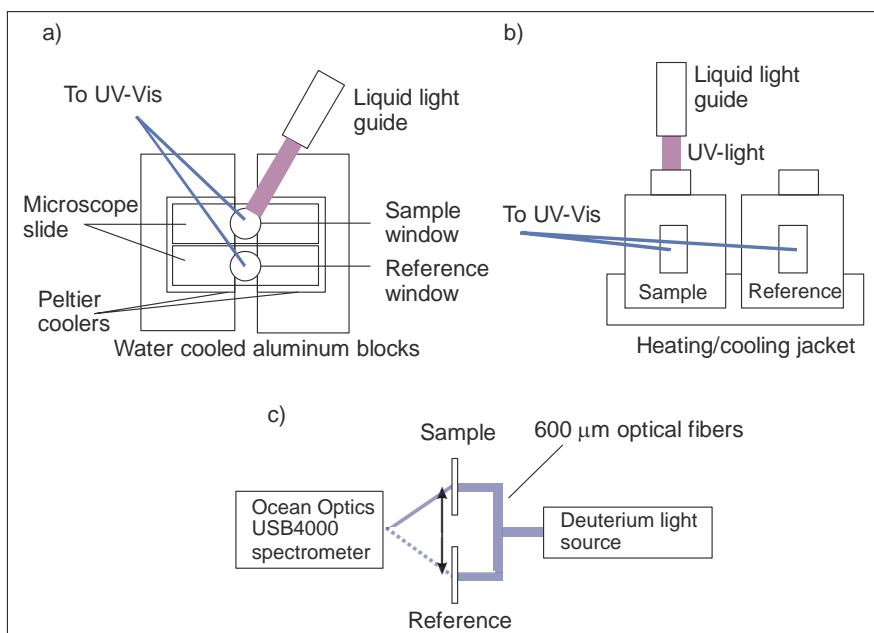


Figure 6. Experimental setup for temperature controlled SOA matrix photolysis (a) and aqueous SOA photolysis (b). Both setup compartments were purged with dry-air. c) Side view of the sample slides of the SOA matrix photolysis setup showing the locations of the delivery and collecting fibers.

Optimizing the 24-DNP/SOA sample preparation method was a challenging task. Several approaches were attempted prior to the adoption of the successful method described above. The quality of the sample films turned out to be extremely sensitive to the amount of methanol used, the actual physical movement of the windows during “sandwiching”, and the amount of SOA used. Initially, the SOA was dissolved in 24-DNP/methanol solution in a separate vial, and this solution was added in parts to the window to evaporate. In this approach the uncertainty of the SOA mass was quite large, as some of the material was evidently staying in the vial. In another approach the CaF₂ windows were gently heated using a heat gun after the evaporation process. This seemed to change the properties of the film, as the SOA material became evidently less viscous (this observation was based on the easiness of moving the windows relative to each other after the “sandwiching”). Annealing in an oven at 50°C was also attempted, but this resulted in poor film quality. The attempt to make films with less material (conserving the 24-DNP:SOA mass ratio) to reduce the absorption well below 1 (this requirement will be discussed later) led to films that produced

the physical changes (“islands”) very fast, and no meaningful photolysis experiments were possible.

The windows containing sandwiched SOA, 24-DNP/SOA or 24-DNP/octanol were placed directly on a temperature controlled microscope slide inside a dry-air purged aluminum box. The dry air prevented any water condensation in experiments well below room temperature. The windows were cooled down via direct heat withdrawal from the microscope slide, the temperature range being -18 °C and 25 °C in these experiments. The cooling was done by combining a circulating water cooler (50:50 ethylene glycol:water or 70:30 methanol:water) connected to an aluminum heat sink and two 50 x 50 mm Peltier coolers controlled by separate temperature controllers. The temperature was monitored using a type-K thermocouple mounted to the microscope slide. The samples were photolyzed using a 150 W Xe arc lamp, the actinic radiation was delivered through a liquid light guide fiber and projected to the sample windows under a 15° angle. Two different filtering configurations were used. The first was a 300 nm band pass filter (40 nm FWHM, # NT67-817) that was used to isolate a band of the actinic radiation of interest for tropospheric photochemistry (280-400 nm), as well as prevent heating of the sample. The second configuration was a 295 nm long pass filter (Schott WG 295, Edmund Industrial Optics #46-418) with a Schott BG1 blue filter, which was chosen as a compromise between producing more intense radiation for photolysis, and again producing a band of the actinic radiation relevant for tropospheric conditions. An Ocean Optics USB4000 spectrometer combined with a deuterium light source and 600 µm optical fibers was used to follow the photolysis as a function of time [see Fig. 6 (c)]. The reference spectrum for absorption measurements was obtained by recording the background spectrum prior to the photolysis in the sample position using the same pair of CaF₂ windows that were used for sample preparation. The experimental setup also allowed another background spectrum measurement option, where the optical fiber connected to the spectrometer was shifted above the reference window (see Fig. 6 (c)). However, the latter method was only used in a few experiments, as the first one provided less interference to the highly sensitive optical fibers. In case of the SOA and 24-DNP/SOA experiments, the background was simply the identical pair of windows. In the case of 24-DNP/octanol studies and actinometry, a 15 µL droplet of octanol was used as the reference spectrum. The azoxybenzene actinometer was photolyzed under the same experimental conditions, similarly as in the PA experiments described in section 2.2 .

For the aqueous SOA studies the SOA material was prepared in the flow reactor, but instead of the CaF_2 windows, the particles were collected on a Teflon filter. The SOA material was extracted in HPLC grade water by sonication, and the concentration of the samples were kept constant so, that the absorbance of the SOA/water solution was ~ 0.2 (approximately 0.7 mg/mL). This corresponds to a mass absorption coefficient (MAC) value of $\sim 660 \text{ cm}^2/\text{g}$. This value was consistent with previous measurements of α -pinene SOA.¹⁵⁹

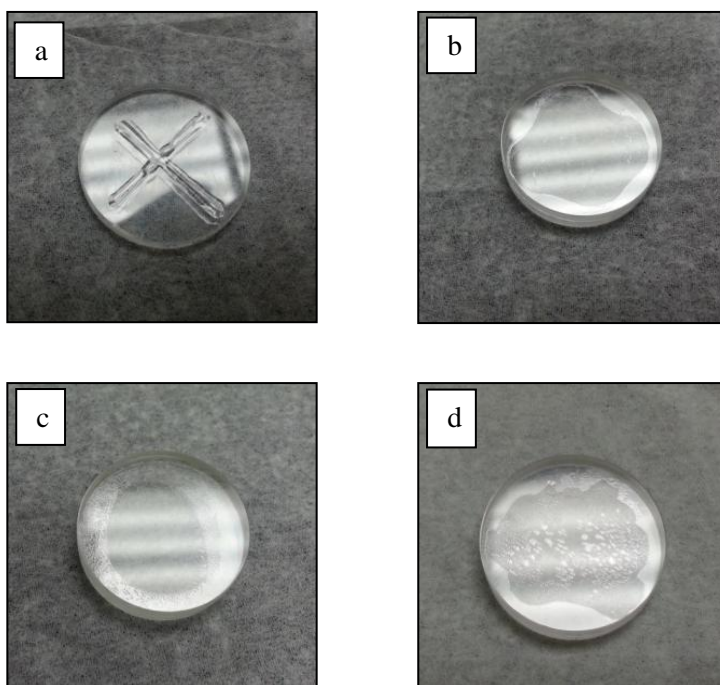


Figure 7. a) SOA material prepared in a flow reactor via α -pinene ozonolysis reaction and collected with a Sioutas impactor on a CaF_2 window b) the pure SOA film after “sandwiching” the SOA material between two CaF_2 windows c) SOA/24-DNP film prepared by evaporating a methanol solution of SOA/24-DNP as described in the text d) formation of “islands” in the SOA film during a control experiment.

The apparatus used for photolysis of the aqueous α -pinene SOA solutions consisted of a Shimadzu constant temperature cell holder (5°C - 35°C in these experiments, controlled by a recirculating water chiller) inside a Shimadzu

model 2450 UV–Vis spectrometer. The cell holder was modified to hold a 3/8” liquid light guide that delivered actinic UV-radiation (280–400 nm) from a 150 W xenon arc lamp housing (Newport model 66902). The aqueous samples were photolyzed directly in a quartz cuvette from the top. The samples inside the cuvette were constantly mixed with a micro stirrer (2-mag USA, MIX control eco, #MF90100). Absorption spectra of the solution were recorded periodically, with nanopure water in an identical quartz cuvette as a reference. The UV-Vis spectrometer’s sample compartment was continuously purged with dry air to prevent water condensation on the outside surfaces of the cuvettes during experiments that were carried out at reduced temperatures. During photolysis, the sample cuvette was constantly purged with dry argon to remove dissolved oxygen; purging was paused during collection of absorption spectra. The same setup was also used to measure the photolysis rate of a 4×10^{-5} M 24-DNP/water solution acidified to pH \sim 1.4, but with the same filter combination as in the SOA film experiments and without Ar-purging. For the actinometry experiments, an ethanol solution consisting of 0.2 mM azoxybenzene/6.0 mM KOH was photolyzed under the same conditions, also without for Ar purging.

3. Computational Methods

3.1 Isomerization and Ionization of N_2O_4 on Model Ice and Silica Surfaces

The starting point of the study of N_2O_4 on atmospherically relevant surfaces was the assumption that symmetric N_2O_4 isomerizes on the surfaces of interest based on the model suggested by Finlayson-Pitts *et al.*⁴¹:



The model ice surface utilized in Article II consisted of $n = 20$ water molecules that were organized to form a cluster of four $(\text{H}_2\text{O})_5$ rings. The choice of this cluster was justified by previous studies, where it has been used to successfully describe atmospherically relevant ice surfaces.^{161,162} It is important to note that interface reactions are believed to be local processes, thus such clusters are expected to provide a model for studying these reactions with a reasonably good level of theory. It was also assumed that the cluster structure does not change during the adsorption to any significant extent. The model system for the silica surface was simply an $\text{Si}_8\text{O}_{16}\text{H}_{12}$ particle, which is a $(\text{SiO}_2)_8$ cluster with surface hydrogens resembling the crystal structure of quartz.¹⁶³

Second-order Møller-Plesset perturbation theory (MP2) and density functional theory (DFT/B3LYP functional) were used to study the structures and spectra of N_2O_4 (symm) and ONONO_2 (asymm) molecules, the transition state between the two conformers, and the NO^+NO_3^- ion pair on model ice and silica surfaces. The transition state (a first-order saddle point) between symmetric and asymmetric N_2O_4 was determined by optimizing a guess structure with a transition vector value of 1. The TRIM method used in Turbomole package attempts to maximize the energy along one of the Hessian eigenvectors, while minimizing it in all other directions.¹⁶⁴ The best choice for the eigenvector to follow was the one with a negative eigenvalue (imaginary frequency). The level of calculation applied was B3LYP/def2-TZVP with DFT-D2 dispersion correction. The Intrinsic Reaction Coordinate (IRC) path, which is the minimum energy path connecting the saddle point to reactants and products, was determined for the isomerization reactions. With MP2, aug-cc-pVDZ and 6-311**G(d,p) basis sets were used, as they were known to perform reasonably well in describing water systems. For B3LYP calculations def2-TZVP and 6-311++G(d,p) basis sets were used, and DFT-D2 dispersion correction was added for selected systems. The IRC calculations were performed using B3LYP functional with 6-311++G(d,p) and DZVP basis sets. The basis sets were chosen based on a comparison between experimental and computational structures and spectral data of the isolated N_2O_4 molecule. Partial charges were calculated using natural population analysis (NPA). Zero-point energy correction was taken into account in all energy calculations. The computations were carried out using Turbomole (v.6.2)¹⁶⁵ and Gaussian (v.03)¹⁶⁶ program packages on the Greenplanet cluster operating at the Physical Sciences Modeling Facility, UC Irvine.

3.2 The Photoexcitation Dynamics of PA and Hydrated PAMe

The PA photolysis was also approached by computational methods. The photochemical reaction processes were followed in time both in absence and in presence of water molecules employing semiempirical on-the-fly molecular dynamics. Orthogonalization-corrected Method 2 (OM2) was chosen based on its past success in similar systems. Number of trajectories was 100, which was large enough to provide good statistics for different reaction events. When water was present, PA methyl ester (PAMe) was used instead of PA to prevent the carboxylic acid group from attracting the water molecules away from the photochemically active carbonyl group. As the focus in Article III was mainly the photochemistry taking place at carbonyl-part of the molecule, and the substitution was not assumed to affect the photodissociation dynamics significantly.

The initial optimization of the structures of PA, PAMe, and PAMe \cdots (H₂O)_n, n = 1-5 were performed with Møller-Plesset second order perturbation theory (MP2) using cc-pVDZ basis set,¹⁶⁷ and the resolution of the identity approximation (RI)¹⁶⁸ implemented in Turbomole¹⁶⁵ was used to get the electron-repulsion integrals. Excitation energies were calculated using the Algebraic Diagrammatic Construction method 2 (ADC2).¹⁶⁹ The potential energy surface calculations were performed using the semiempirical OM2 method.¹⁷⁰ The advantage of OM2 over other semiempirical methods is the fact, that the excited states can be treated with the equivalent OM2/MRCI (Multireference Configuration Interaction) methods.¹⁷¹ The active space for all the studied systems was chosen based on comparison to the orbital excitations in ADC(2) calculations.¹⁶⁹ Photoinduced processes of PA and PAMe \cdots (H₂O)_n, n = 1-5 were simulated using Modified Neglect of Diatomic Overlap (MNDO).^{172,173} The 3-step simulation process progressed the following way. First, ground state dynamics were performed in order to sample the initial configurations. Secondly, vertical transition took place to the first excited singlet state followed by the ISC to the triplet state. Third, the excited state dynamics were run on the excited triplet state. The excited state dynamics on the excited singlet state were not included (it was assumed that no photochemical changes will take place before the ISC, as it is well established that triplet electronic states are more significant for carbonyl photochemistry).⁷ The exclusion of the singlet excited state is discussed in detail in Ref. 174, where photodissociation dynamics of structurally similar aldehyde pentanal were studied. The gap between the excited singlet and triplet state was calculated from the ground state dynamics sampling the initial configurations. The ISC was assumed to take place where the singlet-

to-triplet gap was smallest (0.51-0.56 eV for PA and 0.37-0.89 for PAMe \cdots (H₂O)_n, n = 1-5). A total of 100 geometries with the smallest singlet-to-triplet gaps were chosen as initial conditions for the dynamics on the triplet state. The sampling of the initial conditions for the dynamics were performed by running a trajectory on the ground state for 10 ps at 300 K utilizing the velocity Verlet algorithm with a 0.1 fs time step and the OM2 potential. In the case of PAMe \cdots (H₂O)_n, n = 1-5, the temperature was set to 200 K to prevent evaporation of the water molecules. The initial velocity of the atoms in the triplet state dynamics was determined using Monte Carlo sampling of kinetic energy, which was based on the assumption that thermal equilibrium was reached immediately after the ISC. The Monte Carlo kinetic energy was converted to a temperature of 300 K, giving the atoms their initial velocity. The adiabatic dynamics were run for 100 ps, one from every starting geometry. For PAMe \cdots (H₂O)_n, n = 1-5 the dynamics were tested also at 200 K. The cleavage distance for the C-C $_{\alpha}$ bond breaking was assumed to be 2.5 Å (distance where the chemical interaction between the fragments is negligible).

4. Results and Discussion

4.1 Low Temperature Formation of HArF

4.1.1 Precursors and Preparation

The spectra of the precursor molecules HD and DF are presented in Fig. 8. These bands are in agreement with previous studies of HF.¹⁷⁵ Upon photolysis with a Kr lamp, these bands decrease and the (ArHAr)⁺ absorptions grow.¹⁷⁶

After the photolyzed samples were annealed, the characteristic triplet-absorption of the H-Ar stretching mode of the HArF molecule was observed. These bands at 1965.7, 1969.4, and 1972.3 cm⁻¹ belong to the unstable configuration of HArF, whereas bands observed at 2016.3, and 2020.8 cm⁻¹ belong to the stable configuration of HArF.^{18,19} Figure 9 (a) shows the formation of these characteristic bands. Although the major part of the unstable configuration is formed during the annealing, a small amount of HArF was observed directly after photolysis.^{16,19} In the following analysis, this initial HArF formation was subtracted from the annealing induced formation, so it has no effect on the low temperature formation kinetics.

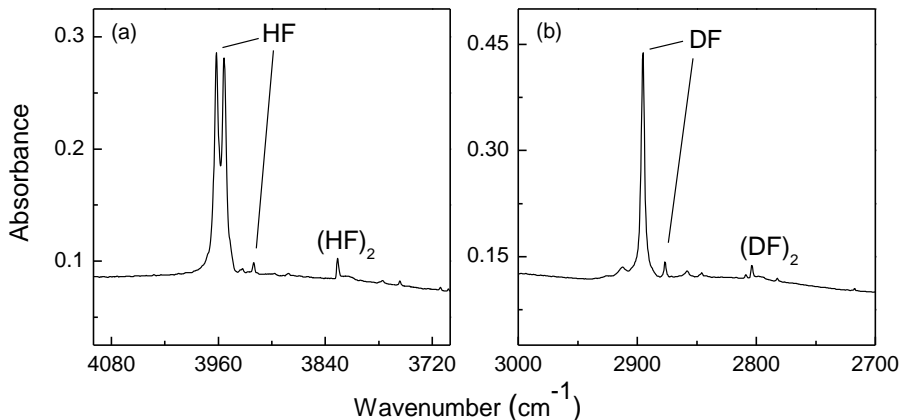


Figure 8. IR spectra of the precursor molecules HF (a) and DF (b) in an Ar matrix. The spectra are measured at 8 K.

The different configurations, referred to as the unstable and stable HArF, are related to different local matrix structures.²⁷ The unstable configuration is formed during annealing the sample at 20 K after initial photolysis, and further annealing above ~ 28 K converts the unstable HArF to the stable configuration. This intriguing solid state phenomenon is caused by thermal relaxation of the surrounding matrix,^{18,19,29} and the shift in the absorbance is significant. The suggested experimental and theoretical mechanisms for this behavior will be discussed in more detail in the following sections. In Fig. 9 (a) is also shown the librational band (L) of HArF in solid Ar matrix, which is also caused by the surrounding environment.²⁸ The HArF molecule is trapped between the host atoms, which restrict its motion inside the matrix. Thus the librational band is caused by the hindered rotation of the molecule. Experimental observations highlight the thermal modification of the IR absorption bands.²⁸ The librational band is not unique to argon matrices, similar features have been observed also in the case of HXeBr and HKrCl in Xe and Kr matrices, respectively.¹⁷⁷

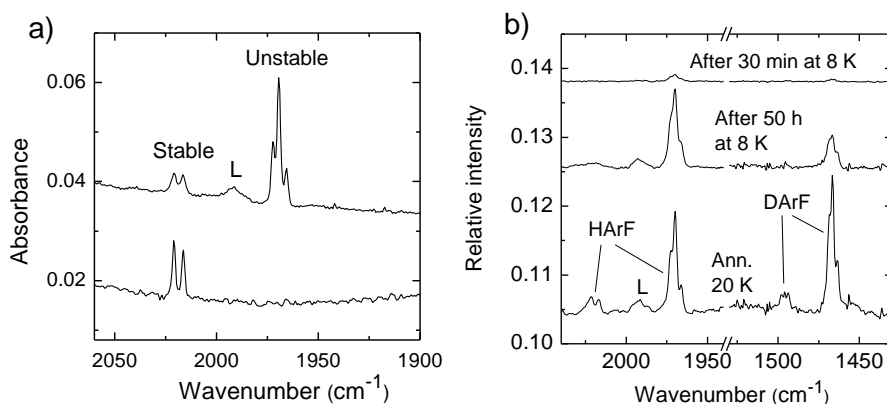


Figure 9. (a) Formation of HArF upon thermal annealing. In the upper trace (ann. at 20 K), both unstable and stable HArF configurations are visible. In the lower trace (ann. at 30 K), only the stable form is present. (b) Low-temperature formation of HArF and DArF. The upper trace is measured after 30 min waiting at 8 K and the middle trace after 50 h waiting at 8 K after photolysis. It should be noted, that the unstable configuration of HArF is mainly formed at 8 K. The lower trace shows the spectrum after additional annealing at 20 K. The band marked with L is due to the librational motion of the HArF molecule in solid argon.²⁸ The spectra are measured at 8 K. The HF(DF)/Ar matrix was preliminarily photolyzed with a Kr lamp. The photolysis induced absorptions are subtracted from the spectra shown in (b).

4.1.2 Low Temperature Formation

The main goal in Article I was to gain detailed understanding of the low temperature formation behavior of HArF. When considering reactions that take place at temperatures as low as ~ 10 K, non-classical phenomena cannot be neglected as a possible reaction mechanism. Fig. 9 (b) presents the formation of HArF and DArF at 8 K, and the result of the subsequent annealing at 20 K. The formation kinetics were studied at varying temperatures, and it was observed that although the formation rate slows down at lower temperatures, the formation reaches completion even at the lowest experimental temperature of 8 K. This is further supported by the subsequent annealing, which does not increase the HArF amount significantly. When the HArF formation was compared to its deuterated form, it was observed that DArF molecule forms significantly slower (by a factor of ~ 50) [Fig. 10 (a)]. The increased rate of formation as a function of increasing temperature was observed for both HArF and DArF, as shown for HArF in Fig. 10 (a). When looking at kinetics of slow chemical processes at

low temperatures, it was necessary to exclude the possible effect of the broadband IR-radiation from the globar of the spectrometer. This negligible effect presented in Fig. 10 (b), where the formation of HARF is shown at 10 K with both under the globar radiation and in dark conditions.

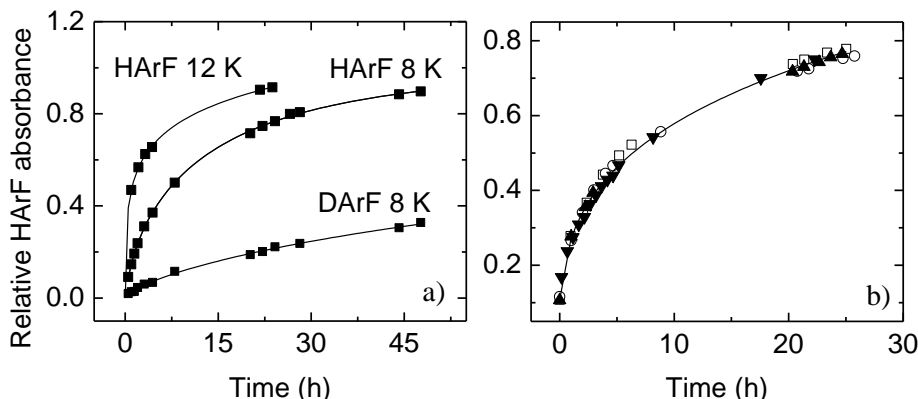


Figure 10. (a) Formation of unstable HARF as a function of time at different temperatures (8, 10, and 12 K). Formation of unstable DArF is shown at 8 K demonstrating a strong isotope effect. The spectra were measured at the annealing temperatures. The lines are stretched-exponential fits. (b) Demonstration of the negligible effect of broadband IR light on the HARF formation at 10 K. The solid and open symbols represent the data obtained with the closed and open Globar source between the measurements, respectively. The integrated absorbance was normalized by the value obtained after annealing at 20 K and the values after photolysis were subtracted. These experiments were done using relatively low HF concentrations (~1:2500) to further isolate individual HARF molecules.

4.1.3 Decay of (ArHAR)⁺ and (ArDAR)⁺ and Implications of Tunneling Reaction

When looking at chemical processes at very low temperatures, the classical contribution will decrease and tunneling processes start to dominate. Several chemical phenomena are characteristic for tunneling mechanisms. The systems studied in Article I demonstrate this behavior, and these “tunneling fingerprints” are now discussed.

The (ArHAR)⁺ ions are formed upon photolysis of the sample, and they decay as a function of time. In Article I the decay kinetics of these ions were studied and compared to the formation kinetics of HARF. As the connection between

these two species has been under debate previously, the main findings of this relationship will be discussed. The decay of the $(\text{ArHAr})^+$ and $(\text{ArDAr})^+$ is shown in Fig. 11. The decay process is observed to have a strong isotope effect, seen as significantly slower decay of the deuterated form. While the $(\text{ArHAr})^+$ ion is almost completely disappeared upon waiting for 8 hours at 8 K, the decay of the $(\text{ArDAr})^+$ is practically negligible after 50-hour waiting period. The decay remains small even after further annealing at 20 K.

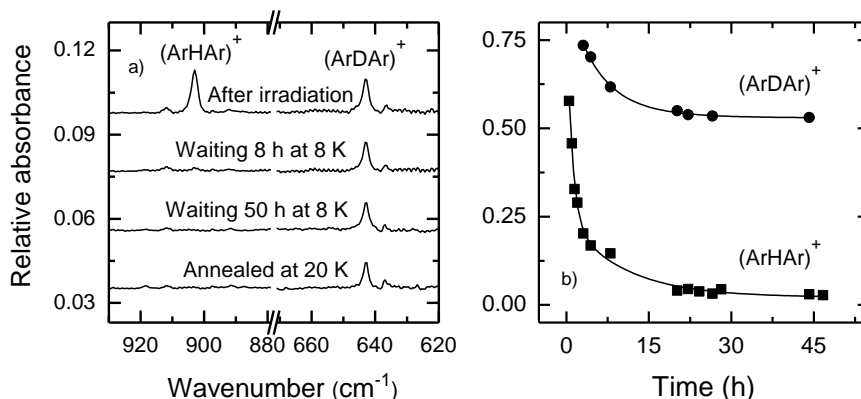


Figure 11. a) IR spectra of $(\text{ArHAr})^+$ and $(\text{ArDAr})^+$. The upper spectrum was recorded after irradiation. The two middle spectra represent the decay at 8 and 50 h after photolysis, respectively. The lower spectrum is recorded after annealing the sample at 20 K. All the spectra were measured at 8 K. b) Decay of $(\text{ArHAr})^+$ and $(\text{ArDAr})^+$ at 8 K.

The HArF formation is enhanced by elevated temperatures. The decay of the $(\text{ArHAr})^+$ ions is somewhat faster at higher temperatures, but less efficient than the effect on the HArF formation kinetics. The temperature dependence of the formation and decay of these species was approached by introducing the Arrhenius behavior which describes the temperature dependence of reaction rates.¹⁷⁸ Figure 12 shows the Arrhenius plots of the HArF and DArF formation, as well as the decay of the $(\text{ArHAr})^+$ ions. It can be seen from the figure, that the behavior of these species is quite different. The formation of DArF is significantly slower compared to HArF at 8 K, whereas the formation rates become comparable by 15 K. The Arrhenius plot for the decay of the $(\text{ArDAr})^+$ was not achieved due to the extremely slow decay of this species. These Arrhenius plots provide means to determine the activation energy for the formation from the high temperature points. These values were $E_{\text{act}} = (333 \pm 25) \text{ cm}^{-1}$ and $E_{\text{act}} = (322 \pm 18) \text{ cm}^{-1}$ for HArF and DArF, respectively.

The temperature dependence of the formation of HArF and DArF start to deviate from the Arrhenius behavior when the temperature is lowered. This low temperature limit of the formation can be seen in Fig. 12 as a plateau at low temperatures, and a thermally activated part is seen with temperatures above 12 K. The observed low-temperature limit is a known fingerprint of a tunneling mechanism.^{179,180}

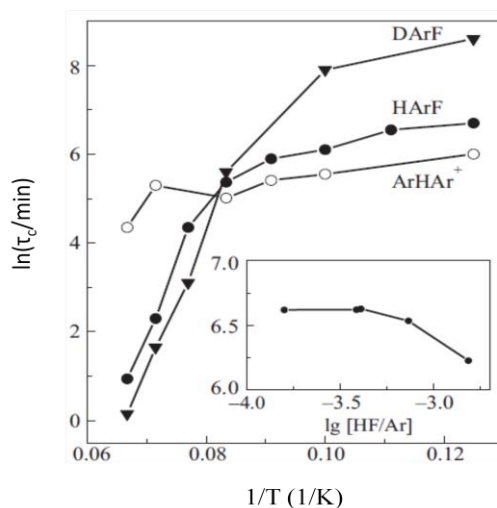


Figure 12. Arrhenius plot for unstable HArF and DArF formation and (ArHAr)⁺ decay. The formation time of unstable HArF and DArF was estimated at 0.63 and 0.45 levels of the integrated intensity obtained after annealing at 20 K, respectively. The insert shows the HF-precursor concentration dependence of the HArF formation at 10 K. Matrices were deposited at 12 K and the Ar/HF ratios (~1:2000) were estimated using the molar absorptivity of gaseous HF.¹⁸¹

The other indication of the non-classical behavior is the strong H/D isotope effect observed in both the formation of HArF and DArF [Fig. 10 (a)], and the decay of (ArHAr)⁺ and (ArDAr)⁺ species [Fig. 11 (b)]. This isotope effect in case of HArF/DArF also suggests that the formation is not affected by mobile F atoms and/or matrix vacancies. Tunneling of hydrogen atoms may occur only through a short distance, which further supports the locality of both the HF photodissociation and HArF formation in solid argon (discussed in the following section). It seems viable to assume that HArF is formed at low temperatures from the same H atoms as upon annealing at 20 K. This conclusion is supported by the stability of the HArF concentration upon annealing at 20 K after a long period at 8 K.

Another interesting question addressed in Article I was the relationship between the formation of HArF and the decomposition of (ArHAr)⁺. Although it is possible that the neutralization of the ionic (ArHAr)⁺ species by electron transfer from F⁻ could kindle the formation of HArF via the neutral H + Ar + F reaction,³² the distinct kinetics observed in these systems show that they are not directly connected. The parameters extracted from stretched-exponential fits from the formation of HArF and the decay of (ArHAr)⁺ at 8 K were different, which also was in agreement with previous conclusions.³² In addition to this, the Arrhenius plots of these species shown in Fig. 12 clearly demonstrate different temperature dependencies. The decay of the (ArHAr)⁺ was evidently less sensitive to the matrix temperature, and the decay of (ArDAr)⁺ was significantly slower than the formation of DArF [Figs. 11 (a) and 9 (b)] .

4.1.4 Locality of the Photolysis

As tunneling can occur only through short distances, the scale of the photolysis distance bears relevance to the suggested HArF formation mechanism. In essence, the HArF formation can be a result of either global (long-range) or local (short-range) process with respect to atomic mobility and thermal mobilization of both H and F atoms is plausible. Local solid-state processes differ from the global processes energetically.^{29,182} Global formation occurs via atomic diffusion over relatively long distances (compared to the lattice parameter), and the formation reaction most probably occurs apart from the parent cage. Formation of HKrCl in a Kr matrix and formation of HXeCCH and HXeBr in a Xe matrix have been shown to be mainly global processes,^{31,183} although some contribution from local mobility can also be noticed.³⁰ In Article I the formation of HArF was proposed to be a local process, and the data supporting this observation is described in the following section.

The efficiency of local formation is controlled by the local formation barrier characteristic of a molecule in vacuum, or a matrix-induced barrier. The avoided crossing (see Fig. 13) between the ionic and neutral potential energy surfaces causes the intrinsic barrier, which enables the HArF formation from the neutral H + Ar + F fragments. The intrinsic formation barrier has been calculated to be 0.18 eV by Runeberg *et al.*²¹ and 0.44 eV by Li *et al.*²³ Bihary *et al.* reported that the H + Ar + F reaction barrier decreases by ~ 0.2 eV in solid argon compared to vacuum, and they estimated a barrier of ~0.3 eV for the H + Ar + F reaction in argon matrix.²² It should be noted, that reaction barriers in matrices are very complicated to model due to the many particles and their interactions involved in the process. Thus it is easy to imagine that

the local host environment can have consequential effects on the precursor photodissociation and the HArF formation.

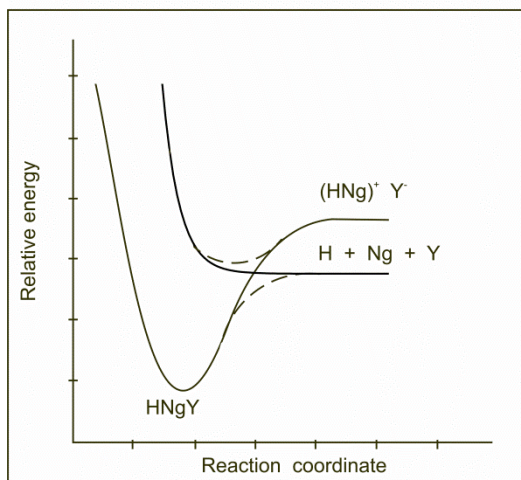


Figure 13. *The avoided crossing between neutral and ionic potential energy surfaces.*

For local formation process, no dependence on the initial precursor concentration to the formation rate should occur. The concentration dependence of the HArF formation is presented in the insert of Fig. 12. The amount of precursor HF was varied, and it was observed that lower HF precursor concentrations (1:1400 to 1:6000) did not affect the formation kinetics. This strongly suggests the local formation scheme. In an earlier study of HKrCl molecule, the formation time changed by a factor of two between this concentration range. This behavior was connected to global formation mechanism.¹⁸³ In contrast to the concentration independence of local processes, global formation is relatively strongly dependent on the precursor concentration. In the global formation scheme, the reaction should generally slow down with lowering precursor concentrations, since more jumps of the hydrogen atoms are required to reach the reactive center. It was observed, that with high precursor concentrations (~1:700) the HArF formation process increased slightly (~30%). This is possible to explain by the matrix morphology. With higher HF-concentration, the matrix was likely to have more defects, and this can lower the formation barrier.

Another observation that supports the locality of the formation and thus the tunneling mechanism is the fact, that HArF is already formed in small

amounts upon initial photolysis. Precursor HF photolyzes locally and part of the dissociating H atoms stay close to the parent cage. Due to this proximity, they can be captured to the HArF energy minimum forming the intermediate. The following photons can decompose the intermediately formed HArF and provide excess energy to the H atoms sending them away from the parent cage. The other part of the dissociated H atoms can be stabilized immediately after the initial precursor photodissociation. It can be argued that the H atoms formed from the intermediate HArF dissociation will not participate in the low temperature formation of HArF due to the long distances from the parent cage. These H atoms could, nevertheless, participate in the annealing induced formation, as temperature will cause long-range mobility. This does not seem, however, to be an effective route based on the observation that the low temperature formation is almost complete even at the lowest measured temperatures (8 K), and further annealing does not increase the absorption significantly.

4.1.5 HArF@Ar_n Supermolecule

Another observed feature that supports the local formation mechanism is the HArF formation time dependence on the deposition temperature. Although the matrix preparation is always a compromise between the deposition rate and the temperature, in general higher deposition temperatures lead to more regular matrix structures. This produces deeper energy wells for atoms to stabilize after photolysis and creates higher energy barriers for further reactions. In earlier studies of HArF, the transformation temperature from the unstable form to the stable form was increased by increasing deposition temperature.¹⁸ Theoretical models connected the difference between the stable and unstable configurations with their substitutional numbers meaning that the thermal reorganization of the system involved a mobile vacancy. Accepting the vacancy in one model and losing a vacancy in the other.^{25,26} In one model, the stable HArF absorptions were assigned to a loose, double-substitutional site and unstable HArF to a compact, single-substitutional matrix site.²⁶ In another model the opposite assignments were made.²⁵ Experimentally, the mobile vacancies are discussed in detail.^{19,29} In this context, the HArF@Ar_n supermolecule was also introduced.¹⁹ In the supermolecule model, it was assumed that the loose HArF configuration has two forms, with and without formation of the Ar...HArF complex, appearing as the stable and unstable forms, respectively. These two configurations can be separated by a low-energy reaction barrier, and the transition from the higher-energy state to the lower-energy state takes place around ~30 K. When HArF was considered in argon surrounding (HArF@Ar_n) as a supermolecule, two of its isomers were discussed.¹⁹ The isomers considered

were two stable configurations of HArF in loose matrix site (double substitutional and T-shaped according to their nomenclature). These structures were predicted computationally.²⁶ In this scheme, the unstable HArF is formed when HF precursor in a single substitutional matrix site photodissociates into the H+F pair, one of the atoms occupying the SS site (probably F) and the second atom being interstitial. The observed preferable formation of the higher energy configuration upon photolysis and low-temperature annealing may indicate that the formation of the higher energy configuration (unstable HArF) involves smaller reorganization of the surrounding matrix thus having a smaller formation barrier. In the case of the stable HArF formation, extensive reorganization of the local matrix morphology was required when the H atom of the HArF molecule complexes with a surrounding Ar-atom and it was energetically demanding, meaning a higher dynamical barrier.

In the follow-up work by Bochenkova *et al.*, the decomposition of unstable HArF and the formation of stable HArF were ascribed to local mobility of vicinal vacancies.²⁹ They observed that stable HArF was formed in two stages, below 20 K and at about 25-27 K. The lower-temperature stage was explained by the decomposition of the unstable HArF configuration with a vacancy in the first solvation shell. In this case, the low conversion barrier is determined by the movement on the vacancy in the first solvation shell, which allows a fast transition to the stable configuration. The direct formation of stable HArF from the neutral atoms is also possible at this stage, but this has not been modeled. The higher-temperature stage was attributed to the decomposition of the unstable HArF configuration with a vacancy in the second solvation shell. In this process, the conversion barrier is determined by the transition of the vacancy from the second to the first solvation shell. The theoretical conversion rates were in a good agreement with the experimental kinetics measurements.

As observed in case of the HArF formation, the condensed phase noble-gas medium can enable stabilization of otherwise highly unstable species (including extremely short-lived transition state structures). In the model discussed above, the matrix environment stabilizes the unique unstable-to-stable transition, and it is clear that the interaction between the HArF molecule and the host medium play an important role. Later in this thesis the attention is shifted to more familiar and atmospherically relevant matrices at more familiar temperatures. It will be seen, that also in more atmospherically realistic temperatures the matrix environment will affect the condensed phase reactions and lead to unique chemical phenomena.

4.2 Heterogeneous chemistry of N₂O₄ on Model Ice and Silica Surfaces

In Article II the role of the reaction surface was demonstrated by means of computational study of the heterogeneous isomerization reaction of N₂O₄ molecule on two atmospherically relevant surfaces. Both of the studied surfaces, ice [(H₂O)₂₀] and silica (Si₈O₁₆H₁₂), possessed so called dangling surface hydrogens, and these were suggested to play an important role in the isomerization reaction mechanism. The further ionization was also investigated.

Complexation of the N₂O₄ with both of the studied surfaces resulted in decrease of the N-N bond length, which indicates strengthening of the bond. The (O)N-O(NO₂) bond of the asymmetric ONONO₂ on the other hand was increased upon complexation, likely suggesting the tendency of the active, asymmetric form to cleave into ions. Both of these observations were expected based on earlier studies.⁴¹⁻⁵⁰ Several combinations of computational methods were tested and compared to experimental values, and their performance further validated based on previous reports. For example, it has been reported for N₂O₄ molecule, that MP2 overestimates the bond lengths.¹⁸⁴ Thus expectedly, the dispersion corrected B3LYP structural parameters of the isolated species were closer to experimental values. This validated the choice of the B3LYP functional to our research purposes. MP2 also is known to overbind the N₂O₄ system,¹⁸⁴ and for this reason the dispersion corrected B3LYP values were proposed as the most reliable in describing the N₂O₄ systems complexed with the (H₂O)₂₀ surface. The effect of the dispersion correction can be seen also in Table 1, where the harmonic frequencies of the dangling -OH vibration and the distance between the dangling surface hydrogen and the nearest oxygen atom of the NO_x species are listed for the studied systems. The comparison of this distance between calculations performed with the same level of theory, varying only in including or excluding the dispersion correction, showed that the dispersion corrected calculations bind the NO_x species significantly stronger. Similar conclusion for the silica surface can be drawn from Table 2, where the interaction energies of the studied systems are listed.

Table 1. The harmonic frequencies of the dangling –OH vibration and the distance between the dangling surface hydrogen and the nearest oxygen atom of the NO_x species. DFT = with (B3LYP/def2-TZVP), DFT2 = with [B3LYP/6-311++G(d,p)], MP2 = with (MP2/aug-cc-pVDZ)

Studied system (method)	Dangling –OH frequency (distance to nearest O of the NO _x in Å)
N ₂ O ₄ ···(H ₂ O) ₂₀ (DFT)	3821 (2.364)
N ₂ O ₄ ···(H ₂ O) ₂₀ (MP2)	3800 (2.125)
ONONO ₂ ···(H ₂ O) ₂₀ (DFT)	3693 (2.810)
ONONO ₂ ···(H ₂ O) ₂₀ (MP2)	3725 (2.816)
TS···(H ₂ O) ₂₀ (DFT)	3718 (2.508)
NO ⁺ NO ₃ ⁻ ···(H ₂ O) ₂₀ (DFT2)	3710 (1.959)
NO ⁺ NO ₃ ⁻ ···(H ₂ O) ₂₀ (MP2)	3695 (1.954)
N ₂ O ₄ ···(SiO ₂) ₈ (DFT)*	3836 (2.345)
ONONO ₂ ···(SiO ₂) (DFT)	3585 (1.850)
ONONO ₂ ···(SiO ₂) ₈ (DFT)*	3636 (1.906)
TS···(SiO ₂) ₈ (DFT)	3651 (1.889)
TS···(SiO ₂) ₈ (DFT)*	3831 (2.247)
NO ⁺ NO ₃ ⁻ ···(SiO ₂) ₈ (DFT)	3630 (1.894)
NO ⁺ NO ₃ ⁻ ···(SiO ₂) ₈ (DFT)*	3693 (1.987)

* no dispersion correction

4.2.1 Isomerization

Figure 14 and Figure 15 show snapshots from the IRC calculations on the (H₂O)₂₀ and (Si₈O₁₆H₁₂) model surfaces, respectively. The correctness of the transition state was confirmed by the IRC in both cases, where the isomerization reaction was followed from the reactant (N₂O₄) to product (ONONO₂). These calculations clearly showed the role of the dangling –OH bonds, as highlighted in both Fig. 14 and Fig. 15. The changes in partial charges upon complexation, listed in Table 3, also support this mechanism.

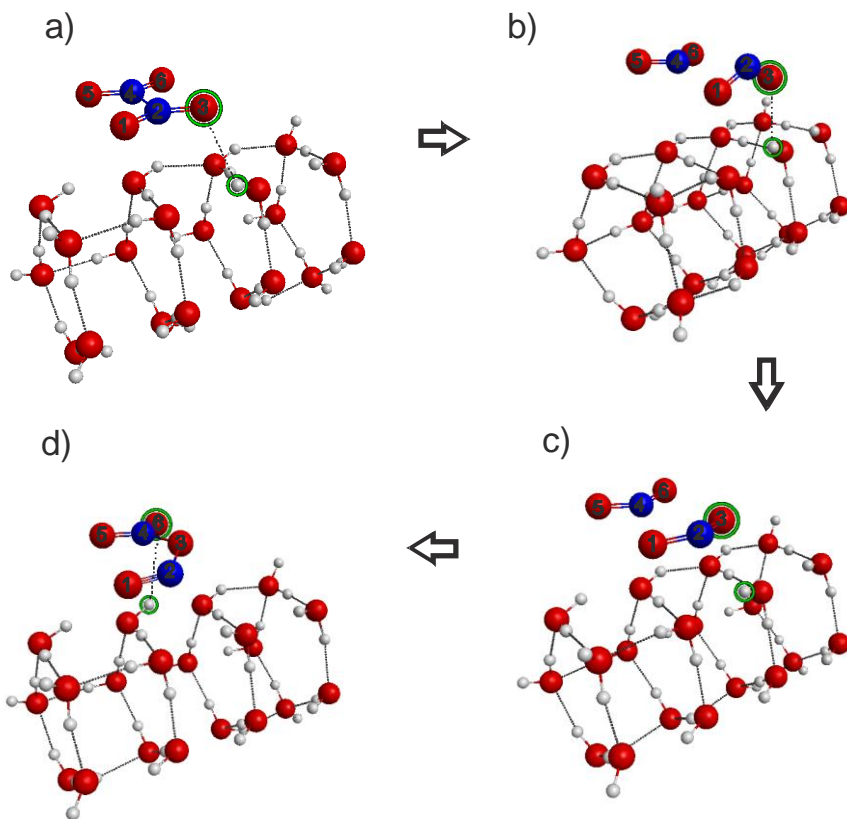


Figure 14. Snapshots of the IRC calculation of the isomerization reaction on the model ice surface including geometry optimized structures of a) symmetric N_2O_4 , b) transition state, c) arbitrary configuration along the reaction path d) asymmetric $ONONO_2$. The calculations were performed with B3LYP/DZVP level of theory. Red = O-atom, Blue = N-atom, White = H-atom.

The interaction energies of the studied systems are collected in Table 2. It should be noted, that the addition of the dispersion correction to the symmetric $N_2O_4 \cdots (SiO_2)_8$ calculation produced an additional imaginary frequency, but it is very likely that the dispersion corrected interaction energy would have suggested stronger binding based on the $ONONO_2$ results. As expected, the surface hydrogens on the silica surface interacted with the adsorbed NO_x species more strongly compared to water, as silica surface was more acidic reaction medium. The strong interaction is supported also by the significant intensity of the OH-vibration frequency of the surface hydrogen atoms bonding to the N_2O_4 and $ONONO_2$ molecules, 1270 cm^{-1} in $ONONO_2 \cdots (SiO_2)_8$.

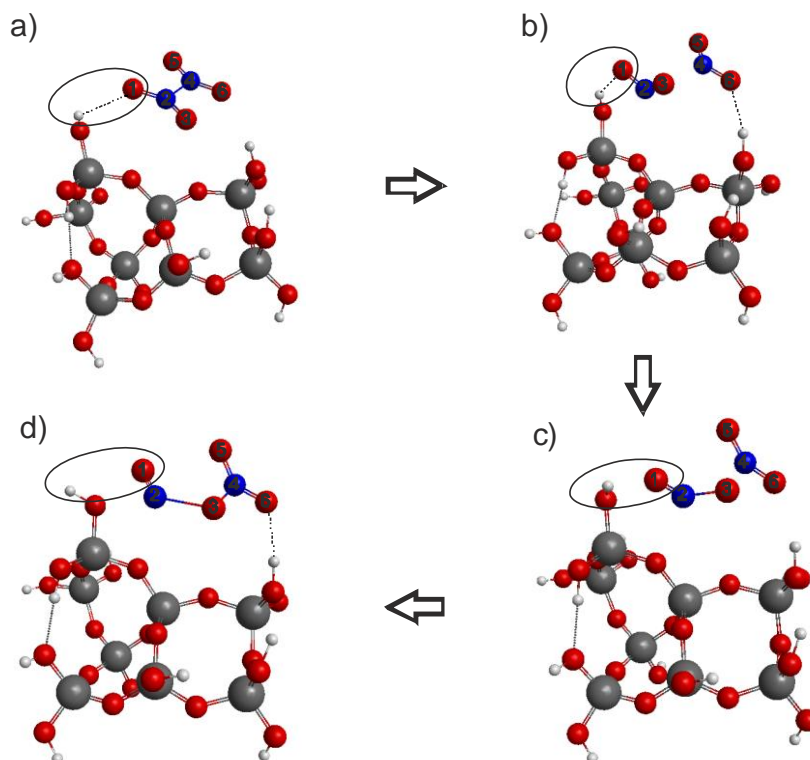


Figure 15. Snapshots of the IRC calculation of the isomerization reaction on the model silica surface. a) symmetric N_2O_4 , b) transition state (TS), c) arbitrary configuration along the reaction path d) asymmetric $ONONO_2$. The level of theory is B3LYP/DZVP. Red = O-atom, Blue = N-atom, Grey = Si-atom. White = H-atom.

Table 2. Interaction energies (E_{int}) of the studied systems. All energies are in kcal/mol. DFT=with (B3LYP/def2-TZVP), DFT2=with [B3LYP/6-311++G(d,p)], MP2=with (MP2/aug-cc-pVDZ), MP2,2=with [MP2/6-311++G(d,p)].

System/Method	DFT	DFT*	DFT2	DFT2*	MP2	MP2,2
$N_2O_4 \cdots (H_2O)_{20}$	-5.91	-	-6.93	-	-10.66	-9.78
$ONONO_2 \cdots (H_2O)_{20}$	-5.22	-	-7.25	-	-11.26	-11.24
$NO^+NO_3^- \cdots (H_2O)_{20}$	-	-	-7.51	-	-10.22	-
TS $\cdots (H_2O)_{20}$	-4.24	-	-	-	-	-
$N_2O_4 \cdots (SiO_2)_8$	-	-2.40	-	-4.34	-	-
$ONONO_2 \cdots (SiO_2)_8$	-11.54	-6.57	-	-8.87	-	-
$NO^+NO_3^- \cdots (SiO_2)_8$	-16.09	-6.31	-	-7.92	-	-
TS $\cdots (SiO_2)_8$	-8.49	-1.9	-	-	-	-

* no dispersion correction

The activation energy of the isomerization reaction of the isolated species was calculated to be 37 kcal/mol and 36 kcal/mol (B3LYP/def2-TZVP and B3LYP/6-311++G(d,p) levels, respectively). For isomerization on the ice and silica surfaces, the activation energies were 39 kcal/mol and 38 kcal/mol, respectively (B3LYP/def2-TZVP, DFT-D2 dispersion correction). The complexation with the surfaces was expected to lower the activation energies, but this behavior was not observed in the calculations.

4.2.2 Ionization

Previous studies on the ionization of the asymmetric ONONO₂ had shown that in the presence of water, the ionization reaction takes place fast (several picoseconds for one water molecule, much faster with several water molecules).⁵³ This approach utilized small water clusters [(H₂O)_n, (n ≤ 8)] to describe the heterogeneous air-water interface. A so called critical size-effect,¹⁸⁵ where the reaction starts to accelerate was observed for n ≥ 3 water molecules. In Article II the ionization was approached simply by investigating and comparing the structural parameters, partial charges, harmonic frequencies, and interaction energies of the asymmetric ONONO₂ and the corresponding ion pair NO⁺NO₃⁻.

The structures of the ion pair on the ice and silica surfaces are presented in Fig. 16. Energetics are collected in Table 2. As a result of the ionization, the partial charge separation between the NO⁺ and NO₃⁻ ions is increased in both systems (by 0.12 and 0.08 in ice and silica, respectively). In the case of the (H₂O)₂₀, the separation is larger. Also at the ice surface, the interaction between the ion pair and the surface is stronger than in the complex of ONONO₂, suggesting that the ionic form is the preferred configuration.

Table 3. Partial charges of the oxygen and nitrogen atoms. Both isolated and complexed species are listed. The partial charges were calculated using Natural Population Analysis (NPA), level of theory was B3LYP/def2-TZVP.

System/Atom	O (1)	N (2)	O (3)	N (4)	O (6)	O (6)
N ₂ O ₄	-0.25	0.51	-0.25	0.51	-0.25	-0.25
TS	-0.22	0.47	-0.22	0.43	-0.22	-0.22
ONONO ₂	-0.09	0.47	-0.36	0.67	-0.36	-0.31
N ₂ O ₄ ⋯(H ₂ O) ₂₀	-0.29	0.53	-0.25	0.54	-0.29	-0.25
TS⋯(H ₂ O) ₂₀	-0.27	0.46	-0.24	0.46	-0.21	-0.20
ONONO ₂ ⋯(H ₂ O) ₂₀	-0.06	0.50	-0.34	0.68	-0.41	-0.33
N ₂ O ₄ ⋯(SiO ₂) ₈	-0.27	0.52	-0.25	0.52	-0.23	-0.29
TS⋯(SiO ₂) ₈	-0.24	0.50	-0.21	0.43	-0.21	-0.27
ONONO ₂ ⋯(SiO ₂) ₈	-0.02	0.53	-0.40	0.68	-0.38	-0.39

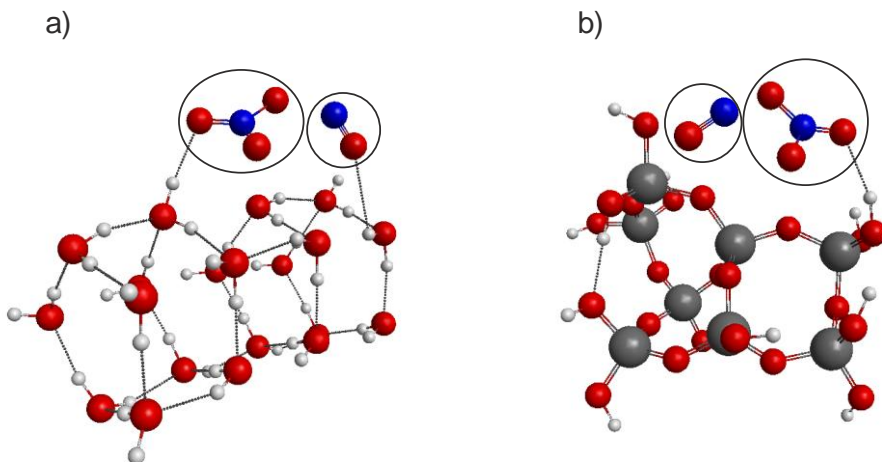


Figure 16. The ionpair complexes. a) $\text{NO}^+\text{NO}_3^-\cdots(\text{H}_2\text{O})_{20}$ and b) $\text{NO}^+\text{NO}_3^-\cdots(\text{SiO}_2)_8$. The calculations were performed with MP2/aug-cc-PVDZ for $\text{NO}^+\text{NO}_3^-\cdots(\text{H}_2\text{O})_{20}$ and B3LYP/def2-TZVP for $\text{NO}^+\text{NO}_3^-\cdots(\text{SiO}_2)_8$. Red = O-atom, Blue = N-atom, Grey = Si-atom, White = H-atom.

4.2.3 Atmospheric Implications

The main finding of this work was that the dangling $-\text{OH}$ on surfaces may indeed play a key role in converting symmetric N_2O_4 to the asymmetric form ONONO_2 , as was proposed in the past for ice.⁴⁶⁻⁴⁸ The solid phase environment can promote the $\text{N}_2\text{O}_4 \rightarrow \text{ONONO}_2$ isomerization, and the model surfaces used in this work were certainly more realistic than the previously considered polarizable continuum model and small cluster models.^{42,49,50,53} It was observed by comparison to these previous studies, that the solid surface as a medium for the isomerization reaction differs from reactions modeled in bulk water media and small clusters.^{42,49,50,53} This was presumably the first time when these atmospherically relevant solid phase reactions were studied computationally on real surfaces, such as ice and silica. The dangling $-\text{OH}$ mechanism may serve as a more general model for other surfaces as well. However, the activation energy calculated for this process, 36 - 39 kcal mol⁻¹, was relatively high, suggesting a small reaction rate for this reaction. Under atmospheric conditions, however, some water will always be present on the surface, either as adsorbed water on silica surfaces or as a quasi-liquid layer on ice surfaces. Since the role of water in assisting this isomerization has been predicted,⁴² it seems likely that the combination of the dangling $-\text{OH}$ and the presence of water molecules could

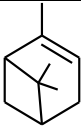
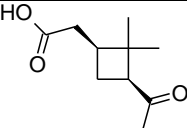
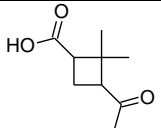
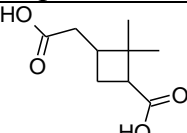
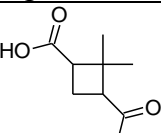
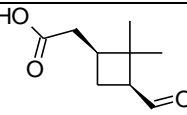
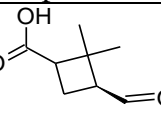
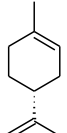
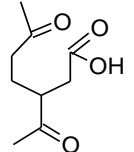
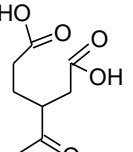
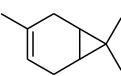
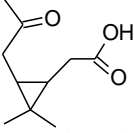
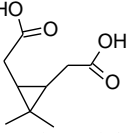
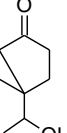
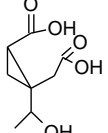
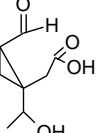
work cooperatively. This may have been the case for the experimentally observed isomerization on ice.⁴⁶⁻⁴⁸ It is also possible that in the previous work where the bulk water medium was described by the means of polarizable continuum model,⁵⁰ the water worked as dielectric medium thus decreasing the reported barrier. A non-direct photochemical effect, where light is converted to local heat on the surface also could provide means for lowering the high barrier. This behavior does not apply to the dark reaction, but evidence exists for photochemical production of HONO from reactions of oxides of nitrogen.¹⁸⁶⁻¹⁹⁰ As a conclusion, while the calculated barrier is high, it may be possible to mediate the differences by one of these mechanisms.

4.3 Aqueous Photochemistry of *cis*-Pinonic Acid and α -pinene SOA

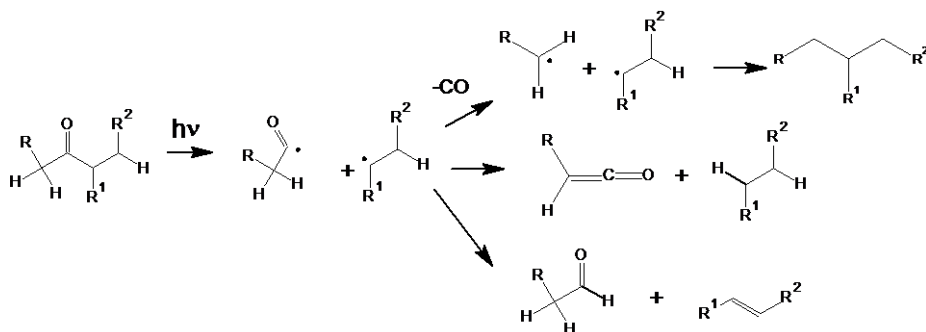
α -pinene is one of the most common biogenic monoterpenes. It is especially abundant in coniferous forests. Ozonolysis of α -pinene produces *cis*-pinonic acid (PA) as one of the first-generation products and further oxidation of the first-generation products then leads to highly-oxidized compounds that condense to SOA. Other monoterpenes also produce related multifunctional products in their photooxidation reactions, with some examples listed in Table 4.

In Article III, PA was chosen as a representative α -pinene SOA constituent, and the rate, quantum yield, and mechanism of its aqueous photolysis were investigated using experimental and computational methods. The results summarized in the following sections provide useful insights into the role of biogenic carbonyls in photochemistry of aqueous SOA.

Table 4. Common monoterpenes and their oxidation products

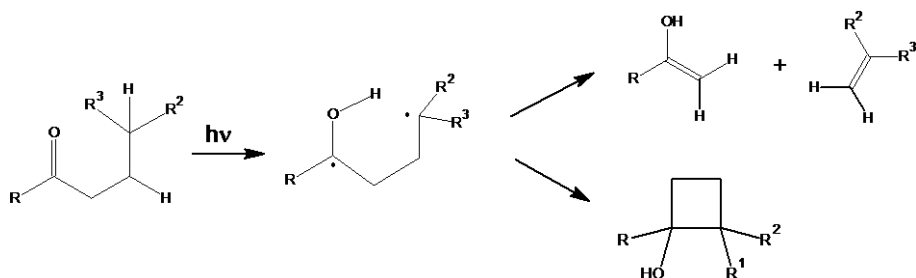
Monoterpene	Oxidation product	
 α-pinene	 cis-pinonic acid	 norpinonic acid
	 pinic acid	 norpinic acid
	 pinalic acid	 norpinalic acid
 d-limonene	 keto-limononic acid	 keto-limonic acid
 Δ ³ -carene	 caronic acid	 caric acid
 sabinene	 sabinic acid	 sabinalic acid

The photolysis of PA is taking place via the well known Norrish type-I and Norrish type-II photochemical mechanisms,¹⁹¹ which now will be briefly discussed. Scheme 1 shows the Norrish type-I (or α cleavage) reaction where the photoexcited ketone dissociates between the carbonyl carbon and the α -carbon related to the carbonyl group.¹⁹² In the gas phase the diradical can be vibrationally excited and additional processes take place (such as the loss of $-\text{CO}$ shown in Scheme 1).¹⁹³



Scheme 1. Norrish type-I reaction. Initially two radicals are formed which can further react via three different channels.

In Scheme 2, the Norrish type-II (or β cleavage) is presented. The Norrish type-II reaction proceeds by hydrogen atom abstraction, preferably on the γ -carbon with respect to the carbonyl group.¹⁹² This can also lead to ring opening, as in case of the PA photolysis. The diradical can then react to form cyclobutanol or the alkene and enol products shown in Scheme 5. The diradical can also transfer the hydrogen back to the γ carbon which can lead to racemization of the chiral center.⁷



Scheme 2. Norrish type-II reaction. The initial step is a hydrogen abstraction which can produce cyclobutanol, enol, and alkene products.

4.3.1 Products and Mechanism of the Aqueous PA Photolysis

The first goal of Article III was to investigate the mechanism of the aqueous *cis*-pinonic acid photolysis. This was achieved by separating the photolysis products, and analyzing them using liquid chromatography, mass spectrometric methods, and nuclear magnetic resonance spectroscopy, as well as computational methods.

The GC-CIMS chromatograms of PAMe after 0, 30, and 60 minutes photolysis, and PA ethyl ester after 60 min photolysis are shown in Fig. 17. After 60 minutes of PAMe photolysis, one major product peak and two minor product peaks were visible. Mass spectra corresponding to these peaks are shown in Fig. 18 and all the observed products are listed in Table 5. In the case of the *cis*-pinonic acid ethyl ester photolysis it was observed that the parent peak and the two minor product peaks were shifted as was expected based on the different esterification alcohol, but the major photolysis product peak was unaffected. This led to a conclusion that the major product was not affected by the choice of the alcohol during the esterification process and that peak was assigned to a structural isomer of *cis*-pinonic acid, 3-isopropenyl-6-oxoheptanoic acid, also known as limononic acid (C₁₀H₁₄O₂). This isomer is formed upon PA photolysis via opening of the four membered cyclobutane ring, and then goes through an intramolecular esterification in its enol form when exposed to the acidic esterification conditions producing the C₁₀H₁₄O₂ molecule observed in the GC-CIMS experiments (see Scheme 3 and Fig. 18). It is likely that this cyclic enol-lactone can be formed from the isomer but not from PA itself, because the more constrained ring structure of PA hinders that pathway. After 2 hours of photolysis, two additional smaller peaks appeared in the chromatogram also corresponding to the unesterified formula of C₁₀H₁₄O₂. These peaks were assigned to additional structural isomers of the major product (PA isomer), and this was supported by the Norrish type-II mechanism that can produce three different PA isomers, of which two are less abundant due to steric constraints. The observation, that *cis*-pinonic acid photolyzes producing a single major product was supported also by HPLC, NMR, LC-ESI-MS, and UV-Vis experiments, as well as computational results.

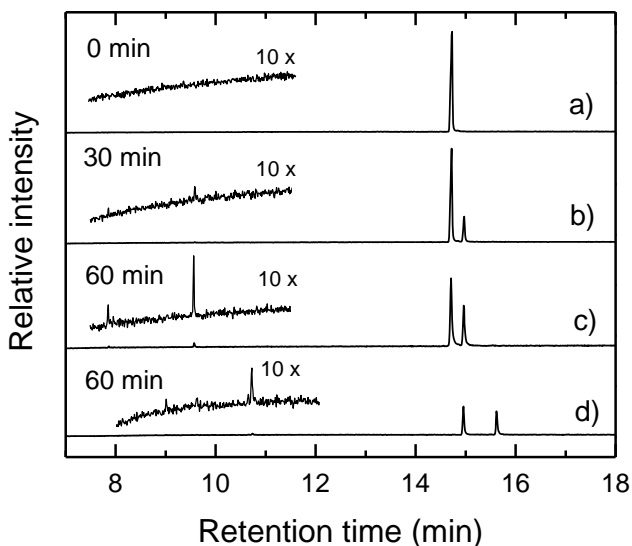


Figure 17. GC-CIMS total-ion-current chromatograms: (a-c) PA after 0, 30, and 60 minute aqueous photolysis followed by esterification of the photolysis products with methanol; (d) PA after 60 minute aqueous photolysis followed by esterification of the photolysis products with ethanol. The inserts show magnified portions of the chromatogram.

As carboxylic acids ionize easily, it was not a surprise that the (-) mode of the LC-ESI-MS experiments provided more easily interpretable results. Fig. 19 shows the chromatograms of PA and PA after 30 min of photolysis. The impurities in trace a) should be discussed briefly. The commercial PA used in this work originally contained some impurities. One of these is pinic acid (MW186). It is not surprising that pinic acid gives such a strong signal in the (-) mode ESI, as it has a high ionization efficiency (being a dicarboxylic acid). Pinic acid should also not interfere with the photolysis, as it does not have carbonyl functional groups. The carboxylic acid group is not expected to participate in photolysis, a statement that will be revisited later and which was discussed in detail in Article III.

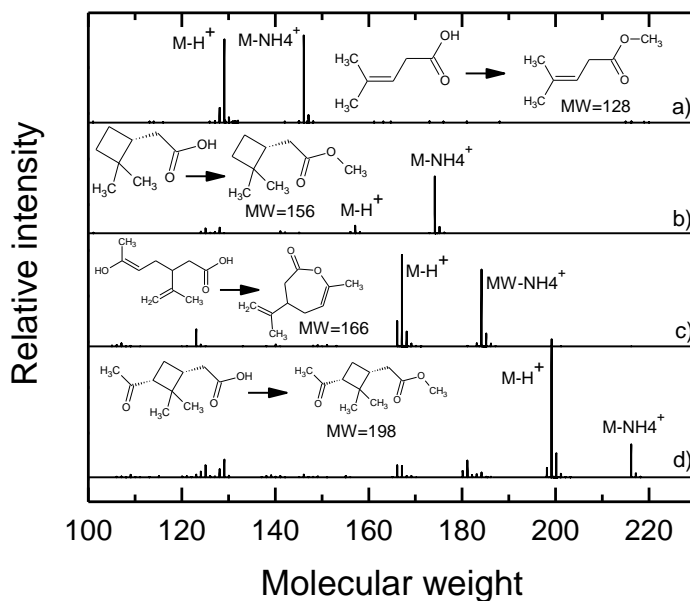
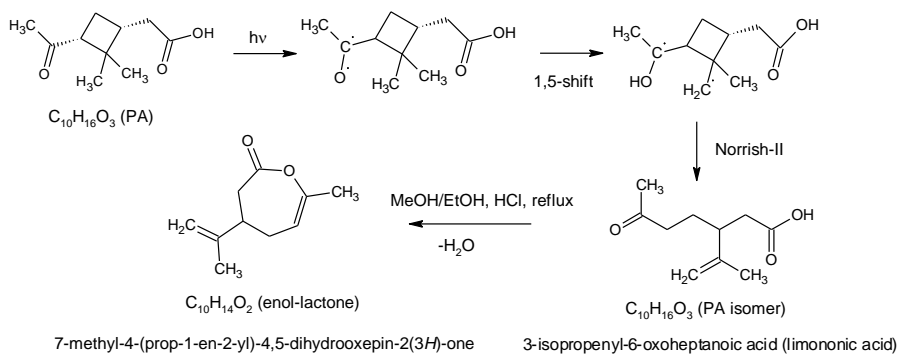


Figure 18. Mass spectra corresponding to the peaks observed in the GC-CIMS experiments. Unesterified formulas: a) $C_6H_{10}O_2$ (114), b) $C_8H_{14}O_2$ (142), c) $C_{10}H_{16}O_3$ (184, PA-isomer), and d) $C_{10}H_{16}O_3$ (184, PA).



Scheme 3. The major observed photolysis pathway for PA, resulting in a Norrish type-II isomerization into 3-isopropenyl-6-oxoheptanoic acid (PA isomer, also called limonic acid). The intramolecular esterification of the enol form of the PA isomer produces the enol-lactone detected by the GC-CIMS method.

The (+) ion mode spectra were harder to interpret, as it suffered from dimer formation and solvent interference. Some of the peaks were identified also in the (-) mode, but with lesser certainty. In general, the mass spectrum of individual species was fragmented and ionized, and as opposed to the (-) mode spectrum where usually only one mass peak was present, in the (+) mode spectra one mass was scattered to several peaks.

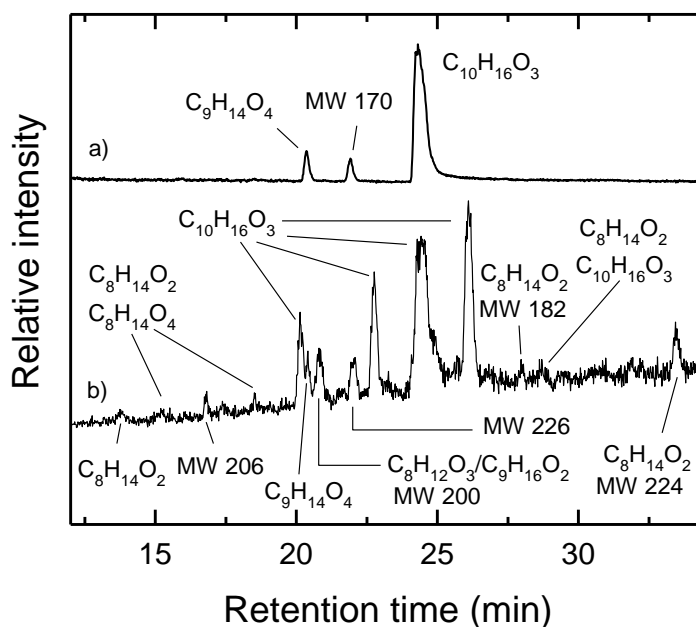
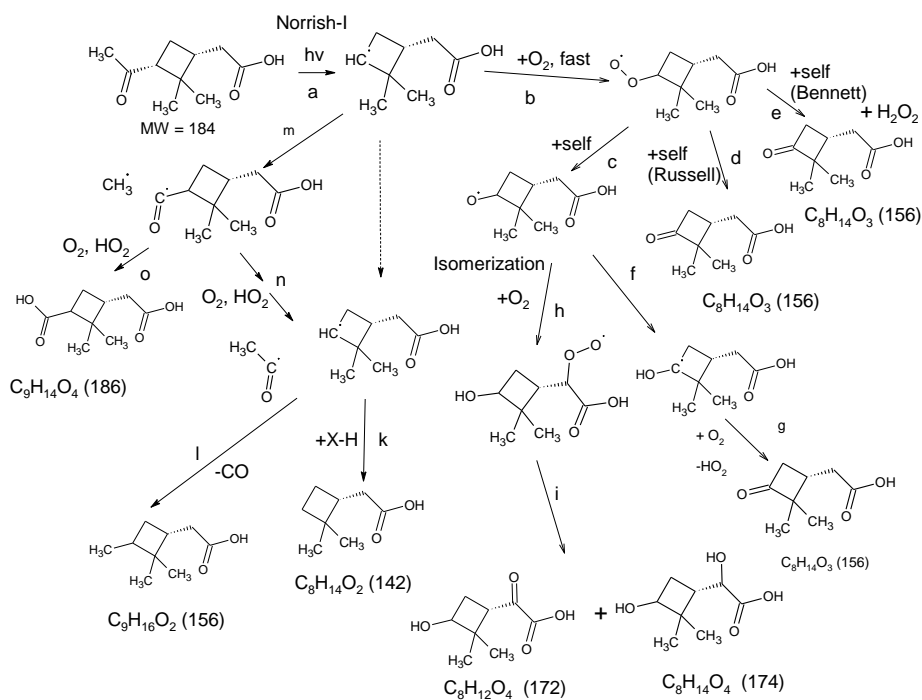


Figure 19. LC-ESI-MS negative ion mode total-ion-current chromatograms: a) PA solution before photolysis; b) PA solution after 30 minute photolysis. Chromatographic peaks are labeled by the molecular formula(s) and/or mass(es) of the neutral compounds corresponding to the major observed ions.

The interpretation of the (-) mode LC-ESI-MS data was assisted by mechanisms suggested for structurally similar species; the data were in good agreement with previous studies of photolysis of cyclobutylmethylketone (CMK) and aliphatic ketones.^{90,194-200} It should be noted that two well-known keto acids, namely pyruvic and glyoxilic acids, are known to photolyze by different mechanisms, but in contrast to PA, the carbonyl and carboxyl functional groups are in close proximity in pyruvic and glyoxilic acids.²⁰¹ In the case of PA the two functional groups are significantly separated by a fairly rigid hydrocarbon chain. The cyclobutyl ring, on the other hand, is directly attached to the carbonyl group, as it is in CMK, and therefore has

significant effect on its photophysical properties. The Norrish type-I and type-II reactions described above were able to explain most of the observations. The suggested mechanisms are shown in Scheme 4 and 5. As Norrish type-II reactions generally dominate in case of larger carbonyls, it was expectedly the dominating pathway in the aqueous *cis*-pinonic acid photolysis. The Norrish type-I reactions also occurred, as the LC-ESI-MS data suggest, but were clearly not as dominating. All the observed species are listed in Table 5 for clarity.

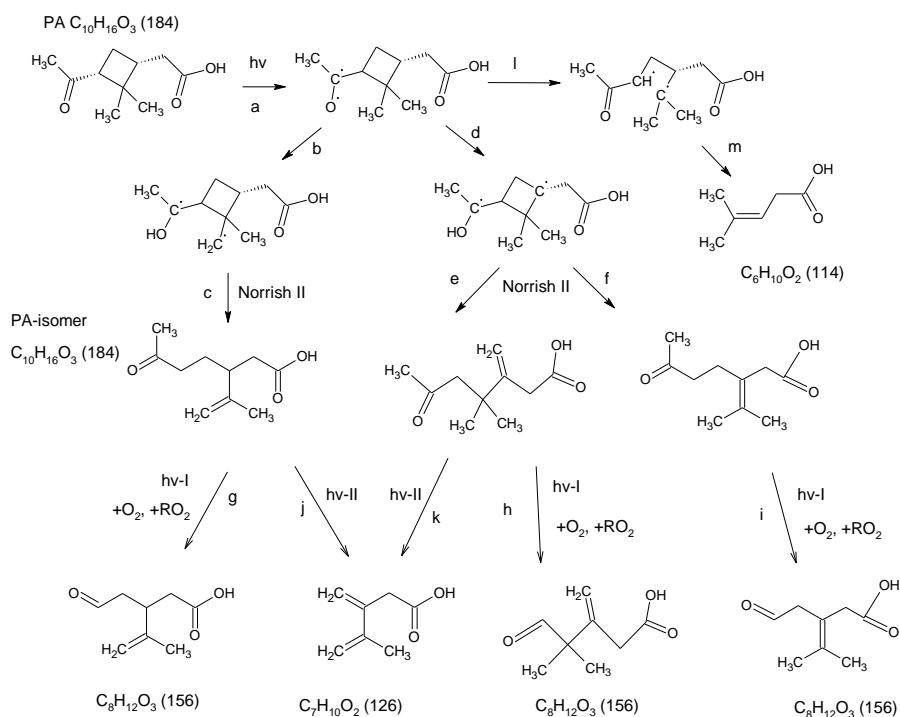
The Norrish type-I reactions can proceed via three different channels. In the peroxy radical forming Norrish type-I reaction, PA dissociates via $\text{CH}_3\text{-C}(\text{O})\bullet$ abstraction forming (in the presence of dissolved oxygen) an $\text{R-O-O}\bullet$ radical (reactions a and b in Scheme 4; R represents the residual part of the molecule after the splitting). The equilibrium concentration of dissolved oxygen in water is ~ 0.2 mM, which is smaller than that of PA (2-18mM), but the diffusion-limited rate constant for the $\text{R}\bullet$ and O_2 recombination is larger than the expected rate constant for abstraction of a hydrogen atom from PA by $\text{R}\bullet$. The long-lived peroxy radicals can be removed through self reactions (Bennet, Russel)¹⁹⁸ forming cyclobutanone based products with formula $\text{C}_8\text{H}_{12}\text{O}_3$ (MW156) (reactions c-f-g in Scheme 4), and self reactions that lead to $\text{C}_8\text{H}_{12}\text{O}_4$ (MW172) and $\text{C}_8\text{H}_{14}\text{O}_4$ (MW174) products via isomerization mechanisms (reactions c-h-i in Scheme 4). The second Norrish type-I path includes secondary reactions of $\text{R}\bullet$ with a suitable hydrogen donor, eventually forming a product with formula $\text{C}_8\text{H}_{14}\text{O}_2$ (MW142) (see Scheme 4, reaction k). This channel is expected to gain prominence in oxygen-depleted solutions. The third Norrish type-I path involves recombination of the primary radicals with a loss of CO, and produces a product with formula $\text{C}_9\text{H}_{16}\text{O}_2$ (MW156) (Scheme 4, reaction l). The $\text{C}_8\text{H}_{12}\text{O}_3$ (MW156) product can also be formed via the Norrish type-II reaction, but the $\text{C}_9\text{H}_{16}\text{O}_2$ (MW156) is unique to the Norrish type-I mechanism. Although the resolving power of the LC-ESI-MS instrument was not high enough to reliably distinguish between these two species, the data suggested the $\text{C}_9\text{H}_{16}\text{O}_2$. In the gas phase studies of PAMe (discussed later) both analogs of the MW156 product were observed [the methyl-esterified isomers ($\text{C}_9\text{H}_{14}\text{O}_3$ (171) and $\text{C}_{10}\text{H}_{18}\text{O}_2$ (171))]. Formation of CO is possible regardless of whether the photolysis initially splits the $\text{CH}_3\text{-C}(\text{O})$ or $\text{CH}_3\text{C}(\text{O})\text{-}$ bond. If the $\text{CH}_3\text{-C}(\text{O})\text{-}$ bond is split initially, reaction with O_2 can also lead to formation of pinic acid $\text{C}_9\text{H}_{14}\text{O}_4$ (MW186) (Scheme 4, reactions m-o).



Scheme 4. Expected products from the Norrish type-I splitting of PA and secondary chemistry in solution exposed to air.

In the Norrish type-II reaction, the 1,5-hydrogen shift can lead to the cyclobutane ring opening, producing a number of PA isomers. One of these isomers with the most probable 1,5- shift is suggested to be the major photolysis product of the aqueous photolysis of PA (Scheme 5, reaction a-b-c). Two more isomers are formed via less probable 1,5 shifts due to steric constraints (Scheme 5, reactions a-d-e and a-d-f). In the LC-ESI-MS experiments, all three isomers were observed in the photolyzed samples (Fig. 19). The GC-CIMS data further showed that only one of them clearly dominates (Fig. 17). All of the isomers can go through additional Norrish type-II reactions where photochemical intramolecular proton transfer results in a 1,4-biradical photoproduct that further produces smaller products, such as C₈H₁₂O₃ (MW156) (Scheme 5, reactions g, h, and i). A non-Norrish radical rearrangement that leads to cyclobutane ring opening and further splitting of the molecule has been reported previously.¹⁹⁶ This splitting can lead to formation of C₆H₁₀O₂ (MW114) (Scheme 5, reactions l-m), which is observed in our experiments as a minor product. The C₇H₁₀O₂ (MW126) (Scheme 5,

reactions j and k) was not observed in the aqueous phase studies, but was present in the gas phase photolysis of PAMe (discussed later). As will be seen later, calculations support the formation of the PA isomer (limononic acid) as the main photolysis product.



Scheme 5. Expected products from the Norrish type-II splitting and/or ring opening of PA and secondary chemistry in solution exposed to air.

Table 6. Molecular formulae and nominal masses of identified products of aqueous photolysis of PA (excluding the impurities). For consistency, the formulae from the GC-CIMS measurements correspond to the non-esterified photolysis products. The mechanism column indicates whether the product is formed by Norrish type-I (Scheme 4), Norrish type-II (Scheme 5), or direct ring opening (Scheme 5) pathways. The major detected product is C₁₀H₁₆O₃, a Norrish type-II isomer of PA shown in Schemes 3 and 4.

Molecular Formula (nominal mass, Da)	Method Detected	Mechanism
C ₆ H ₁₀ O ₂ (114)	GC-CIMS, LC-ESI-MS	Ring-opening
C ₈ H ₁₄ O ₂ (142)	GC-CIMS, LC-ESI-MS	Norrish-I
C ₈ H ₁₂ O ₃ (156)	LC-ESI-MS	Norrish-I, Norrish-II
C ₉ H ₁₆ O ₂ (156)	LC-ESI-MS	Norrish-I
C ₈ H ₁₂ O ₄ (172)	LC-ESI-MS	Norrish-I
C ₈ H ₁₄ O ₄ (174)	LC-ESI-MS	Norrish-I
C ₁₀ H ₁₆ O ₃ (184)	GC-CIMS, LC-ESI-MS	Norrish-II, major product

Nuclear magnetic resonance spectroscopy was then used to further confirm the identification of the main photolysis product by initially separating it using HPLC and subsequently recording both C13 and H1 spectra of the separated fraction. NMR, although being less sensitive than the previously mentioned mass spectrometric techniques, provides important structural information needed to reliably identify the product. The NMR spectra of PA were in good agreement with previous measurements,²⁰² and the separated isomer was identified as 3-isopropenyl-6-oxoheptanoic acid (limonic acid). As no previous literature data of the isomer existed, the results were compared to predicted C13 and H1 spectra from Ref. 203 and to validate these predictions, same was done to PA. The C13 and H1 spectra were also measured from an experiment where PA was photolyzed 60 minutes directly in deuterated chloroform instead of water. This resulted in a clear spectrum with exceptionally good S/N ratio, where both the PA and the isomer peaks were visible. This spectrum is presented in Fig.20.

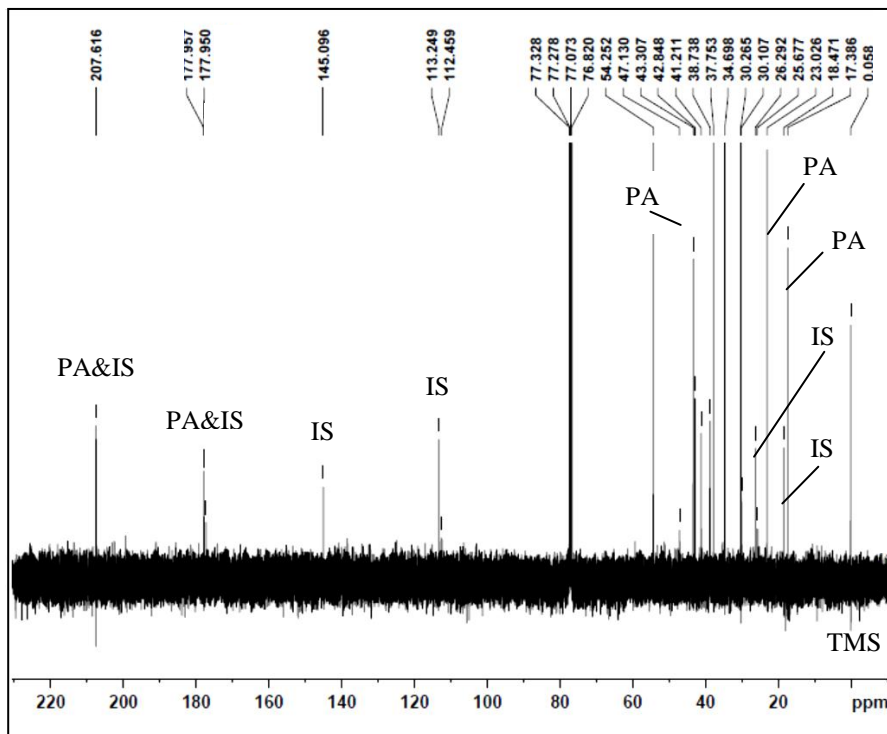


Figure 20. The C^{13} NMR spectrum of PA after being photolyzed in $CDCl_3$ for 60 min, with peaks due to PA and its isomers (IS) clearly observable. Some of the peaks are notated in the figure.

The other fractions separated by HPLC were also attempted to measure with NMR. In addition to D_2O , $CDCl_3$, and CD_3CN , also C_4D_8O (THF-d8) was used as a solvent. However, due to the small amounts of separated product species, the sensitivity of the NMR instrument was not sufficient to produce reliably interpretable data.

4.3.2 Absorption Cross Sections and Quantum Yield of the Photolysis

The second goal of Article III was to measure absorption cross sections of PA and determine the quantum yield of the photolysis. This information is necessary to quantitatively determine the lifetime of PA in an aqueous environment. This was achieved by UV-Vis measurements of the aqueous PA photolysis and the photolysis of a chemical actinometer, azoxybenzene. The

results were interpreted with three different kinetics models that addressed the difficulty of the data interpretation arising from issues including the possible product absorption at 280 nm, the increased extinction coefficient due to the conjugation effects caused by the cyclobutyl ring, and differences/similarities of the PA and its isomer.

First, the absorption cross section of aqueous PA with respect to other carbonyls should be discussed. The aqueous PA absorption cross section is shown in Fig. 21 in comparison with cross sections of gas phase acetone,³ aqueous acetone,²⁰⁴ and CMK in isooctane.¹⁹⁶ The middle part of the 280 nm band of the aqueous PA cross section resulting from the $\pi^* \leftarrow n$ transition is notably different from the other carbonyls for the following reasons. The increase in absorption of PA relative to acetone is partly due to second order conjugation effects arising from the cyclobutyl ring next to the PA's carbonyl group.²⁰⁵ Additionally, the difference between aqueous PA and CMK in isooctane is explained by increasing solvent polarity which increases the absorption cross section and shifts the center absorbance to the blue.²⁰⁶ The comparison of gas phase PA (or PAME) was not included, since those values were not measured quantitatively during the work.

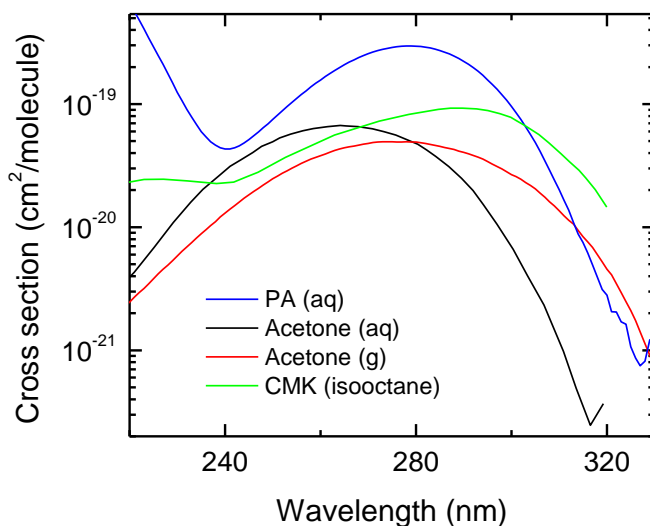


Figure 21. Absorption cross sections of aqueous PA (this work, used for calculating the quantum yield of photolysis in aqueous experiments), aqueous acetone,²⁰⁴ gas phase acetone (used for calculating the quantum yield of photolysis in gas-phase experiments),³ and cyclobutyl methyl ketone (CMK) in isooctane.¹⁹⁶

In addition to the molecular extinction coefficients of PA (obtained from the absorption cross section measurements), determination of the photolysis quantum yield required quantification of the UV-light used in the photolysis experiments. This was done using chemical actinometry. An actinometer suitable for this purpose was azoxybenzene, as its quantum yield is relatively independent of initial concentration and temperature over the wavelength range of interest. Azoxybenzene photoisomerizes upon photolysis with a known quantum yield ($\phi_{act} = 0.021 \pm 0.0019$),¹⁴⁷ the UV-Vis spectra of the photolysis is presented in Fig. 22. The photolysis of aqueous PA was carried out under similar experimental conditions, and the decrease of the $\pi^* \leftarrow n$ transition at 280 nm was followed as a function of time. The spectra of the PA photolysis is shown in Fig. 23, the insert shows the decay kinetics of the 280 nm peak. It should be noted that the steady decay of 280 nm feature almost to completion after 3 hours of photolysis is an indication of stable final photolysis product(s). Also visible in the spectra is an isosbestic point around 260 nm, which is an indication of a single photolysis product, observation that was supported also by previously described results.

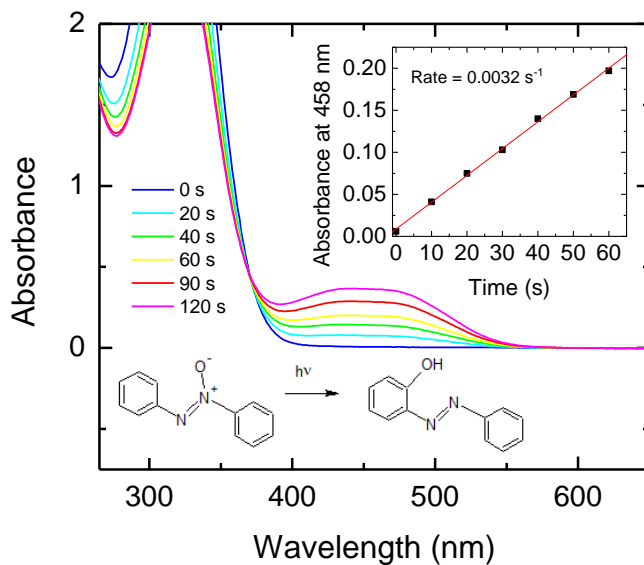


Figure 22. UV-Vis spectra of azoxybenzene actinometer photolysis, measured under the same conditions as photolysis of PA.

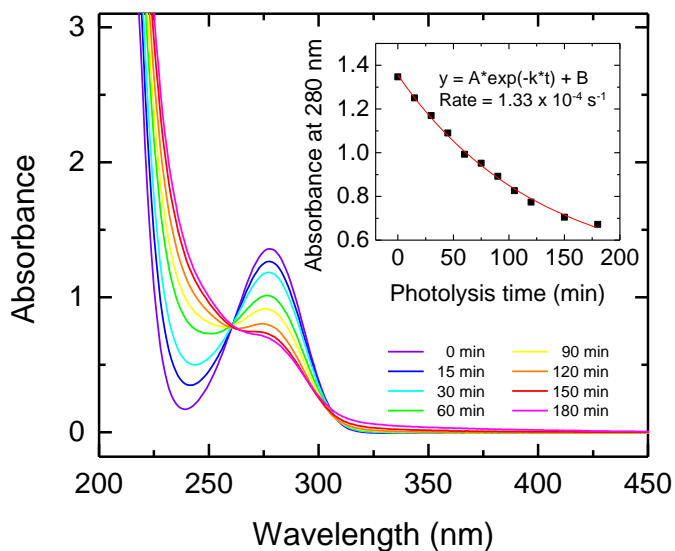


Figure 23. UV-Vis spectra taken during aqueous photolysis of 18 mM PA. The reaction rate and photolysis quantum yield are $1.33 \times 10^{-4} \text{ s}^{-1}$ and 0.30, respectively. In the insert is an exponential fit to the absorbance at 280 nm as a function of time using Model 1.

The kinetic behavior of the aqueous PA photolysis was approached by three different kinetics models, that all had slightly different assumptions. Model 1 assumed an ideal case, where photolysis of PA produced a single product that did not photolyze further:

$$A_{10}(t) = A_0 \left[\beta + (1 - \beta) \cdot e^{-k_{PA}t} \right] \quad (1)$$

A_0 is the initial absorbance and the meaning of parameter β is the ratio of the absorption of the product and PA ($\beta = \epsilon_P / \epsilon_{PA}$).

However, when looking back at the experimental results described earlier, the assumption of a single, non-photolyzable product is not valid. It was shown by the HPLC, LC-ESI-MS, and GC-CIMS results, that more than one product are produced, and those products are also predicted to be photolyzable based on their functional groups.

In Model 2, an assumption that the photolysis reaction follows a two-step mechanism, $PA \rightarrow \text{Isomer} \rightarrow \text{Product(s)}$, was made. It was also assumed that the rate constants for both $PA \rightarrow \text{Isomer}$ and $\text{Isomer} \rightarrow \text{Product(s)}$ were

similar, and that the extinction coefficients of PA and IS were roughly the same. The initial idea for building up the Model 2 arose from the similarities of the PA and IS absorptions seen in the HPLC-PDA spectra. With these assumptions taken into account, the behavior of the 280 nm band could be described with the following equation:

$$A_{10}(t) \approx A_0 \left[\beta + (1 - \beta)(1 + kt) \times e^{-k \cdot t} \right] \quad (2)$$

where A_0 , β , and k_{PA} are fitting parameters, and β has a similar meaning as in Model 1. Model 2 includes a linear pre-exponential factor in the equation, which suggests sigmoidial behavior of the kinetics data in the early photolysis times when PA isomerizes prior to further photolysis. This type of sigmoidial behavior was not observed thus Model 2 did not fit the observed data as well as Model 1. This led to a search for additional models.

Model 3 makes a more realistic assumption by taking into account the differences in the extinction coefficients of PA and the isomer. As was discussed in the beginning of this section, the cyclobutyl ring in PA increases the extinction coefficient due to hyperconjugation.²⁰⁵ The extinction coefficient and the rate constant of the isomer were decreased by a factor f ($\epsilon_{IS} = f \times \epsilon_{PA}$ and $k_{IS} = f \times k_{PA}$), which was determined from the difference in cross sections between aqueous PA and aqueous acetone. Justification for this choice was the structural difference of these carbonyls, namely that PA structure includes a cyclobutyl ring but acetone does not. These assumptions produced the following dependence (value of f was fixed at 0.16):

$$A_{10}(t) = A_0 \left[\beta + \frac{(1 - 2f) + f\beta}{1 - f} e^{-k_{PA} \cdot t} + \frac{f - \beta}{1 - f} e^{-f \cdot k_{PA} \cdot t} \right] \quad (3)$$

Model 3 was able to fit the experimental data better than Model 2, and the quantum yields from Models 1 and 3 are listed in Table 6 (a). The average values were 0.43 ± 0.09 and 0.65 ± 0.27 for Model 1 and 3, respectively. The differences in these values are an indication of the uncertainties of the experimental method. The UV-Vis records the changes in the total absorbance that includes PA and its photolysis products, which is not the realistic representation of the case. The HPLC, LC-ESI-MS, GC-CIMS, and NMR data clearly show, however, that the PA isomerizes and further photolyzes, and it should be safe to suggest a value of 0.5 ± 0.3 for the photolysis quantum yield based on the kinetic model calculations. In the

future, improving these experiments by purging with dry argon would prevent any secondary peroxy radical products from forming and interfering with the carbonyl band decay. Also, investigating the photolyzed solutions with high resolution mass spectrometry would reveal possible secondary product formation. The loss of PA can be also followed with NMR spectroscopy directly, as NMR can distinguish between structural isomers (unlike UV-Vis).

Table 7. Measurements of the photolysis quantum yield of aqueous PA (a) and gaseous PAMe (b). The data suggest insignificant suppression of photolysis by the aqueous solvent.

a)

Concentration (mM)	Quantum Yield (Model 1)	Quantum Yield (Model 3)
18	0.32±0.03	0.39±0.08
10	0.49±0.03	0.93±0.19
2.0	0.47±0.06	0.64±0.24
average	0.43±0.09	0.65±0.27

b)

Measurement	Quantum Yield
Gas phase 1	0.51±0.06
Gas phase 2	0.55±0.06

4.3.3 The Gas Phase Photolysis of PAMe

In order to provide comparison between the aqueous PA photolysis and the fate of PA in the gas phase, gas phase photolysis experiments using PAMe were carried out. PTR-ToF-MS was used to follow the photolysis reaction in real time by monitoring the decay of the parent and formation of product species. PAMe was used instead of PA, as the PTR-ToF-MS instrument does not detect carboxylic acids sufficiently well. For the photolysis quantum yield calculation, acetone was used as an actinometer to quantify the light source, and the wavelength dependency of acetone's quantum yield and absorption cross section was taken into account utilizing data from Ref. 3.

The decay of the PAMe and the acetone actinometer are shown in Fig. 24, the rates resulted in an averaged quantum yield of 0.53 ± 0.02 for the PAMe photolysis. This quantum yield, however, cannot include the analogous isomerization process (Norrish type-II) observed in the aqueous photochemistry experiments, as the isomer and the parent species are isobaric (i.e., have the same molecular weight). Thus, the actual overall quantum yield in this case is likely higher, and it could potentially be as high as 1. In the future it would be beneficial to carry out these experiments in an FTIR-chamber, and follow the build-up of the isomer's double bond, obtaining an overall quantum yield for the photolysis as well as the individual product yields. In addition to the quantum yield, information about the photolysis products was obtained, and these observations suggest that the photolysis mechanisms of aqueous PA and gas phase PAMe bear similarities. Figure 25 shows a time-series plot of the decay of PAMe and formation of products. The PAMe photolysis resulted in Norrish type-I products $C_9H_{14}O_3$ (170.084) and $C_{10}H_{18}O_2$ (170.131), which are analogues of the MW156 species observed in the aqueous PA photolysis (see Schemes 4 and 5). $C_8H_{12}O_2$ (140.084) and $C_9H_{16}O_4$ (188.105) also appeared upon photolysis of PAMe, and they correspond to MW126 and MW174 in the case of PA. MW126 was not observed in the PA photolysis experiments, but was expected based on the suggested mechanism in Scheme 5. MW174 was detected in the LC-ESI-MS experiments (Scheme 4).

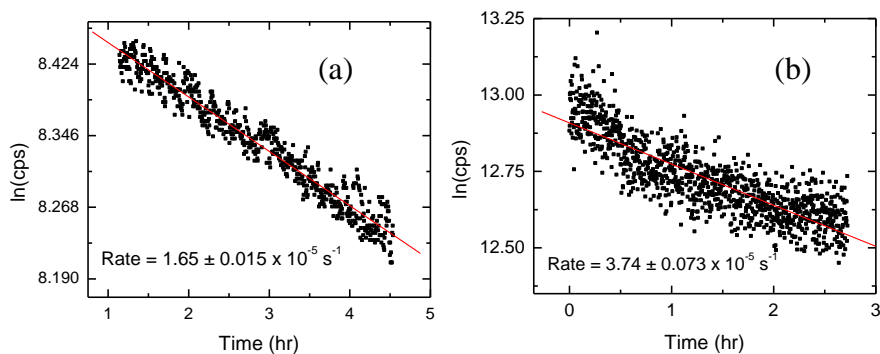


Figure 24. The decay of the PAMe signal (a) and decay of the acetone signal (b) recorded by the PTR-ToF-MS instrument under identical conditions

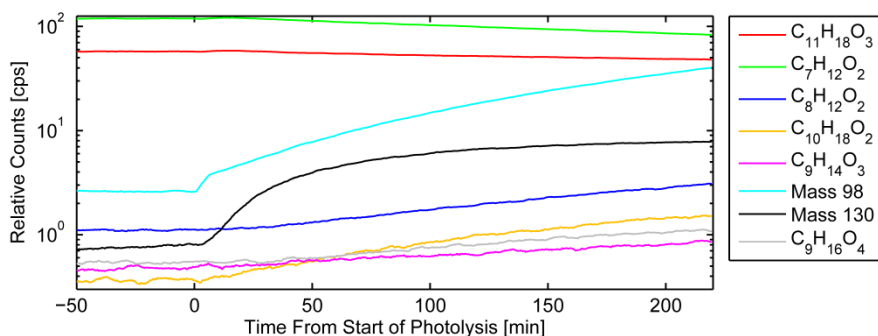


Figure 25. Relative counts as a function of photolysis time for specific products in the photolysis of PAMe. Counts are scaled by their estimated transmission, but are not corrected by the rate constants of H_3O^+ reaction (no published data available). $\text{C}_7\text{H}_{12}\text{O}_2$ signal is proportional to PAMe ($\text{C}_{11}\text{H}_{18}\text{O}_3$) signal and is most probably a fragment. Unidentified peaks appearing at m/z 129.986 and m/z 98.0742 must come from impurities, as their formation rates are faster than the disappearance of PAMe.

4.3.4 Computational results for the PA photochemistry

Fig. 26 presents the optimized MP2/cc-PVDZ structures of PA, PAMe \cdots H₂O complex, and PAMe \cdots (H₂O)₅ cluster. The simulations of photodissociation dynamics in both PA and PAMe included only the 1st singlet excited state, which is centered on the carbonyl group. Higher electronic states were not expected to play an active role in the photodissociation dynamics, an assumption that is supported by previous studies of similar systems.¹⁷⁴ The singlet-triplet gap was 0.2 eV with the ADC(2) method and 0.3 eV with the OM2/MRCI method. The intersystem crossing (ISC) transition was forced at the smallest singlet-triplet gap, and the MD simulations were initiated from that location.

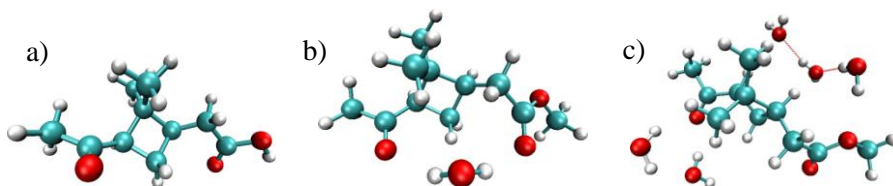


Figure 26. The equilibrium structure of a) PA, b) PAMe \cdots H₂O, and c) PAMe \cdots (H₂O)₅. The level of theory is MP2/cc-PVDZ.

With the MD simulation time on the triplet surface set to 100 ps, the fraction of the trajectories leading to a photochemical reaction was 69%. Table 8 shows all the observed events (both reactive and non-reactive) observed in the simulations with the number of trajectories. Selected snapshots corresponding to the different reaction pathways observed in the bare PA calculations are presented in Fig. 27. There were four different types of events occurring during the PA and PAMe \cdots (H₂O)_n (n = 1 or 5) simulations. 1) No reaction and/or water evaporation. This was the most common results in all of the simulations, even up to 100 ps. 2) The initial step in the Norrish type-II reaction is the H-atom transfer from the methyl group to the carbonyl group [Fig. 27 (a)]. This event occurred in some of the simulation trajectories. There was no preference in the timing of the H-transfer in the simulation time window (0-100 ps), but it is possible that longer simulation times could increase the probability of this reaction. Histograms demonstrating the photolysis distribution time of this event are presented in Fig. 28 a)-b). 3) The most commonly observed event was the Norrish type-I reaction, the loss of the CH₃C(O)• radical. This reaction pathway was distributed throughout the entire 100 ps simulation. The photolysis distribution times as histograms of this event are presented in Fig. 28 c)-d). 4) Large number of trajectories resulted in the cyclobutyl ring opening [Fig. 27 (b)]. This event had a clear time preference; it either occurred on an ultrafast timescale (< 20 fs) or did not occur at all. 5) The loss of •C(O)OH PA (decarboxylation) [Fig. 27 (c)] or the corresponding, methylated loss of •C(O)OCH₃ from PAMe, was observed in some of the simulation trajectories. This event was found to be ultrafast in all of the observed the cases (within 500 fs).

Table 8. Comparison of the events in PA, PA+H₂O, and PA+5H₂O systems

Events	PA 300 K	PA + H ₂ O 300 K	PA + 5 H ₂ O 200 K	PA + 5 H ₂ O 300 K
No reaction	31	68	52	39
Norrish-II (H transfer)	10	2	5	3
Norrish-I (CH ₃ -CO abstraction)	37	18	8	24
Ring opening	10	5	18	18
COOCH ₃ abstraction	12	6	17	16

The reported computational results supported the experimental findings fairly well. The decarboxylation pathway was the only event that was not observed in the experiments, but this can be probably explained by the incapability of the LC-ESI-MS instrument to detect decarboxylated species. It is likely that the loss of the $\bullet\text{C}(\text{O})\text{OH}$ group takes place, but was not detected in these experiments due to instrumentation limitations. In the GC-CIMS, the decarboxylated species should have been detected. It is possible, however, that they are not observed due to evaporative losses of these species (low MW products especially) either during the derivatization or as entering the GC-CIMS. Most importantly, also the small effect of water molecule(s) on the different photolysis pathways is in agreement with the experimental results, as no extensive suppression of the photolysis of PA in aqueous solution was observed.

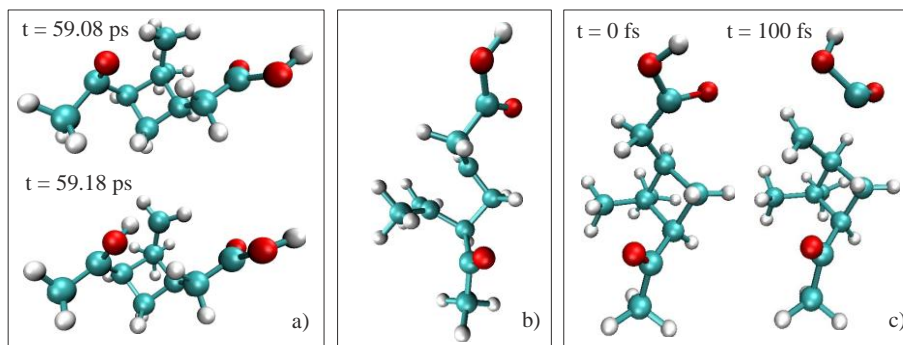


Figure 27. Representative snapshots of MD trajectories taken shortly after the following reactions took place: a) H-transfer to CO group; b) opening of the 4-membered ring; c) decarboxylation.

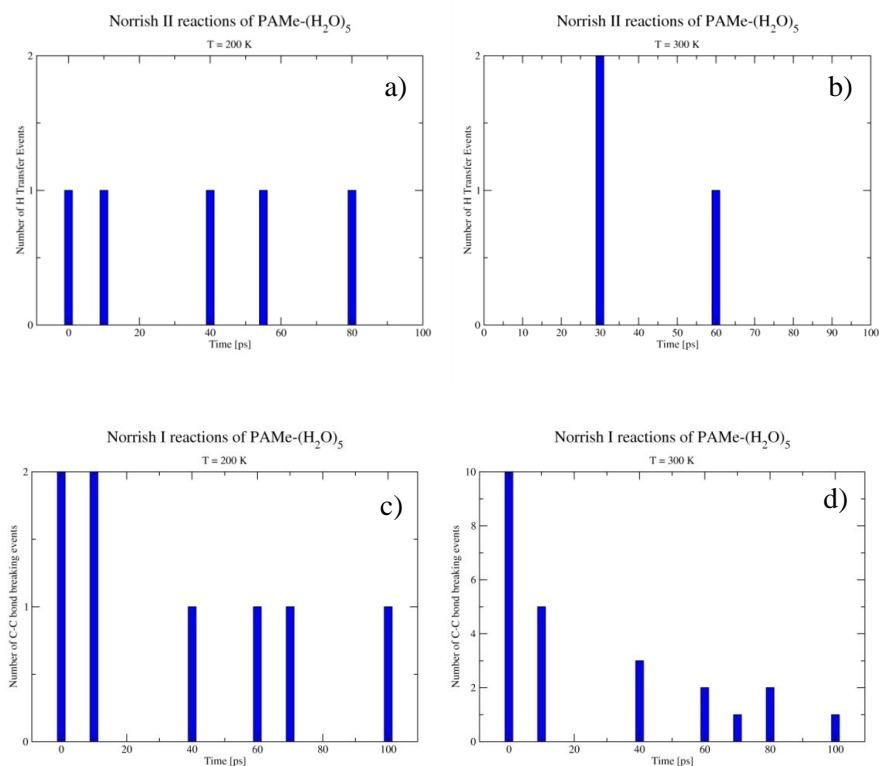


Figure 28. Histograms of the timescales of Norrish type-II and type-I reactions of PAMe \cdots (H₂O)₅. a) Norrish type-II at T = 200 K, b) Norrish type-II at T = 300 K, c) Norrish type-I at T = 200 K, d) Norrish type-I at T = 300 K. The time bin is 10 fs.

4.3.5 Atmospheric Implications

Atmospheric perspective to the results obtained in Article III was provided by two sets of calculations that compared the rate of removal of PA by direct aqueous photolysis in cloud water and in aerosol water. The calculations, described in the methods section of this thesis (Section 2.4), were performed for a range of solar zenith angles and compared with rates of other removal processes (gas-phase oxidation by OH, aqueous phase oxidation by OH, and gas-phase photolysis). As explained below, the calculations showed that the direct aqueous photolysis is not the most significant removal path for PA in the scenarios considered here, but it is likely that direct photolysis will

contribute to the removal of other, more soluble and/or less volatile biogenic oxidation products in aqueous and wet particle phases.

The PA removal selectivity via different channels as a function of the SZA is presented in Fig. 29. It can be seen that the aqueous OH-oxidation controls the fate of PA when found in an aqueous environment ($LWC = 0.5 \text{ g/m}^3$). Photolysis is the second most important pathway, responsible for removing about 2 % of the PA mass. In dry air masses ($LWC=0$) gaseous photolysis becomes more important but it also loses in efficiency to gas-phase OH-oxidation. At $SZA < 70^\circ$, the gas phase photolysis is responsible of removing ~40% of the PA in dry air, with the rest being removed by OH. It should be noted that the photolysis rates were more dependent on the SZA than the OH oxidation reaction rates, but a solar zenith angles below 60° , the selectivity is largely independent. Based on these calculations, it can be stated that the aqueous PA photolysis will be a significant removal pathway only in cloud and fog droplets where the OH concentrations happen to be unusually low.

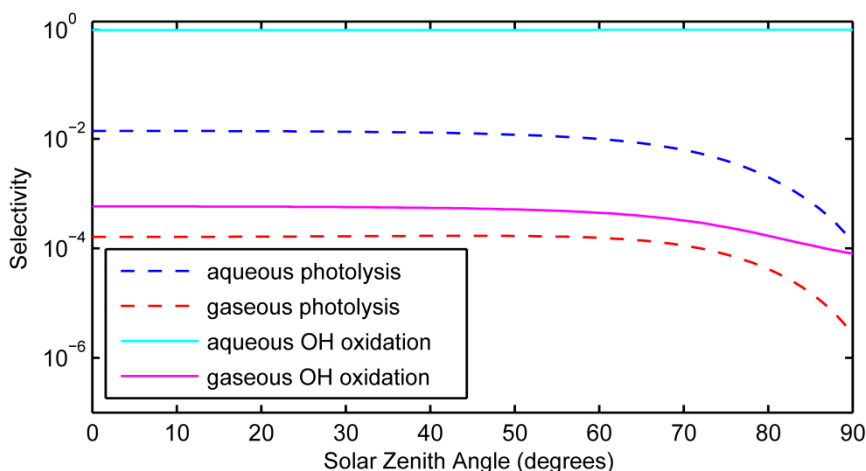


Figure 29. Calculated PA removal selectivity of key chemical processes likely to affect PA in the presence of cloud and fog droplets. The selectivity of aqueous photolysis, gaseous photolysis, aqueous oxidation by OH radical, and gaseous oxidation by OH radical are plotted as a function of solar zenith angle. $LWC = 0.5 \text{ g m}^{-3}$ and $T = 298 \text{ K}$.

The wet aerosol selectivity plot is presented in Fig. 30. Shown are the selectivity of the photolysis in the aqueous-aerosol phase, photolysis in the organic-aerosol phase, gaseous photolysis, and gaseous oxidation by OH as a function of SZA. At solar angles below 60° the gas phase OH oxidation and

organic-aerosol phase photolysis were the most significant pathways being responsible for $\sim 88\%$ of the PA removal. As the LWC in the aerosol was very low, the contribution of the aqueous photolysis was expectedly almost negligible.

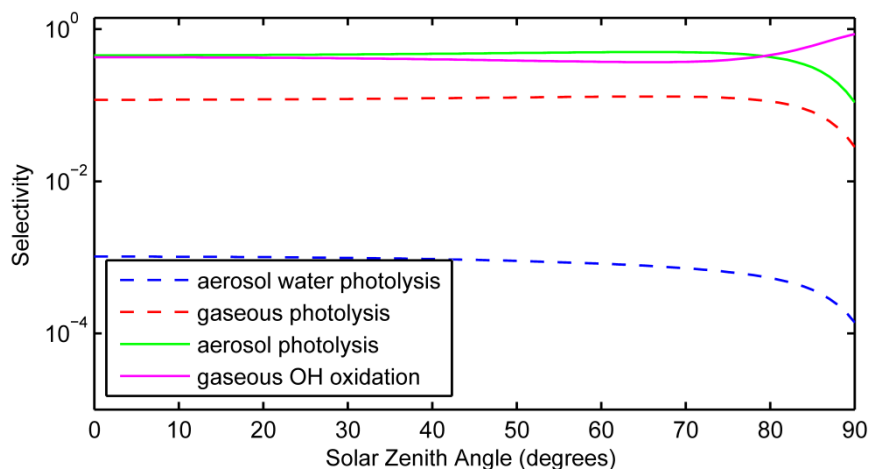


Figure 30. Calculated PA removal selectivity of key chemical processes likely to affect PA in a polluted atmosphere without cloud or fog droplets. The selectivity of photolysis in aerosol water, photolysis in the gas-phase, photolysis in the organic-aerosol-phase, and oxidation by OH radical in the gas phase are compared. (Total organic aerosol concentration is $20 \mu\text{g m}^{-3}$, liquid water concentration in particles is $50 \mu\text{g m}^{-3}$, and $T = 298 \text{ K}$.)

The results presented here have several atmospheric implications. First, an important conclusion was that even though the direct photochemical removal of PA is not too significant under tropospheric conditions, the observation that the photolysis quantum yield is not remarkably suppressed in condensed phase may provide important insights into photochemical behavior of other SOA constituents and into the SOA aging mechanisms in general. Many organic molecules in the atmosphere are more soluble in water and less volatile than PA to the extent that they are more likely to reside in condensed phase than in the gas phase. This is an important factor, as the general view has been that (photo)chemical aging of atmospheric aerosols is only significant in the gas phase and that molecules embedded in condensed phases are protected from photochemical processing.²⁰⁷ This might be the case when considering oxidative aerosol aging by OH-radicals,²⁰⁸ however, the solar radiation penetrates deep into the particles, and molecules possessing photolabile functional groups must be susceptible to loss via photolysis.

The second important implication deals with the challenge of unique tracer identification. Large variety of different chemical processes take place in the atmosphere in multiple phases, thus specific tracers of this tropospheric chemistry are exceedingly useful for constraining the possible chemical mechanisms. For the gas phase oxidation of PA a tracer has been identified (3-methyl-1,2,3-butanetricarboxylic acid),⁹¹ but no tracers are currently known for photolysis of PA or related species, especially in aqueous phase. One of the objectives in the work in Article III was to identify such a tracer by determining the photolysis products. Whereas the main product, the structural isomer of PA (or limonic acid) cannot be considered as a tracer since it is known to be produced in the ozonolysis reaction of d-limonene,⁷¹ the comprehensive approach to the mechanism of photolysis of PA will be useful for understanding photochemical fates of other water-soluble biogenic carbonyls. It also demonstrates the difficulty of determining unique traces for specific molecules, and brings up the possibility of potential misinterpretation of source apportionment based on tracer measurements. For example, the formation of limonic acid via photolysis of PA could be falsely assigned to oxidation of d-limonene. The choice of PA as a representative molecule of α -pinene oxidation also proved to be relatively good, as will be seen in the following section.

4.3.6 Temperature Dependence of the Aqueous Photochemistry of α -pinene SOA

In addition to the aqueous PA photolysis experiments described above, comparative photolysis experiments of α -pinene SOA in aqueous phase were carried out. α -pinene SOA is a complicated mixture of compounds,²⁰⁹ but it is expected that a large fraction of these compounds should have photophysical properties comparable to photophysics of PA. In order to simplify the data interpretation, dissolved oxygen was removed from solutions by bubbling argon through the samples during photolysis. In the presence of air, the free radicals R initially generated by Norrish type-I processes quickly convert into peroxy radicals, RO₂. The RO₂ chemistry tends to re-generate carbonyls,¹⁹⁸ which interferes with the goal of tracking the progress of photolysis via the decay of the characteristic $\pi^* \leftarrow n$ carbonyl absorption.

Within the first 30 min of the aqueous SOA photolysis, the $\pi^* \leftarrow n$ absorbance at 280 nm decreased on a time scale of minutes, with no clear dependence of the apparent photolysis rate on temperature. At longer photolysis times the

decrease in the absorbance at 280 nm slowed down considerably, again with no clear dependence on temperature. It should be noted that photochemistry at long photolysis times is complicated by multiple secondary reactions and absorbing products. Therefore, significance was placed only on the results obtained at small photolysis times. Spectra of the aqueous SOA photolysis are shown in Fig. 31 and comparison of the rates of photolysis during the first 30 min in varying temperatures is shown in Table 9. The overall conclusion of our observation is that there is no dramatic effect of temperature on photolysis of aqueous SOA.

Another important aspect was to evaluate the suitability of PA as a model compound of α -pinene SOA. This was carried out by comparing the photolysis rates of α -pinene SOA and PA. The photolysis rates

$$J = \phi \int_{\lambda} \sigma(\lambda) F(\lambda) d\lambda$$

of PA and α -pinene SOA were calculated at SZA 10° ($F(\lambda)$,¹⁵³ relevant for conditions in Los Angeles area in the summer at noon) assuming that the average molecular weight of an SOA molecule is the same as that of PA, and the quantum yield of photolysis ϕ is the same. This allowed the determination of the wavelength dependent absorption cross section of α -pinene SOA. This estimation produced a $J_{\text{SOA}}:J_{\text{PA}}$ ratio of 0.8, and thus suggests that PA is a relatively good representative of the α -pinene SOA.

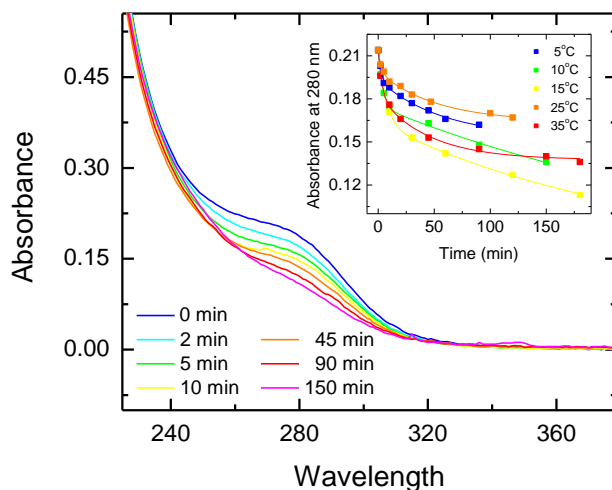


Figure 31. Spectra of the aqueous SOA photolysis at 10°C . The insert shows the decay kinetics of the characteristic carbonyl absorbance at 280 nm.

Table 9. Rates of the decay of the characteristic 280 nm carbonyl peak during the first 30 minutes of the aqueous SOA photolysis at varying temperatures. The rates are calculated from the exponential fits of the 280 nm absorbance as a function of time using Model 1.

T (°C)	R (10^{-3} s^{-1})
5	2.9 ± 0.71
10	3.1 ± 0.68
15	2.7 ± 0.40
25	2.5 ± 0.36
35	2.5 ± 0.58

4.4 Temperature Dependence of the Photolysis in SOA Matrices

4.4.1 Photolysis of the SOA Materials

After investigating the photolysis of aqueous solutions of SOA materials, as described in the previous section, the focus was shifted to photolyzing SOA materials directly, as collected from the flow reactor. Initially, d-limonene SOA samples collected on CaF_2 windows were photolyzed at various temperatures to obtain a general idea whether the temperature has any effect on the photolysis rate. In these preliminary studies, it was observed that lowering the temperature by $\sim 20^\circ\text{C}$ can affect the apparent photolysis rate of the carbonyl compounds in the SOA matrix (tracked via the characteristic $\pi^* \leftarrow n$ transition of carbonyls in the absorption spectrum) by almost an order of magnitude. After this promising initial result was observed, a more detailed study of α -pinene SOA material photolysis was undertaken. α -pinene SOA was chosen instead of limonene SOA due to its more distinguishable carbonyl feature in the absorption spectrum at 280 nm, as shown in Fig. 32. However, these α -pinene SOA experiments showed highly complicated kinetics, where slow spontaneous changes in the physical properties of the SOA material matrix interfered with the chemical changes caused by the photolysis. For example, it was observed that the film of SOA

sandwiched between two CaF₂ windows in the absorption spectrometer shown in Fig. 7 (a-c) was slowly changing shape, and little “islands” slowly developed in the film (Fig. 7 d). This made the interpretation of the observations challenging because this experiment relied on the optical transmission through the film, which depended on both the thickness and uniformity of the film. Control experiments were carried out, in which the visual shape changes and isolating some of the matrix material into “islands” were observed as a function of time, and it was noticed that those changes were delayed at 0°C compared to 25°C. Presence of radiation appeared to promote these physical changes (presumably, in addition to the chemical transformations taking place in the film), which was observed in the 0°C matrix photolysis experiments. For example, 12 hours of waiting at 0°C did not affect the matrix visually, but photolysis that was carried out at 0°C without initial waiting period produced the same physical changes (including the island formation) seen in control experiments at 25°C.

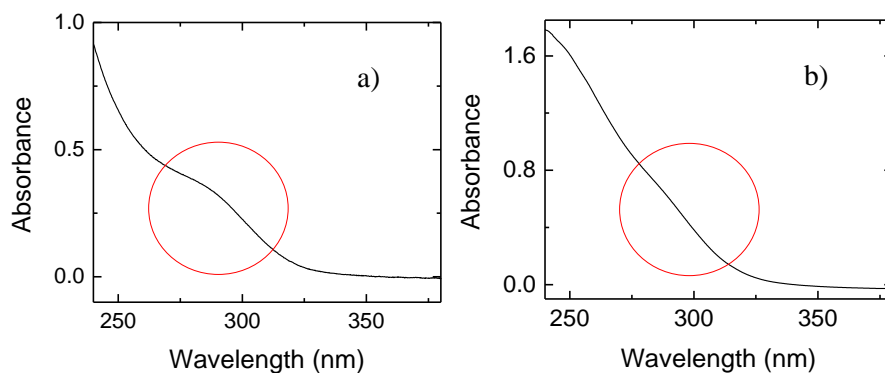


Figure 32. Absorption spectrum of a) *a-pinene* SOA, b) *d-limonene* SOA prepared in the flow reactor and collected with an impactor on a CaF₂ window. The characteristic 280 nm carbonyl absorption is highlighted.

Despite these difficulties, reasonably useful and informative data were obtained in some of the SOA film experiments. Sample spectra of α -pinene SOA recorded at different stages of photolysis are presented in Fig. 33. The band at 280 nm corresponds to the $\pi^* \leftarrow n$ transition of carbonyls in the SOA film. The insert in Fig. 33 shows the corresponding kinetics of disappearance of the $\pi^* \leftarrow n$ absorbance. The time dependence is not reproducible from one experiment to the next because of the physical changes in the film described

here, but the general trend is the reduction on the intensity of the $\pi^* \leftarrow n$ transition of carbonyls, as expected. Figure 34 shows the kinetics of the α -pinene matrix photolysis over a longer time period, where the 12 hour waiting period prior to the photolysis is included. The reduction in the $\pi^* \leftarrow n$ is apparent, but it is clear that the effects of the physical changes in the film persist even after 30 hours. It should be noted, that the actinometry experiments with azoxybenzene/KOH in octanol carried out under the same conditions as the SOA photolysis were successful, demonstrating that the experimental setup was functioning properly. Therefore, the complicated time dependence was definitely due to the physical annealing of the film.

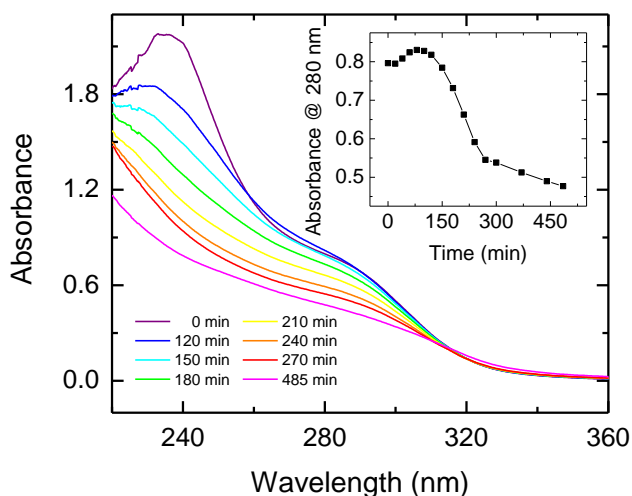


Figure 33. α -pinene photolysis and the decay of the characteristic 280 nm peak at 0°C. This experiment was done without prior waiting.

To avoid the physical changes in the matrix material caused by prolonged photolysis times, a different spectral window and intensity was chosen to accelerate the photolysis. The 300 nm band pass filter was replaced by 295 nm high pass filter and a BG1 blue filter. This produced photolysis source that included more visible radiation, but with significantly stronger intensity on the whole than the previous setup. As anticipated, the increased spectral intensity of the UV-lamp was able to photolyze the SOA samples faster than the physical changes took place. These experiments showed that the photolysis of the SOA samples was indeed too slow under the chosen experimental conditions to be reliably observed. In the future these

experiments will be improved by designing more sophisticated sample holders to prevent the film from spreading during the experiments.

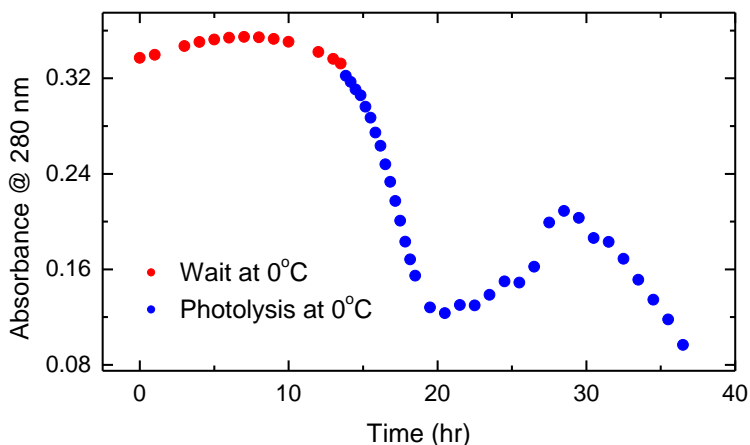


Figure 34. The kinetic behavior of α -pinene SOA matrix at 0°C. The red dots present the waiting period at 0°C and the blue dots represent the subsequent photolysis. In this experimental design, it was difficult to tell whether the “bump” at 30 hours was a result of chemical change induced by photodegradation or physical evolution of the film morphology.

4.4.2 Photolysis of the α -pinene SOA Matrix with 24-DNP as a Probe

As the “pure” SOA matrix photolysis experiments were complicated by the spontaneous changes in the morphology of the SOA film, and as these experiments showed that the timescales of the processes were slow (characteristic time scales of hours), a different experimental protocol was adopted. In the next series of experiments, the focus shifted from the photolysis of SOA compounds in the “pure” SOA matrix to a photolysis of a suitable probe molecule embedded in the SOA matrix. The atmospherically relevant and strongly absorbing 2,4-dinitrophenol (24-DNP) molecule was chosen as a probe. 24-DNP absorbs significantly stronger than any of the SOA compounds, and it can be expected to photolyze faster. Therefore, it should be possible to investigate the photolysis rates of the probe molecule at different temperatures with a minimal effect of the SOA matrix restructuring on the probe molecule’s kinetics.

The spectra of 24-DNP possesses different characteristics based on the solvent pH and concentration. 24DNP is acidic, with $pK_a = 4.1$, and therefore

is almost fully ionized at small concentrations and/or in a basic solution. At high concentrations and/or in an acidic solution the non-ionized, molecular form dominates. The effect of the acid-base changes on the absorption spectrum of 24-DNP is demonstrated in Fig. 35. Based on comparison of the spectra, it can be concluded that in SOA, which is acidic and has relatively high concentration of 24-DNP, it is not ionized.

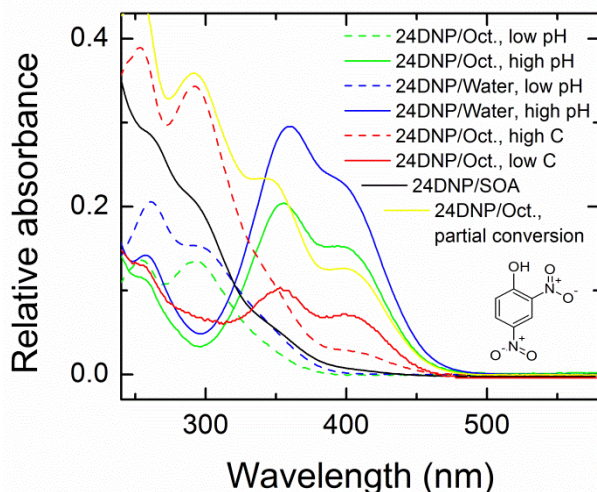


Figure 35. Comparison of the different concentrations and pH-values of 24-DNP solutions. The solid line refers to lower concentrations and higher pH-values and the dashed lines refer to high concentrations and low pH-values. The absorbance at the y-axis is scaled to show the shapes of the spectra and the absorbance values are not the absolute values of the different conditions.

Figure 36 compares the pure SOA matrix and the matrix embedded with 24-DNP prepared in similar manner, showing the different characteristic absorbances. The insert shows the difference spectrum. The extinction coefficient of 24-DNP is also known to change with solvent.²¹⁰ Figure 37 (a-c) presents the calculated extinction coefficients in water, octanol, and isopropanol, respectively, values that were needed in the analysis of this work.

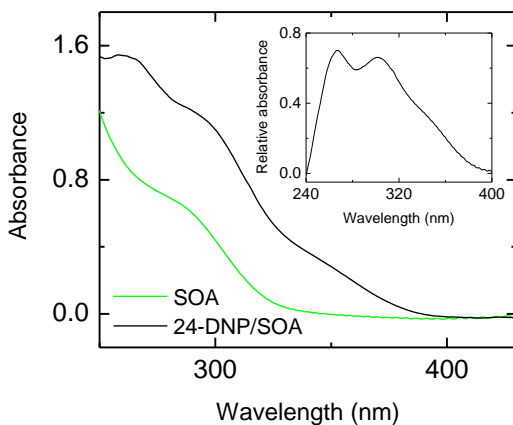


Figure 36. Absorption spectra of pure *a*-pinene SOA and 24-DNP embedded in *a*-pinene SOA matrix. The spectra show the different characteristics, and the insert presents the difference spectrum.

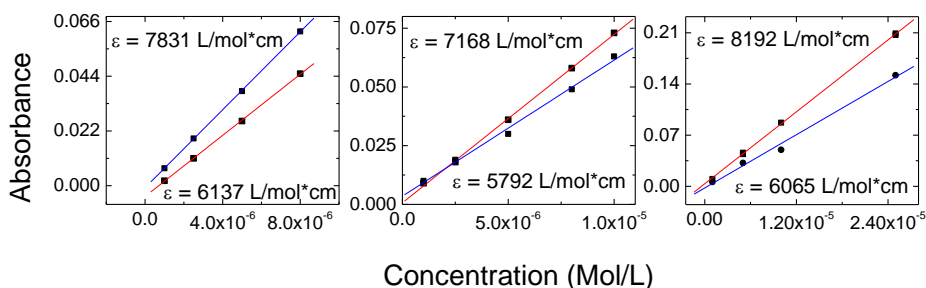


Figure 37. Measured molar extinction coefficients of 24-DNP in different solvents. Beer-Lambert plots in a) water, b) octanol, and c) isopropanol. The absorbances were monitored in the molecular form (pH ~ 1) at 290 nm (blue) and in the ionic form (pH ~8) at 405 nm (red). The measurements were carried out at 20°C. The extinction coefficients were extracted from the linear fits of the Beer-Lambert plots.

The spectra recorded at different stages of the photolysis of SOA/24-DNP films at 25°C and 0°C are shown in Figures 38 a) and b), respectively. Inserts in both of the figures show the behavior of the decay of the absorbance at 290 nm. It can be seen from the spectra, as well as from the absorbance decay rates listed in Table 9, that the 25°C decrease in temperature slows down the photolysis process significantly.

While these experiments were highly suggestive of significant temperature (or viscosity) effects on the photolysis of 24-DNP inside the SOA matrix, their quantitative interpretation was challenging. Our experiments revealed a pronounced increase in the visible absorbance upon photolysis, e.g., at 400 nm. But in order to convert the measured 400 nm absorbance change rates into physically meaningful photolysis rate constants, extinction coefficients of 24-DNP photolysis products dissolved in an SOA film are required. The experiments on characterization of the products of photolysis (described below) suggested that multiple species were produced, making it difficult to ascribe the growing absorbance at 400 nm to a specific product. The absorbance at 290 nm should be dominated by 24-DNP in the limit of low photolysis times. However, if one of the products also absorbs at 290 nm (which is likely) one cannot convert the time-dependent decrease in the 290 nm absorbance into the photolysis rate and photolysis quantum yield without making simplifying assumptions.

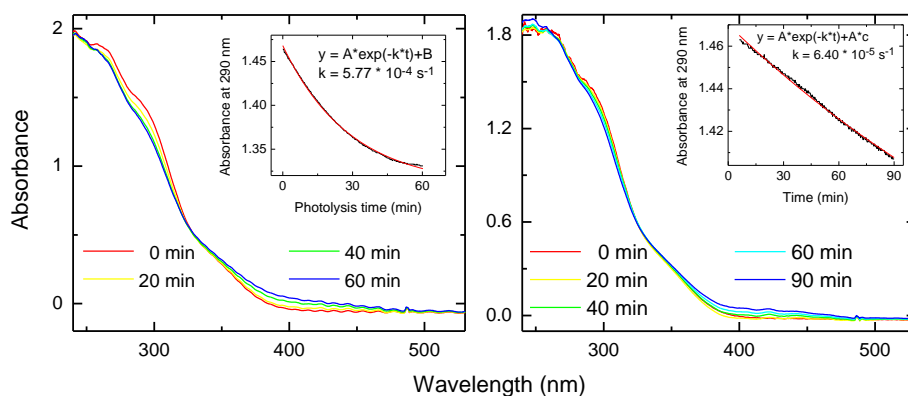


Figure 38. Photolysis of 24-DNP dispersed in α -pinene SOA matrix at a) 25°C (total photolysis time 60 min) and b) 0 °C (total photolysis time 90 min).

Table 10. Rates of 24-DNP/ SOA photolysis from separate experiments calculated using Model 1 at temperatures 0-25°C.

T (°C)	R _{290nm} (s ⁻¹)
25	5.77 ± 0.050 x 10 ⁻⁴
25	4.73 ± 0.077 x 10 ⁻⁴
20	2.85 ± 0.009 x 10 ⁻⁴
20	2.48 ± 0.041 x 10 ⁻⁴
15	1.77 ± 0.020 x 10 ⁻⁴
15	2.03 ± 0.023 x 10 ⁻⁴
10	1.56 ± 0.008 x 10 ⁻⁴
10	9.86 ± 0.010 x 10 ⁻⁵
5	8.96 ± 0.035 x 10 ⁻⁵
5	8.97 ± 0.099 x 10 ⁻⁵
0	6.40 ± 0.034 x 10 ⁻⁵
0	7.31 ± 0.024 x 10 ⁻⁵

The most logical assumption that can be made under the circumstances is similar to that used in Model 1 of the PA section (4.3.2) of this thesis; specifically, that there is a single product that does not undergo secondary photolysis. Limiting the photolysis experiment to low photolysis times should make this assumption more accurate.

According to Model 1, the normalized absorbance in this case should decay as follows:

$$\frac{A_{10}(t)}{A_0} = \beta + (1 - \beta) \cdot e^{-k_{24DNP} \cdot t} \quad (1)$$

where β , and k_{24DNP} are fitting parameters and $\beta = \varepsilon_{Prod} / \varepsilon_{24-DNP}$, similarly as in the case of PA. The experimental data of the decay of the 290 nm feature was possible to fit to the data measured at temperatures 10°C and higher. At lower temperatures, the time frame of the experiments was not able to fully capture the exponential behavior, but was limited to the initial, linear-looking part of the kinetics. This was taken into account by modifying Model 1 to assume that the ratio of the initial absorbance and the offset described by the parameter β should stay relatively constant at all temperatures. Therefore, the parameter β was fixed in the fits to the average value (6.67) obtained from experiments at temperatures above 10°C. The justification for fixing the value of β is that the 290 nm extinction coefficient of 24-DNP and

its photolysis product are not expected to vary significantly with temperature, which is demonstrated in Fig. 39 in both molecular and in ionic form. The temperature had a slight effect on the absorption cross sections, but this is not expected to affect the extinction coefficient significantly. The cause for caution in considering Model 1 is that was developed for an optically-thin films, where the absorbance needs to be $\ll 1$. It may not apply in this case, as the film's absorbance exceeds unity at some of the wavelengths covered by photolyzing radiation (290-500 nm). The unsuccessful attempts to prepare films with lower initial absorbances were described in section 2.5. Therefore, a more complicated model needs to be considered before for example photolysis quantum yields can be calculated quantitatively. More experiments are underway to resolve this issue.

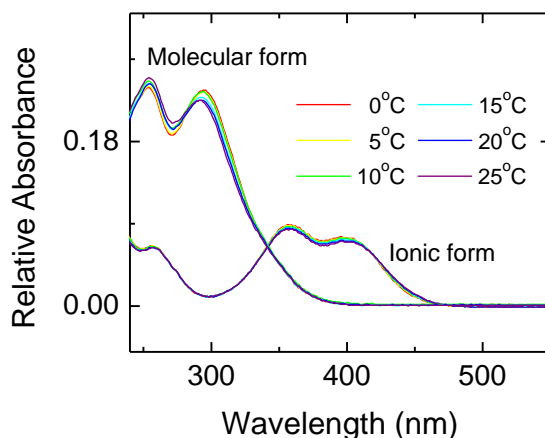


Figure 39. The UV-Vis absorption spectra of 24-DNP in octanol in molecular and ionic form.

4.4.3 Temperature Dependence of the Photochemistry of 24-DNP in Octanol

As mentioned in the introduction, temperature can affect condensed-phase photochemistry directly, by slowing down unimolecular decomposition of photoexcited molecules, and indirectly, by reducing the viscosity of the SOA matrix thus constraining molecular motion. In order to decouple the direct and indirect effects, parallel measurements of 24-DNP photolysis in octanol films, which remain in liquid form above $-16\text{ }^{\circ}\text{C}$ were carried out. Octanol is a

relatively viscous liquid, but it is less viscous than the α -pinene SOA matrix, thus providing a good environment to decouple the viscosity and temperature effects on the photochemistry of 24-DNP. Octanol is also a widely used organic phase prototype, and used commonly in water-organic phase partitioning studies.

The spectra of 24-DNP taken during its photolysis in an octanol film at 25°C and 0°C are shown in Fig. 40, and the inserts show the decay of the absorbance at 290 nm. The film thickness was estimated to be $\sim 30 \mu\text{m}$ based on the geometry of the liquid spot formed between the windows and the volume of the sample droplet. Table 10 compares the decay rates and quantum yields of the 290 nm absorbance. The absorbance decay rates of the photolysis carried out in all of the temperatures could be easily fitted to the exponential decay described in Model 1. The quantum yields were calculated in similar manner as described in detail in Article III of this thesis, a representative spectra of the actinometer photolysis is shown in Fig. 41. As seen from the rate constants and quantum yields listed in Table 10, no clear temperature dependence was observed.

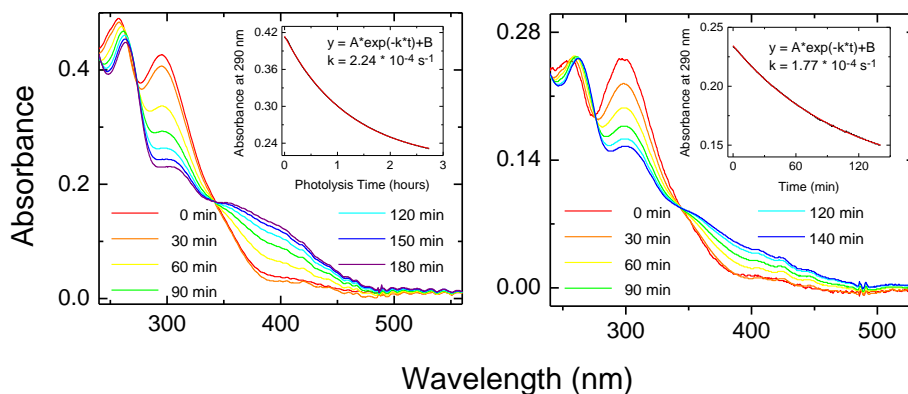


Figure 40. Photolysis of 24-DNP dispersed in octanol at 25°C (a) and 0°C (b). The inserts show the decay of the 290 nm absorbance.

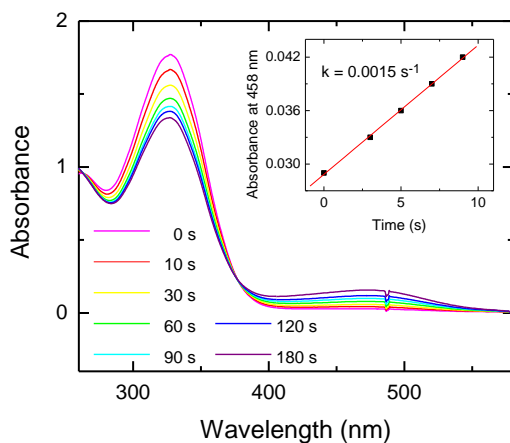


Figure 41. *Azoxybenzene actinometer in octanol/KOH film. The insert shows the growth of the characteristic 458 nm peak.*

Presence of multiple products formed in photolysis was supported by LC-ESI-MS measurement of the products in the photolyzed sample (See Fig. 42). More experiments and calculations are currently underway to explore the photolysis products and the photolysis mechanism.

It was verified that photodissociation of 4×10^{-5} M 24-DNP in water (Fig. 43) was negligible ($QY \sim 4 \times 10^{-6}$), result that was consistent with previous observations of aqueous photolysis of 24-DNP.¹³⁷ The large disparity in the apparent photolysis rate in water vs. octanol implied that the photochemistry may be driven not necessarily by direct photolysis of 24-DNP but by a reaction of the photoexcited 24-DNP with octanol (or, in the SOA case, with various organic species in the SOA phase).

The photolysis of 24-DNP/octanol below octanol's freezing points was carried out also. It was verified that the sample stayed frozen by closely monitoring the sample's transmission (which would change suddenly upon melting) and also visually. It was observed that the photolysis reaction had an "induction period", during which no change in the film absorbance occurred, and the 290 nm absorbance started to go down only ~ 15 minutes after the photolysis started. The following decay was exponential, and even faster than the fastest photolysis in the liquid samples. This suggests a different photolysis mechanism in the frozen films. One explanation could be the film separating into solid octanol and a thin liquid layer including the 24-DNP which then photolyzes with a fast rate. Another explanation could be

the octanol forming crystals upon freezing and the 24-DNP escaping to high concentration droplets surrounding the crystals. This behavior clearly needs more attention in the future. A photograph of the frozen film and the kinetics of the 290 nm absorbance are shown in Fig. 44.

Table 11. Rates and quantum yields for the decay of the 290 nm peak during 24-DNP photolysis in a) octanol and b) water at varying temperatures. The quantum yield values at -10°C and lower were not included due to uncertainty of the actinometer's photolysis mechanism at lower temperatures.

a)

Temperature (°C)	Rate constant (*10 ⁻⁴ s ⁻¹)	Quantum Yield (*10 ⁻³)
25	2.20 ± 0.011	1.6
25	2.04 ± 0.006	2.0
25	2.55 ± 0.008	1.7
15	1.64 ± 0.010	1.3
15	1.74 ± 0.008	1.4
15	2.59 ± 0.010	1.5
10	1.78 ± 0.008	1.8
10	2.02 ± 0.008	1.2
10	2.36 ± 0.005	1.1
5	1.48 ± 0.009	1.4
5	1.80 ± 0.008	1.2
5	1.48 ± 0.004	1.6
0	1.77 ± 0.012	1.3
0	1.48 ± 0.011	1.7
-10	1.23 ± 0.009	-
-10	1.01 ± 0.007	-
-17 (liq.)	1.13 ± 0.007	-
-17 (liq.)	1.07 ± 0.014	-
-18 (solid)	4.38 ± 0.029	-
-18 (solid)	5.58 ± 0.033	-

b)

Temperature (°C)	Rate constant (*10 ⁻⁶ s ⁻¹)	Quantum Yield (*10 ⁻⁶)
20	0.95 ± 0.069	3.6
20	1.11 ± 0.222	4.4

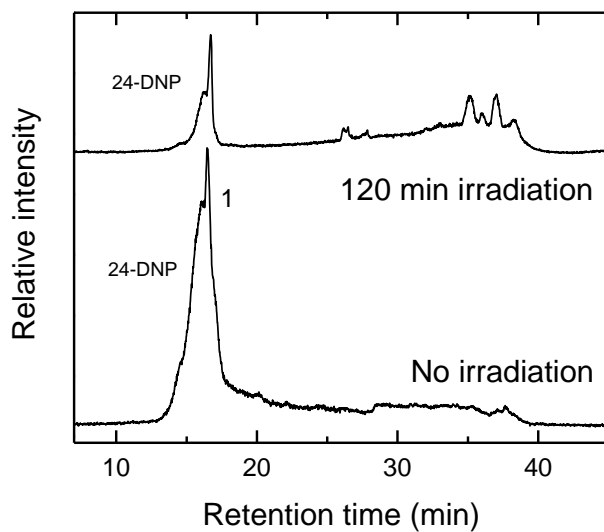


Figure 42. LC-ESI-MS (-) ion mode total-ion-current chromatograms: 24-DNP/octanol before photolysis (lower trace); 24-DNP/octanol after 120 min photolysis (upper trace).

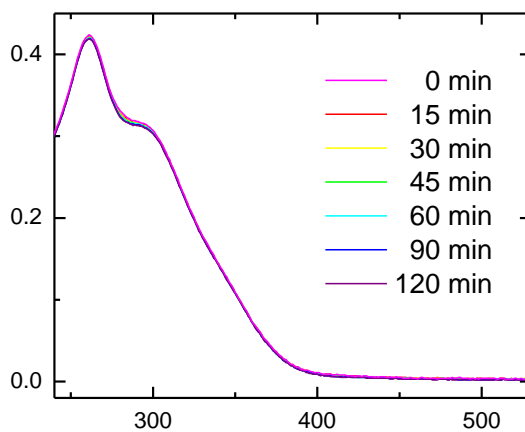


Figure 43. Photolysis of 4.0×10^{-5} M 24-DNP in acidified ($pH = \sim 1.4$) water solution at 20°C .

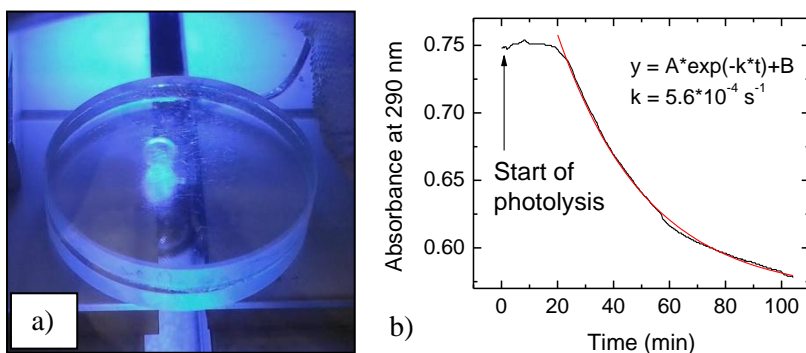


Figure 44. The photolysis of the frozen 24-DNP/octanol film (a) and the kinetics of the 290 nm absorbance (b). The kinetics of the frozen sample differed from the liquid films, and suggests a different mechanism.

4.4.4 Conclusions and Atmospheric Implications

The photolysis experiments carried out in different matrices, with and without the 24-DNP probe, provided interesting new results and shed light into the viscosity effects of photolysis. The photolysis efficiency of the 24-DNP was influenced by the type of the surrounding media (water, octanol, or SOA), as well as by the temperature (which directly affects viscosity of the film). It was also observed that freezing the octanol films produced a change in the photolysis mechanism, an observation that requires more attention in the future. The photolysis products were briefly explored by performing LC-ESI-MS experiments, but more detailed study of the products and mechanisms is currently underway, including both experiments and calculations. Table 12 summarizes all the observations of the 24-DNP experiments.

Table 12. Summary of the observations of photochemistry of 24-DNP dispersed in matrixes with varying viscosity and temperature.

Matrix	Characteristics	Photolysis rate	Effect of T on 24-DNP photolysis rate in this matrix
Water	Liquid	No photolysis	Not investigated here
Octanol	Viscous organic liquid	Fast	No significant effect
SOA	More viscous organic liquid (or solid)	Fast	Photolysis slows down with temperature

Preliminary results showed that SOA materials produce highly complicated kinetics when the films were photolyzed. Due to these complications, the focus was centered on following the photolysis kinetics of 24-DNP as a function of temperature in different environments. One of the main findings of these experiments was that 24-DNP photolyzed much more efficiently in organic environment than in water ($QY_{\text{water}} = \sim 4 \times 10^{-6}$ vs. $QY_{\text{oct}} = \sim 1.5 \times 10^{-3}$). This behavior brings up important atmospheric implications as 24-DNP resides as likely in water and in organic phase based on its octanol-water partitioning coefficient ($K_{\text{ow}} = 8738$ by Ref. 145). The difference in the photolysis efficiency itself is necessarily not a surprise, as it is known that photochemistry of nitrophenols is dominated by hydrogen abstraction reaction from the solvent, and alcohols are more efficient hydrogen donors than water. It is also plausible to assume that the photolysis mechanism in octanol and SOA are similar due to similar spectral features. It should be noted that at 25 °C the photolysis was observed to be faster in the SOA film, which is likely due to the multifunctional nature of SOA compounds (= more possible hydrogen donors from secondary hydroxyl groups).

The difference in the temperature dependence of the photolysis in different organic media is clearly demonstrated by looking at the Arrhenius plots of the photolysis reaction (Fig. 45). The activation energies calculated from these plots for 24-DNP/SOA and 24-DNP/octanol are 53 kJ/mol and 12 kJ/mol, respectively. This difference is striking as it is, but also the fact that the Arrhenius equation captures the behavior of the photolysis well is of significance. In atmospheric modeling, for instance, this result could mean that the rates of the photolysis of these systems could be determined based on only two factors, the activation energy E_a and the pre-exponential factor A (which is not discussed here).

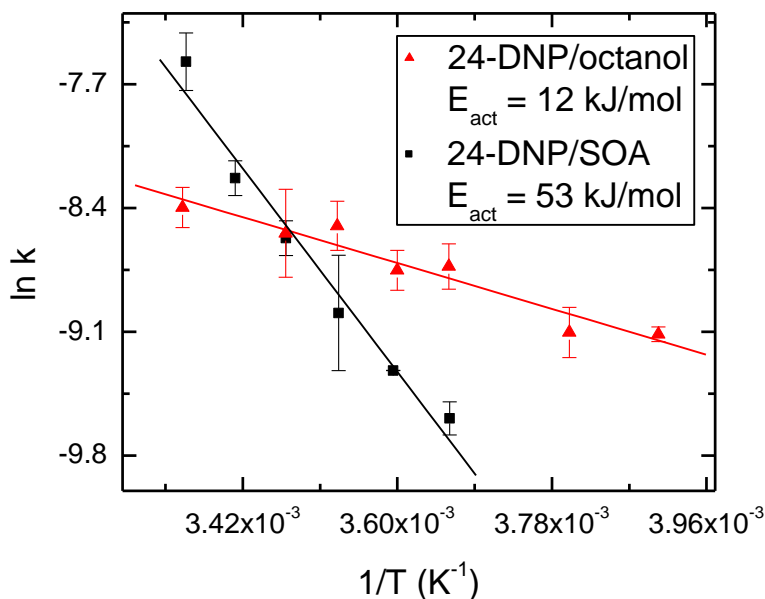


Figure 45. Arrhenius plot for the 24-DNP photolysis in SOA matrix. The points are averaged values of different experiments at varying temperatures (see Tables 10 and 11). The frozen sample points were omitted due to a different mechanism. Activation energies are calculated from the linear fits.

The Arrhenius behavior and the activation energies determined from the slopes of the plots also seem to correlate with the viscosity changes. The viscosity of octanol in room temperature is only 7.3 mPa*s, and it is not expected to increase more than one order of magnitude or less (based on extrapolation of the data in Ref. 211 to -10°C). This slight trend in viscosity correlates with the Arrhenius behavior, as the higher viscosity changes of SOA correlate with the higher activation energy in the SOA matrix. α -pinene SOA have been measured to have viscosity of $\sim 10^3$ Pa*s (Ref. 122) in the experimental conditions applied here. However, as there seems to be sufficient amount of experimental evidence to ascribe the difference of photolysis efficiency (and activation energy) to the viscosity changes, the possible contribution from changing reaction mechanism as the temperature is lowered cannot be disregarded. As SOA is a complicated mixture of different organics, a combination of multiple functional groups could be responsible for the described behavior, and change the photolysis mechanism. This again underlines the importance of further studies, where the already mentioned photolysis products and mechanisms will be explored both experimentally and computationally.

The obvious decrease in photochemical activity as a function of decreasing temperature in the case of 24-DNP/SOA could also have implications to the stratospheric aerosol chemistry. Recently, Murphy *et al.* published a study exploring the chemical composition of stratospheric aerosol particles.²¹² They observed that based on the composition-resolved size distributions at ~19 km altitude, organic volume is unchanged compared to that at the tropical tropopause. This could sound unexpected, as the atmospheric organics originating from the troposphere are multifunctional and thus photolabile. However, in the light of the experiments described in this thesis, decreasing temperature can have significant suppressing effect to the photochemistry of organic material as stratospheric temperatures are < 0 °C, and could potentially explain the observations by Murphy *et al.*²¹²

It was concluded in this work, that the decrease of the photolysis rates of different matrices at different temperatures can be ascribed to viscosity effects. Previous studies that have explored the phase state of aerosol particles have shown that the glassy, viscous particle phase can influence many molecular properties, such as partitioning of semi-volatiles, heterogeneous reaction rates, atmospheric lifetimes, etc.^{126,213,214} It has also been shown that the viscosity of SOA particles strongly correlates with molecular mass and water content, thus playing a role in determining whether an organic aerosol particle is in a liquid, semi-solid, or glassy phase state.¹³¹ These observations state that dry particles with high molecular masses have the highest viscosities. In SOA particles, organic molecules are known to oligomerize, and this has a direct effect on the SOA viscosity. It should also be emphasized that reaction rates reduced as a result of increasing viscosity are not unknown, for example polymerization reaction at an ultra-viscous limit is known to terminate.²¹⁵ Koop *et al.* underlined the need of more detailed understanding of oligomerization and polymerization in SOA particles, in addition to the more discussed effects of viscosity to diffusivity.^{131,132,216} The experimental results presented in this thesis shed more light on the dynamics of SOA particles, since the reduction of photolability as the viscosity increases is clearly observed. This obviously brings up more detailed questions to be addressed in the future, as how will the increased viscosity change the photodissociation products, how will it affect the lifetimes of atmospheric particles, and how will the mechanism of the photolysis change as the surrounding matrix goes through phase changes.

5. Concluding Remarks

This thesis expanded our fundamental understanding of reactions taking place in different heterogeneous environments and condensed phases by exploring photochemistry of several model systems. An exotic noble-gas molecule, HArF, was investigated under cryogenic conditions. The view of the HArF molecule as that of a “supermolecule” was discussed to emphasize the fact that the surrounding matrix can participate in stabilization of the molecules it contains and significantly change the chemistry and mechanisms of reacting species. In addition, this thesis concentrated on understanding atmospherically relevant photochemical reactions in multiple phases, as well as reaction mechanisms leading to the formation or changing the concentrations of key air pollutants. The role of N₂O₄ hydrolysis was explored, showing an important possible contribution to HONO formation via symmetric → asymmetric isomerization reaction assisted by dangling surface hydrogens. Two atmospherically relevant surfaces, ice and silica, were modeled, showing surprisingly similar behavior thus suggesting a more general mechanism. Combination of various experimental and theoretical methods investigating the aqueous photochemistry of α-pinene SOA and *cis*-pinonic acid were utilized, providing important new insights into photochemical fates of water-soluble biogenic carbonyls. Photolysis products, reaction mechanism, and quantum yields were reported and the difficulty of assigning unique tracer molecules to monoterpenes was also demonstrated. The effect of viscosity and temperature on photochemical reactions taking place in aerosol particles has not been previously investigated, and observations revealing the effect of increasing viscosity to photolysis rates in particles were reported in this thesis for the first time. More specifically, photochemistry of 2,4-dinitrophenol in various environments was explored, with results demonstrating significant decrease of photolysis efficiency in highly viscous media. On the whole, this thesis bears direct relevance to understanding processes responsible for the climate change and air pollution, and thus it contributes significantly to the body of fundamental knowledge of atmospheric sciences.

References

- (1) Cheung, K.; Shafer, M. M.; Schauer, J. J.; Sioutas, C., *J. Air Waste Manage.* **2012**, *62*, 541-556.
- (2) Silva, R. A.; West, J. J.; Zhang, Y.; Anenberg, S. C.; Lamarque, J-F.; Shindell, D. T.; Collins, W. J.; Dalsoren, S.; Faluvegi G.; Folberth, G.; Horowitz, L. W.; Nagashima, T.; Naik, V.; Rumbold, S.; Skeie, R.; et al., *Environ. Res. Lett.*, **2013**, *8*, 034005
doi:10.1088/1748-9326/8/3/034005
- (3) Sander, S. P.; Abbatt, J.; Barker, J. R.; Burkholder, J. B.; Friedl, R. R.; Golden, D. M.; Huie, R. E.; Kolb, C. E.; Kurylo, M. J.; Moortgat, G. K.; Orkin, V. L.; Wine, P. H. Chemical Kinetics and Photochemical Data for Use in Atmospheric Studies. In *Evaluation No. 17*; JPL Publication Jet Propulsion Laboratory, Pasadena, 2011; Vol. 10-6.
- (4) Finlayson-Pitts B. J., J. N. P., Jr. *Chemistry of the Upper and Lower Atmosphere: Theory, Experiments and Applications*; Academic Press, 2000.
- (5) Seinfeld, J. H.; Pandis, S. N. *Atmospheric Chemistry and Physics - From Air Pollution to Climate Change*; John Wiley & Sons, 2006.
- (6) Hallam, H. E. E. *Vibrational Spectroscopy of Trapped Species: Infrared and Raman Studies of Matrix-isolated Molecules, Radicals and Ions*; John Wiley & Sons Ltd: London, 1973.
- (7) Turro, N. J.; Scaiano, J. C.; Ramamurthy, V. *Modern Molecular Photochemistry of Organic Molecules*; University Science Books: USA, 2010.
- (8) Khriachtchev, L.; Räsänen, M.; Gerber, R. B., *Acc. Chem. Res.* **2008**, *42*, 183-191.
- (9) Lignell, A.; Khriachtchev, L., *J. Mol. Struct.* **2008**, *889*, 1-11.
- (10) Lignell, A.; Khriachtchev, L.; Lundell, J.; Tanskanen, H.; Räsänen, M., *J. Chem. Phys.* **2006**, *125*, 184514, DOI: 10.1063/1.2378624
- (11) McDowell, S. A. C. *Curr. Org. Chem.*, **2006**, *10*, 791-803.
- (12) Lundell, J.; Khriachtchev, L.; Pettersson, M.; Räsänen, M. *Low Temp. Phys.* **2000**, *26*, 680-690.
- (13) Pettersson, M.; Nieminen, J.; Khriachtchev, L.; Räsänen, M., *J. Chem. Phys.* **1997**, *107*, 8423-8431.
- (14) Khriachtchev, L.; Tanskanen, H.; Räsänen, M., *J. Chem. Phys.* **2006**, *124*, 181101, doi: 10.1063/1.2201445
- (15) Pettersson, M.; Khriachtchev, L.; Lundell, J.; Jolkkonen, S.; Räsänen, M., *J. Phys. Chem. A* **2000**, *104*, 3579-3583.
- (16) Khriachtchev, L.; Pettersson, M.; Runeberg, N.; Lundell, J.; Räsänen, M., *Nature* **2000**, *406*, 874-876.
- (17) Khriachtchev, L.; Pettersson, M.; Lundell, J.; Räsänen, M., *J. Chem. Phys.* **2001**, *114*, 7727-7730.
- (18) Khriachtchev, L.; Pettersson, M.; Lignell, A.; Räsänen, M., *J. Am. Chem. Soc.* **2001**, *123*, 8610-8611.
- (19) Khriachtchev, L.; Lignell, A.; Räsänen, M., *J. Chem. Phys.* **2004**, *120*, 3353-3357.
- (20) Lundell, J.; Chaban, G. M.; Benny Gerber, R., *Chem. Phys. Lett.*, **2000**, *331*, 308-316.
- (21) Runeberg, N.; Pettersson, M.; Khriachtchev, L.; Lundell, J.; Räsänen, M., *J. Chem. Phys.* **2001**, *114*, 836-841.
- (22) Bihary, Z.; Chaban, G. M.; Gerber, R. B., *J. Chem. Phys.*, **2003**, *119*, 11278-11284.
- (23) Li, H.; Xie, D.; Guo, H., *J. Chem. Phys.* **2004**, *120*, 4273-4280.
- (24) Avramopoulos, A.; Reis, H.; Li, J.; Papadopoulos, M. G., *J. Am. Chem. Soc.* **2004**, *126*, 6179-6184.
- (25) Bihary, Z.; Chaban, G. M.; Gerber, R. B., *J. Chem. Phys.* **2002**, *116*, 5521-5529.
- (26) Jolkkonen, S.; Pettersson, M.; Lundell, J., *J. Chem. Phys.* **2003**, *119*, 7356-7364.
- (27) Bochenkova, A. V.; Firsov, D. A.; Nemukhin, A. V. *Chem. Phys. Lett.* **2005**, *405*, 165-171.
- (28) Bochenkova, A. V.; Khriachtchev, L.; Lignell, A.; Räsänen, M.; Lignell, H.; Granovsky, A. A.; Nemukhin, A. V., *Phys. Rev. B* **2008**, *77*, 094301. doi: 10.1103/PhysRevB.77.094301
- (29) Bochenkova, A. V.; Bochenkov, V. E.; Khriachtchev, L., *J. Phys. Chem. A* **2009**, *113*, 7654-7659.
- (30) Pettersson, M.; Khriachtchev, L.; Roozeman, R.-J.; Räsänen, M. *Chem. Phys. Lett.* **2000**, *323*, 506-513.
- (31) Tanskanen, H.; Khriachtchev, L.; Lignell, A.; Räsänen, M.; Johansson, S.; Khyzhniy, I.; Savchenko, E. *Phys. Chem. Chem. Phys.*, **2008**, *10*, 692-701.

- (32) Khriachtchev, L.; Lignell, A.; Räsänen, M., *J. Chem. Phys.* **2005**, *123*, 064507, doi: 10.1063/1.1953467
- (33) Beyer, M. K.; Bondybey, V. E.; Savchenko, E. V. *Low Temp. Phys.*, **2003**, *29*, 792-794.
- (34) Lignell, A.; Khriachtchev, L.; Lignell, H.; Räsänen, M., *Phys. Chem. Chem. Phys.* **2006**, *8*, 2457-2463.
- (35) Khriachtchev, L.; Isokoski, K.; Cohen, A.; Räsänen, M.; Gerber, R. B., *J. Am. Chem. Soc.* **2008**, *130*, 6114-6118.
- (36) Caldwell, W. A.; Nguyen, J. H.; Pfrommer, B. G.; Mauri, F.; Louie, S. G.; Jeanloz, R. *Science* **1997**, *277*, 930-933.
- (37) Sanloup, C.; Schmidt, B. C.; Perez, E. M. C.; Jambon, A.; Gregoryanz, E.; Mezouar, M. *Science* **2005**, *310*, 1174-1177.
- (38) Zhang, R.; Tie, X.; Bond, D. W., *Proc. Natl. Acad. Sci.* **2003**, *100*, 1505-1509.
- (39) Stutz, J.; Aliche, B.; Neftel, A., *J. Geophys. Res. Atmos.* **2002**, *107*, 8192, doi:10.1029/2001JD000390
- (40) Lammel, G.; Cape, J. N., *Chem. Soc. Rev.* **1996**, *25*, 361-369
- (41) Finlayson-Pitts, B. J.; Wingen, L. M.; Sumner, A. L.; Syomin, D.; Ramazan, K. A. *Phys. Chem. Chem. Phys.* **2003**, *5*, 223-242.
- (42) de Jesus Medeiros, D.; Pimentel, A. S., *J. Phys. Chem. A* **2011**, *115*, 6357-6365.
- (43) Givan, A.; Loewenschuss, A., *J. Chem. Phys.* **1989**, *90*, 6135, doi: 10.1063/1.456379
- (44) Givan, A.; Loewenschuss, A., *J. Chem. Phys.* **1989**, *91*, 5126, doi: 10.1063/1.457609
- (45) Givan, A.; Loewenschuss, A., *J. Chem. Phys.* **1991**, *94*, 7562, doi: 10.1063/1.460192
- (46) Wang, J.; Koel, B. E., *J. Phys. Chem. A* **1998**, *102*, 8573-8579.
- (47) Wang, J.; Voss, M. R.; Busse, H.; Koel, B. E., *J. Phys. Chem. B* **1998**, *102*, 4693-4696.
- (48) Wang, J.; Koel, B. E., *Surf. Sci.* **1999**, *436*, 15-28.
- (49) Pimentel, A. S.; Lima, F. C. A.; da Silva, A. B. F., *Chem. Phys. Lett.* **2007**, *436*, 47-50.
- (50) Pimentel, A. S.; Lima, F. C. A.; da Silva, A. B. F., *J. Phys. Chem. A* **2007**, *111*, 2913-2920.
- (51) Jung, Y.; Marcus, R. A. *Journal of the American Chemical Society* **2007**, *129*, 5492-5502.
- (52) Narayan, S.; Muldoon, J.; Finn, M. G.; Fokin, V. V.; Kolb, H. C.; Sharpless, K. B. *Angew. Chem. Int. Ed.* **2005**, *44*, 3275-3279.
- (53) Miller, Y.; Finlayson-Pitts, B. J.; Gerber, R. B., *J. Am. Chem. Soc.* **2009**, *131*, 12180-12185.
- (54) Diamant, R. M. E. *The Chemistry Of Building Materials*; Business Books: London, 1970.
- (55) Raff, J. D.; Njagic, B.; Chang, W. L.; Gordon, M. S.; Dabdub, D.; Gerber, R. B.; Finlayson-Pitts, B. J. *Proc. Natl. Acad. Sci.* **2009**, *106*, 13647-13654.
- (56) Njagic, B.; Raff, J. D.; Finlayson-Pitts, B. J.; Gordon, M. S.; Gerber, R. B., *J. Phys. Chem. A* **2010**, *114*, 4609-4618.
- (57) Molina M. J., Molina, L. T., Kolb C. E., *Annu. Rev. Phys. Chem* **1996**, *47*, 327-367
- (58) Kanakidou, M.; Seinfeld, J. H.; Pandis, S. N.; Barnes, I.; Dentener, F. J.; Facchini, M. C.; Van Dingenen, R.; Ervens, B.; Nenes, A.; Nielsen, C. J.; Swietlicki, E.; Putaud, J. P.; Balkanski, Y.; Fuzzi, S.; Horth, J.; et al., *Atmos. Chem. Phys* **2005**, *5*, 1053-1123
- (59) Griffin, R. J.; Cocker, D. R.; Seinfeld, J. H.; Dabdub, D. *Geophys., Res. Lett.* **1999**, *26*, 2721-2724.
- (60) Tsigaridis, K.; Kanakidou, M. *Atmos. Environ.* **2007**, *41*, 4682-4692.
- (61) Hallquist, M.; Wenger, J. C.; Baltensperger, U.; Rudich, Y.; Simpson, D.; Claeys, M.; Dommen, J.; Donahue, N. M.; George, C.; Goldstein, A. H.; Hamilton, J. F.; Herrmann, H.; Hoffmann, T.; Iinuma, Y.; Jang, M.; et al., *Atmos. Chem. Phys.* **2009**, *9*, 5155-5236.
- (62) Guenther, A.; Hewitt, C. N.; Erickson, D.; Fall, R.; Geron, C.; Graedel, T.; Harley, P.; Klinger, L.; Lerdau, M.; McKay, W. A.; Pierce, T.; Scholes, B.; Steinbrecher, R.; Tallamraju, R.; Taylor, J.; Zimmerman, P., *J. Geophys. Res.* **1995**, *100*, 8873-8892.
- (63) Pio, C. A.; Valente, A. A., *Atmos. Environ.* **1998**, *32*, 683-691.
- (64) Chhabra, P. S.; Ng, N. L.; Canagaratna, M. R.; Corrigan, A. L.; Russell, L. M.; Worsnop, D. R.; Flagan, R. C.; Seinfeld, J. H., *Atmos. Chem. Phys.* **2011**, *11*, 8827-8845.
- (65) Nizkorodov, S. A.; Laskin, J.; Laskin, A. *Phys. Chem. Chem. Phys.* **2011**, *13*, 3612-3629.
- (66) Christoffersen, T. S.; Hjorth, J.; Horie, O.; Jensen, N. R.; Kotzias, D.; Molander, L. L.; Neeb, P.; Ruppert, L.; Winterhalter, R.; Virkkula, A.; Wirtz, K.; Larsen, B. R. *Atmos. Environ.* **1998**, *32*, 1657-1661.
- (67) Yu, J.; Cocker, D. R. I.; Griffin, R. J.; Flagan, R. C.; Seinfeld, J. H., *J. Atmos. Chem.* **1999**, *34*, 207-258
- (68) Yu, J.; Griffin, R. J.; Cocker, D. R. I.; Flagan, R. C.; Seinfeld, J. H.; Blanchard, P., *Geophys. Res. Lett.* **1999**, *26*, 1145-1148.
- (69) Jang, M.; Kamens, R. M., *Atmos. Environ.* **1999**, *33*, 459-474.

- (70) Koch, S. Winterhalter, R. Uherek, E. Kolloff, A. Neeb, P. Moortgat, G. K., *Atmos. Environ.* **2000**, *34*, 4031-4042.
- (71) Glasius, M.; Lahaniati, M.; Calogirou, A.; Di Bella, D.; Jensen, N. R.; Hjorth, J.; Kotzias, D.; Larsen, B. R., *Environ. Sci. Technol.* **2000**, *34*, 1001-1010.
- (72) Kückelmann U.; Warscheid, B.; Hoffmann, T., *Anal. Chem.* **2000**, *72*, 1905-1912.
- (73) Capouet, M.; Peeters, J.; Noziere, B.; Mueller, J. F., *Atmos. Chem. Phys.* **2004**, *4*, 2285-2311.
- (74) Capouet, M.; Müller, J. F.; Ceulemans, K.; Compernelle, S.; Vereecken, L.; Peeters, J. J. *Geophys. Res. Atmos.* **2008**, *113*, D02308, doi:10.1029/2007JD008995.
- (75) Presto, A. A.; Huff Hartz, K. E.; Donahue, N. M., *Environ. Sci. Technol.* **2005**, *39*, 7036-7045.
- (76) Ma, Y.; Luciani, T.; Porter, R. A.; Russell, A. T.; Johnson, D.; Marston, G., *Phys. Chem. Chem. Phys.* **2007**, *9*, 5084-5087.
- (77) Ma, Y.; Willcox, T. R.; Russell, A. T.; Marston, G., *Chem. Commun.* **2007**, 1328-1330.
- (78) Laaksonen, A.; Kulmala, M.; O'Dowd, C. D.; Joutsensaari, J.; Vaattovaara, P.; Mikkonen, S.; Lehtinen, K. E. J.; Sogacheva, L.; Dal Maso, M.; Aalto, P.; Petäjä, T.; Sogachev, A.; Yoon, Y. J.; Lihavainen, H.; Nilsson, D.; et al. *Atmos. Chem. Phys.* **2008**, *8*, 2657-2665.
- (79) Walser, M. L.; Park, J.; Gomez, A. L.; Russell, A. R.; Nizkorodov, S. A., *J. Phys. Chem. A* **2007**, *111*, 1907-1913.
- (80) Walser, M. L.; Desyaterik, Y.; Laskin, J.; Laskin, A.; Nizkorodov, S. A., *Phys. Chem. Chem. Phys.* **2008**, *10*, 1009-1022.
- (81) Bateman, A. P.; Nizkorodov, S. A.; Laskin, J.; Laskin, A., *Phys. Chem. Chem. Phys.* **2009**, *11*, 7931-7942.
- (82) Shilling, J. E.; Chen, Q.; King, S. M.; Rosenoern, T.; Kroll, J. H.; Worsnop, D. R.; DeCarlo, P. F.; Aiken, A. C.; Sueper, D.; Jimenez, J. L.; Martin, S. T. *Atmos. Chem. Phys.* **2009**, *9*, 771-782.
- (83) Bateman, A. P.; Nizkorodov, S. A.; Laskin, J.; Laskin, A., *Anal. Chem.* **2010**, *82*, 8010-8016.
- (84) Eddingsaas, N. C.; Loza, C. L.; Yee, L. D.; Seinfeld, J. H.; Wennberg, P. O., *Atmos. Chem. Phys.* **2012**, *12*, 6489-6504.
- (85) Eddingsaas, N. C.; Loza, C. L.; Yee, L. D.; Chan, M.; Schilling, K. A.; Chhabra, P. S.; Seinfeld, J. H.; Wennberg, P. O., *Atmos. Chem. Phys.* **2012**, *12*, 7413-7427.
- (86) Guenther, A. B.; Jiang, X.; Heald, C. L.; Sakulyanontvittaya, T.; Duhl, T.; Emmons, L. K.; Wang, X. *Geosci. Model Dev.* **2012**, *5*, 1471-1492.
- (87) Yasmeen, F.; Vermeylen, R.; Maurin, N.; Perraudin, E.; Doussin, J.-F.; Claeys, M., *Environ. Chem.* **2012**, *9*, 236-246.
- (88) Jaoui, M.; Kamens, R. M., *J. Geophys. Res. Atmos.* **2001**, *106*, 12541-12558.
- (89) Yu, J.; Flagan, R. C.; Seinfeld, J. H., *Environ. Sci. Technol.* **1998**, *32*, 2357-2370.
- (90) Jaoui, M.; Kamens, R. M. *Atmos. Environ.* **2003**, *37*, 1835-1851.
- (91) Müller, L.; Reinig, M.-C.; Naumann, K. H.; Saathoff, H.; Mentel, T. F.; Donahue, N. M.; Hoffmann, T., *Atmos. Chem. Phys.* **2012**, *12*, 1483-1496.
- (92) Cheng, Y.; Li, S.-M.; Leithead, A.; Brickell, P. C.; Leitch, W. R., *Atmos. Environ.* **2004**, *38*, 5789-5800.
- (93) Cheng, Y.; Li, S.-M., *Environ. Sci. Technol.* **2005**, *39*, 2239-2246.
- (94) Raja, S.; Raghunathan, R.; Yu, X.-Y.; Lee, T.; Chen, J.; Kommalapati, R. R.; Murugesan, K.; Shen, X.; Qingzhong, Y.; Valsaraj, K. T.; Collett Jr, J. L., *Atmos. Environ.* **2008**, *42*, 2048-2061.
- (95) O'Dowd C. D.; Aalto P.; Hämeri K.; Kulmala M.; Hoffmann T., *Nature* **2002**, *416*, 497-498
- (96) Hyvärinen, A.-P.; Lihavainen, H.; Gaman, A.; Vairila, L.; Ojala, H.; Kulmala, M.; Viisanen, Y., *J. Chem. Eng. Data* **2005**, *51*, 255-260.
- (97) Li, X.; Hede, T.; Tu, Y.; Leck, C.; Ågren, H., *J. Phys. Chem. Lett.* **2010**, *1*, 769-773.
- (98) Ervens B., Turpin, B. J.; Weber, R. J. , *Atmos. Chem. Phys.* **2011**, *11*, 11069-11102
- (99) McNeill, V. F.; Grannas, A. M.; Abbatt, J. P. D.; Ammann, M.; Ariya, P.; Bartels-Rausch, T.; Domine, F.; Donaldson, D. J.; Guzman, M. I.; Heger, D.; Kahan, T. F.; Kl' an, P.; Masclin, S.; Toubin, C.; Voisin, D., *Atmos. Chem. Phys.* **2012**, *12*, 9653-9678.
- (100) Faust B.C.; Anastasio C.; Allen J. M.; Arakaki T., *Science* **1993**, *260*, 73-75.
- (101) Vaida, V.; Kjaergaard, H. G.; Feierabend, K. J., *Int. Rev. Phys. Chem.* **2011**, *22*, 203-219.

- (102) Kolb, C. E.; Cox, R. A.; Abbatt, J. P. D.; Ammann, M.; Davis, E. J.; Donaldson, D. J.; Garrett, B. C.; George, C.; Griffiths, P. T.; Hanson, D. R.; Kulmala, M.; McFiggans, G.; Pöschl, U.; Riipinen, I.; Rossi, M. J.; Rudich, Y.; Wagner, P. E.; Winkler, P. M.; Worsnop, D. R.; O' Dowd, C. D., *Atmos. Chem. Phys.* **2010**, *10*, 10561-10605.
- (103) Meng Z. Y., Seinfeld, J. H.; Saxena, P.; Kim, Y. P., *Aerosol Sci. Technol.*, **1995**, *22*, 111-123
- (104) Wang J.; Jacob, D. J.; Martin, S. T., *J. Geophys. Res.* **2008**, *113*, D11207, doi:10.1029/2007JD009368
- (105) Blando J. D., Turpin B. J., *Atmos. Environ.* **2000**, *34*, 1623-1632
- (106) Jang, M.; Czoschke, N. M.; Lee, S.; Kamens, R. M., *Science* **2002**, *298*, 814-817.
- (107) Lee, A. K. Y.; Herckes, P.; Leaitch, W. R.; Macdonald, A. M.; Abbatt, J. P. D., *Geophys. Res. Lett.* **2011**, *38*, L11805, doi:10.1029/2011GL047439.
- (108) Lee, A. K. Y.; Zhao, R.; Gao, S. S.; Abbatt, J. P. D., *J. Phys. Chem. A* **2011**, *115*, 10517-10526.
- (109) Liu, Y.; Siekmann, F.; Renard, P.; El Zein, A.; Salque, G.; El Haddad, I.; Temime-Roussel, B.; Voisin, D.; Thissen, R.; Monod, A., *Atmos. Environ.* **2012**, *49*, 123-129
- (110) Ervens, B.; Wang, Y.; Eagar, J.; Leaitch, W. R.; Macdonald, A. M.; Valsaraj, K. T.; Herckes, P., *Atmos. Chem. Phys.* **2013**, *13*, 5117-5135.
- (111) Nguyen, T. B.; Coggon, M. M.; Flagan, R. C.; Seinfeld, J. H. *Environ. Sci. Technol.* **2013**, *47*, 4307-4316.
- (112) Chen, J. Griffin, R. J. Grini, A. Tulet, P., *Atmos. Chem. Phys.* **2007**, *7*, 5343-5355.
- (113) Carlton, A. G.; Turpin, B. J.; Lim, H.-J.; Altieri, K. E.; Seitzinger, S., *Geophys. Res. Lett.* **2006**, *33*, L06822, DOI: 10.1029/2005GL025374.
- (114) Carlton, A. G.; Turpin, B. J.; Altieri, K. E.; Seitzinger, S. P.; Mathur, R.; Roselle, S. J.; Weber, R. J., *Environ. Sci. Technol.* **2008**, *42*, 8798-8802.
- (115) Fu, T.-M.; Jacob, D. J.; Wittrock, F.; Burrows, J. P.; Vrekoussis, M.; Henze, D. K., *J. Geophys. Res. Atmos.* **2008**, *113*, D15303, doi:10.1029/2007JDO09505
- (116) Dzepina, K.; Volkamer, R. M.; Madronich, S.; Tulet, P.; Ulbrich, I. M.; Zhang, Q.; Cappa, C. D.; Ziemann, P. J.; Jimenez, J. L., *Atmos. Chem. Phys.* **2009**, *9*, 5681-5709.
- (117) Ervens, B.; Volkamer, R. *Atmos. Chem. Phys.* **2010**, *10*, 8219-8244.
- (118) Bateman, A. P.; Nizkorodov, S. A.; Laskin, J.; Laskin, A., *Phys. Chem. Chem. Phys.* **2011**, *13*, 12199-12212.
- (119) Epstein, S. A.; Nizkorodov, S. A., *Atmos. Chem. Phys.* **2012**, *12*, 8205-8222.
- (120) Nguyen, T. B.; Laskin, A.; Laskin, J.; Nizkorodov, S. A., *Phys. Chem. Chem. Phys.* **2012**, *14*, 9702-9714.
- (121) Epstein, S. A.; Tapavicza, E.; Furche, F.; Nizkorodov, S. A., *Atmos. Chem. Phys.* **2013**, *13*, 9461-9477.
- (122) Renbaum-Wolff, L.; Grayson, J. W.; Bateman, A. P.; Kuwata, M.; Sellier, M.; Murray, B. J.; Shilling, J. E.; Martin, S. T.; Bertram, A. K., *Proc. Natl. Acad. Sci.* **2013**, *110*, 8014-8019.
- (123) Ravishankara, A. R.; Longfellow, C. A., *Phys. Chem. Chem. Phys.* **1999**, *1*, 5433-5441.
- (124) Chang, W. L.; Bhave, P. V.; Brown, S. S.; Riemer, N.; Stutz, J.; Dabdub, D., *Aerosol Sci. Technol.* **2011**, *45*, 665-695.
- (125) Osthoff, H. D.; Roberts, J. M.; Ravishankara, A. R.; Williams, E. J.; Lerner, B. M.; Sommariva, R.; Bates, T. S.; Coffman, D.; Quinn, P. K.; Dibb, J. E.; Stark, H.; Burkholder, J. B.; Talukdar, R. K.; Meagher, J.; Fehsenfeld, F. C.; Brown, S. S. *Nature Geosci* **2008**, *1*, 324-328.
- (126) Virtanen, A.; Joutsensaari, J.; Koop, T.; Kannosto, J.; Yli-Pirilä, P.; Leskinen, J.; Mäkelä, J. M.; Holopainen, J. K.; Pöschl, U.; Kulmala, M.; Worsnop, D. R.; Laaksonen, A., *Nature* **2010**, *467*, 824-827.
- (127) Bones, D. L.; Reid, J. P.; Lienhard, D. M.; Krieger, U. K., *Proc. Natl. Acad. Sci.* **2012**, *109*, 11613-11618.
- (128) Abramson, E.; Imre, D.; Beranek, J.; Wilson, J.; Zelenyuk, A., *Phys. Chem. Chem. Phys.* **2013**, *15*, 2983-2991.
- (129) Perraud, V.; Bruns, E. A.; Ezell, M. J.; Johnson, S. N.; Yu, Y.; Alexander, M. L.; Zelenyuk, A.; Imre, D.; Chang, W. L.; Dabdub, D.; Pankow, J. F.; Finlayson-Pitts, B. J., *Proc. Natl. Acad. Sci.* **2012**, doi:10.1073/pnas.1119909109
- (130) Riipinen, I.; Pierce, J. R.; Yli-Juuti, T.; Nieminen, T.; Häkkinen, S.; Ehn, M.; Junninen, H.; Lehtipalo, K.; Petäjä, T.; Slowik, J.; Chang, R.; Shantz, N. C.; Abbatt, J.; Leaitch, W. R.; Kerminen, V. M.; Worsnop, D. R.; Pandis, S. N.; Donahue, N. M.; Kulmala, M., *Atmos.*

- Chem. Phys.* **2011**, *11*, 3865-3878.
- (131) Koop, T.; Bookhold, J.; Shiraiwa, M.; Pöschl, U., *Phys. Chem. Chem. Phys.* **2011**, *13*, 19238-19255.
- (132) Shiraiwa, M.; Ammann, M.; Koop, T.; Pöschl, U., *Proc. Natl. Acad. Sci.* **2011**, *108*, 11003-11008.
- (133) Hosny, N. A.; Fitzgerald, C.; Tong, C.; Kalberer, M.; Kuimova, M. K.; Pope, F. D., *Faraday Discuss.* **2013**, doi: 10.1039/C3FD00041A
- (134) Shiraiwa, M.; Seinfeld, J. H. *Geophys. Res. Lett.* **2012**, *39*, L24801, doi:10.1029/2012GL054008.
- (135) Harris, M. O.; Corcoran, J. J. Toxicological profile for dinitrophenols; Services, U. S. Department of Human and Health Services, 1995.
- (136) Shea, P. J.; Weber, J. B.; Overcash, M. R. Biological activities of 2,4-dinitrophenol in plant- soil systems. In *Residue Reviews*; Gunther, F., Gunther, J., Eds.; Springer New York, 1983; Vol. 87; pp 1-41.
- (137) Albinet, A.; Minero, C.; Vione, D., *Chemosphere* **2010**, *80*, 753-758.
- (138) Yang, G.-P.; Qi, J.-L., *Chemical Journal of Chinese Universities* **2002**, *23*, 1180-1182.
- (139) Lipczynska-Kochany, E. *Water Poll. Res. J. Canada* **1992**, *27*, 97-122.
- (140) Alif, A.; Pilichowski, J.-F.; Boule, P., *J. Photochem. Photobiol. A: Chemistry* **1991**, *59*, 209-219.
- (141) Bejan, I.; Abd El Aal, Y.; Barnes, I.; Benter, T.; Bohn, B.; Wiesen, P.; Kleffmann, J., *Phys. Chem. Chem. Phys.* **2006**, *8*, 2028-2035.
- (142) Lüttke, J.; Scheer, V.; Levsen, K.; Wunsch, G.; Neil Cape, J.; Hargreaves, K. J.; Storeton-West, R. L.; Acker, K.; Wieprecht, W.; Jones, B., *Atmos. Environ.* **1997**, *31*, 2637-2648.
- (143) Vione, D.; Maurino, V.; Minero, C.; Pelizzetti, E. *Environ. Sci. Technol.* **2005**, *39*, 7921-7931.
- (144) ASTER (Assessment Tools for the Evaluation of Risk); Environmental Protection Agency.
- (145) Sanagi, M. M.; Miskam, M.; Wan Ibrahim, W. A.; Hermawan, D.; Aboul-Enein, H. Y., *J. Sep. Sci.* **2010**, *33*, 2131-2139.
- (146) McDow, S. R.; Jang, M.; Hong, Y.; Kamens, R. M., *J. Geophys. Res. Atmos.* **1996**, *101*, 19593-19600.
- (147) Bunce, N. J.; Lamarre, J.; Vaish, S. P., *Photochem. Photobiol.* **1984**, *39*, 531-533.
- (148) U. S. Environmental Protection Agency, EPA Henrywin v3.20, 2011.
- (149) Hobbs, P. V. *Aerosol-Cloud-Climate Interactions*; Academic Press, 1993.
- (150) Monod, A.; Doussin, J. F., *Atmos. Environ.* **2008**, *42*, 7611-7622.
- (151) Doussin, J. F.; Monod, A., *Atmos. Chem. Phys.* **2013**, *13*, 11625-11641.
- (152) Kwok, E. S. C.; Atkinson, R., *Atmos. Environ.* **1995**, *29*, 1685-1695.
- (153) NCAR Tropospheric ultraviolet & visible radiation model, National Center for Atmospheric Research, Atmospheric Chemistry Division, 2012; Vol. Edition 4.4.
- (154) Rohrer, F.; Berresheim, H., *Nature* **2006**, *442*, 184-187.
- (155) Donahue, N. M.; Robinson, A. L.; Stanier, C. O.; Pandis, S. N., *Environ. Sci. Technol.* **2006**, *40*, 2635-2643.
- (156) Pankow, J. F., *Atmos. Environ.* **1994**, *28*, 189-193.
- (157) Bilde, M.; Pandis, S. N. *Environ. Sci. Technol.* **2001**, *35*, 3344-3349.
- (158) Matsunaga, S.; Mochida, M.; Kawamura, K. *Atmos. Environ.* **2003**, *37*, 2045-2050.
- (159) Updyke, K. M.; Nguyen, T. B.; Nizkorodov, S. A. *Atmos. Environ.* **2012**, *63*, 22-31.
- (160) Sioutas, C. Sioutas cascade impactor; University of Southern California: USA, 2004; Vol. US 6786105 B1.
- (161) Kamboures, M. A.; Nizkorodov, S. A.; Gerber, R. B. *Proc. Natl. Acad. Sci.* **2010**, *107*, 6600-6604.
- (162) Epstein, S. A.; Shemesh, D.; Tran, V. T.; Nizkorodov, S. A.; Gerber, R. B., *J. Phys. Chem. A* **2012**, *116*, 6068-6077.
- (163) Hopkinson, L.; Roberts, S.; Herrington, R.; Wilkinson, J., *Contrib. Mineral Petrol* **1999**, *137*, 342-350.
- (164) Helgaker, T., *Chem. Phys. Lett.*, **1991**, *182*, 503-510.
- (165) Ahlrichs, R.; Bar, M.; Haser, M.; Horn, H.; Kolmel, C., *Chem. Phys. Lett.* **1989**, *162*, 165-169.
- (166) Frisch, M. J.; Trucks, G. W.; Schlegel, H. B.; Scuseria, G. E.; Robb, M. A.; Cheeseman, J. R.; Montgomery, J. J. A.; Vreven, T.; Kudin, K. N.; Burant, J. C.; Millam, J. M.; Iyengar, S. S.; Tomasi, J.; Barone, V.; Mennucci, B.; Cossi, M., et al. Gaussian 03, Revision C.02, **2004**.

- (167) Dunning, T. H., *J. Chem. Phys.* **1989**, *90*, 1007-1023.
- (168) Weigend, F.; Haser, M., *Theor. Chem. Acc.* **1997**, *97*, 331-340.
- (169) Schirmer, J., *Phys. Rev. A* **1982**, *26*, 2395-2416.
- (170) Weber, W.; Thiel, W., *Theor. Chem. Acc.* **2000**, *103*, 495-506.
- (171) Koslowski, A.; Beck, M. E.; Thiel, W. J., *Comput. Chem.* **2003**, *24*, 714-726.
- (172) Thiel, W. *MNDO program, version 6.1, Mülheim an der Ruhr, Germany* **2007**.
- (173) Fabiano, E.; Keal, T. W.; Thiel, W., *Chem. Phys.* **2008**, *349*, 334-347.
- (174) Shemesh, D.; Lan, Z. G.; Gerber, R. B., *J. Phys. Chem. A* **2013**, *117*, 11711-11724.
- (175) Mason, M. G.; Von Holle, W. G.; Robinson, D. W., *J. Chem. Phys.* **1971**, *54*, 3491-3499.
- (176) Bondybey, V. E.; Pimentel, G. C., *J. Chem. Phys.* **1972**, *56*, 3832-3836.
- (177) Khriachtchev, L.; Lignell, A.; Juselius, J.; Räsänen, M.; Savchenko, E., *J. Chem. Phys.* **2005**, *122*, 014510-7.
- (178) Arrhenius, S. Z., *Phys. Chem.* **1889**, *4*, 226-228.
- (179) Goldanskii, V. I.; Frank-Kamenetskii, M. D.; Barkalov, I. M. *Science* **1973**, *182*, 1344-1345.
- (180) Khriachtchev, L., *J. Mol. Struct.* **2008**, *880*, 14-22.
- (181) Pettersson, M.; Khriachtchev, L.; Lignell, A.; Räsänen, M.; Bihary, Z.; Gerber, R. B., *J. Chem. Phys.* **2002**, *116*, 2508-2515.
- (182) Khriachtchev, L.; Pettersson, M.; Pehkonen, S.; Isoniemi, E.; Räsänen, M., *J. Chem. Phys.* **1999**, *111*, 1650-1657.
- (183) Khriachtchev, L.; Saarelainen, M.; Pettersson, M.; Räsänen, M., *J. Chem. Phys.* **2003**, *118*, 6403-6410.
- (184) Wesolowski, S. S.; Fermann, J. T.; Crawford, T. D.; Schaefer III, H. F., *J. Chem. Phys.*, **1997**, *106*, 7178-7184.
- (185) Wolf, I.; Shapira, A.; Giniger, R.; Miller, Y.; Gerber, R. B.; Cheshnovsky, O. *Angew. Chem. Int. Ed.* **2008**, *47*, 6272-6274.
- (186) Bartels-Rausch, T.; Brigante, M.; Elshorbany, Y. F.; Ammann, M.; D'Anna, B.; George, C.; Stemmler, K.; Ndour, M.; Kleffmann, J., *Atmos. Environ.* **2010**, *44*, 5443-5450.
- (187) Kleffmann, J., *ChemPhysChem* **2007**, *8*, 1137-1144.
- (188) Zhou, X.; Beine, H. J.; Honrath, R. E.; Fuentes, J. D.; Simpson, W.; Shepson, P. B.; Bottenheim, J. W., *Geophys. Res. Lett.* **2001**, *28*, 4087-4090.
- (189) Rohrer, F.; Bohn, B.; Brauers, T.; Brüning, D.; Johnen, F. J.; Wahner, A.; Kleffmann, J., *Atmos. Chem. Phys.* **2005**, *5*, 2189-2201.
- (190) Zhou, X.; He, Y.; Huang, G.; Thornberry, T. D.; Carroll, M. A.; Bertman, S. B., *Geophys. Res. Lett.* **2002**, *29*, 26-1-26-4.
- (191) Calvert, J. G.; Pitts, J. N. *Photochemistry*; John Wiley: New York, 1966.
- (192) Bamford, C. H.; Norrish, R. G. W., *J. Chem. Soc.* **1935**, 1504-1511.
- (193) Srinivasan, R. *Photochemistry of the Cyclic Ketones*. In *Advances in Photochemistry*; John Wiley & Sons, Inc., 2007; pp 83-113.
- (194) Norman, I.; Pitts, J. N., Jr., *J. Am. Chem. Soc.* **1955**, *77*, 6104-6107.
- (195) Shaffer, G. W.; Doerr, A. B.; Purzycki, K. L., *J. Org. Chem.* **1972**, *37*, 25-29.
- (196) Baldwin, P. J.; Canosa-Mas, C. E.; Frey, H. M.; Walsh, R., *J. Chem. Soc., Faraday Trans. 2: Molecular and Chemical Physics* **1987**, *83*, 1049-1058.
- (197) Baldwin, P. J.; Canosa-Mas, C. E.; Frey, H. M.; Walsh, R., *Int. J. Chem. Kin.* **1987**, *19*, 997-1013.
- (198) von Sonntag, C.; Schuchmann, H.-P., *Angew. Chem. Int. Ed.* **1991**, *30*, 1229-1253.
- (199) Nozière, B.; Barnes, I.; Becker, K.-H., *J. Geophys. Res.* **1999**, *104*, 23645-23656.
- (200) Praplan, A. P.; Barmet, P.; Dommen, J.; Baltensperger, U., *Atmos. Chem. Phys.* **2012**, *12*, 10749-10758
- (201) Griffith, E. C.; Carpenter, B. K.; Shoemaker, R. K.; Vaida, V., *Proc. Natl. Acad. Sci.* **2013**, *110*, 11714-11719.
- (202) Yamaji, T.; Saito, T.; Hayamizu, K.; Yanagisawa, M.; Yamamoto, O.; Wasada, N.; Someno, K.; Kinugasa, S.; Tanabe, K.; Tamura, T.; Hiraishi, J. *Spectral Database for Organic Compounds SDBS*; National Institute of Advanced Industrial Science and Technology (AIST), 2013.
- (203) *Advanced Chemistry Development*, I. A. L.; 11.01 ed., 1994-2013.
- (204) Xu, H.; Wentworth, P. J.; Howell, N. W.; Joens, J. A. *Spectrochim. Acta Part A: Molecular Spectroscopy* **1993**, *49*, 1171-1178.
- (205) Mariella, R. P.; Raube, R. R., *J. Am. Chem. Soc.* **1952**, *74*, 518-521.
- (206) Pavia, D. L.; Lampman, G. M.; Kriz, G. S.; Vyvyan, J. R. *Introduction to spectroscopy*;

- Brooks/Cole Cengage learning, 2009.
- (207) Henry, K. M.; Donahue, N. M., *J. Phys. Chem. A* **2012**, *116*, 5932-5940.
 - (208) Donahue, N. M.; Chuang, W.; Epstein, S. A.; Kroll, J. H.; Worsnop, D. R.; Robinson, A. L.; Adams, P. J.; Pandis, S. N., *Environ. Chem.* **2013**, *10*, 151-157.
 - (209) Reinhardt, A.; Emmenegger, C.; Gerrits, B.; Panse, C.; Dommen, J.; Baltensperger, U.; Zenobi, R.; Kalberer, M., *Anal. Chem.* **2007**, *79*, 4074-4082.
 - (210) Murto, J., *Acta Chem. Scand.* **1964**, *18*, 1029-1042.
 - (211) França Faria, M. A.; de Sá, C. F.; Lima, G. R.; Filho, J. I. B. C.; Martins, R. J.; de M. Cardoso, M.; Barcia, O. E. *J. Chem. Eng. Data* **2005**, *50*, 1938-1943.
 - (212) Murphy, D. M.; Froyd, K. D.; Schwarz, J. P.; Wilson, J. C., *Q. J. Roy. Meteor. Soc.* **2013**, Accepted.
 - (213) Murray, B. J. *Atmos. Chem. Phys.* **2008**, *8*, 5423-5433.
 - (214) Mikhailov, E.; Vlasenko, S.; Martin, S. T.; Koop, T.; Pöschl, U. *Atmos. Chem. Phys.* **2009**, *9*, 9491-9522.
 - (215) Odian, G. *Principles of polymerization*, 4 ed.; John Wiley&Sons, 2004.
 - (216) Pfrang, C.; Shiraiwa, M.; Pöschl, U. *Atmos. Chem. Phys.* **2011**, *11*, 7343-7354.